ABSTRACT

Title of dissertation: LEAD ZIRCONATE TITANATE THIN FILMS FOR PIEZOELECTRIC ACTUATION AND SENSING OF MEMS RESONATORS

Brett Harold Piekarski, Doctor of Philosophy, 2005

Dissertation directed by: Professor Donald DeVoe
Department of Mechanical Engineering and Bioengineering Graduate Program

This research is focused on examining the potential benefits and limitations of applying sol-gel lead zirconate titanate (PZT) piezoelectric thin films to on-chip piezoelectrically driven RF microelectromechanical system (MEMS) resonators in the low frequency (LF) to very high frequency (VHF) frequency range. MEMS fabrication methods are presented for fabricating PZT-based MEMS resonator structures along with investigations into the resultant thin film residual stresses and material properties, and their impact on resonator frequency, beam curvature, and resonant mode shape. The PZT, silicon dioxide (SiO2), platinum (Pt), and silicon nitride (Si3N4) thin film material properties are characterized and validated by wafer bow, cantilever resonance, cantilever thermal-induced tip deflection and finite element modeling (FEM) techniques.

The performance of the fabricated PZT-based MEMS resonators are presented and compared to previously demonstrated zinc oxide (ZnO) based resonators as well as to

electrostatically based MEMS resonator designs. Resonators with frequency response peaks of greater than 25 dB, quality factors up to 4700, and resonant frequencies up to 10 MHz are demonstrated along with a discussion of their advantages and disadvantages for use as MEMS resonators.

Nonlinear resonator response is also investigated in relation to the onset of classic Duffing behavior, beam buckling and mode coupling. Fabrication techniques, operating conditions, and design rules are presented to minimize or eliminate nonlinear resonator response.

LEAD ZIRCONATE TITANATE THIN FILMS FOR PIEZOELECTRIC ACTUATION AND SENSING OF MEMS RESONATORS

By

Brett Harold Piekarski

Dissertation submitted to the Faculty of the Graduate School of the
University of Maryland, College Park in partial fulfillment
of the requirements for the degree of
Doctor of Philosophy
2005

Advisory Committee:
Professor Donald DeVoe, Chair
Professor Balakumar Balachandran
Professor Amr Baz
Professor Reza Ghoddsi, Dean's Representative
Professor Ichiro Takeuchi

© Copyright by
Brett Piekarski
2005

ACKNOWLEDGEMENTS

First I would like to thank Professor Donald DeVoe for the opportunity to pursue my graduate studies under his guidance at the University of Maryland and for his extreme patience as I have pursued this goal in parallel with my sometimes more-than-full-time job at the U.S. Army Research Laboratory. I would also like to thank my committee members, Professor Balakumar Balachandran, Professor Amr Baz, and Professor Reza Ghoddsi for their input, guidance, classroom instruction, and support, all of which have been truly exceptional, over the duration of this research. Also sincere thanks to Professor Ichiro Takeuchi for his interest in the research and for offering to step in at the last minute on the committee with the departure of Dr. Ramamoorthy Ramesh (currently on leave to the University of California, Berkeley).

I would also like to thank many of my coworkers and management at ARL for their support and technical exchanges. This includes Tom Bower for giving me the freedom and time to pursue my degree while working under his supervision, Dr. Robert Zeto (now retired) for giving me the opportunity to work in MEMS and encouraging me to begin my doctoral work in PZT MEMS resonators, and Ronald Polcawich and Dr. Madan Dubey for their many hours of discussing PZT materials, processing and devices. Thanks also to Jeff Pulskamp and Luke Currano for the many hours of discussing MEMS mechanical systems and modeling, Matthew Ervin for his support in obtaining SEM images, and Eugene Zakar, John Conrad and Ritchie Piekarz for their help and expertise in MEMS processing. And finally, thanks to my team members at ARL, who have carried the ball and given me the time to finish this research; Michael Chapman, Gregory Chevis, Nelson Mark, Joel Martin, Dr. Madumita Roy, Joyce Bell-Sampson, and Thomas Takacs.

Most importantly, I could not have completed my graduate work without the understanding and support of my friends and family, especially my loving wife Juliet and our dog Timber, who have given me space when needed and hugs and kisses when needed as well.

Table of Contents

List of Tables .... **vi**

List of Figures .... **viii**

1. Introduction **1**

1.1 Motivation for Research 1
1.2 Additional Research 10

2. Background **11**

2.1 Piezoelectricity 11
2.2 Sol-Gel PZT 13
2.3 Piezoelectric Actuation and Sensing 16
2.4 Piezoeletric Resonator Concept 23

3. Fabrication Process Development **28**

3.1 Overall Process Flow 28
3.2 Top Electrode 29
3.3 Bottom Electrode 30
3.4 Resonator Formation 31
3.5 Resonator Release 34
3.6 Final Overall Process 37

4. Experimental Apparatus **38**

4.1 Wafer Bow Stress Gauge 38
4.2 Network Analyzer and Vacuum Probe Station 40
4.3 Electrode Area and Impedance Matching 42
4.4 Laser Doppler Vibrometer 47
4.5 Optical Profilometer 49
4.6 Optical Microscope 50

5. Material Characterization **52**

5.1 Approach 52
5.2 SiO_2 Material Properties 56
5.3 Pt Material Properties 57
5.4 Si_3N_4 Material Properties 58
5.5 PZT Young's Modulus 61
5.6 PZT Stack Residual Stress and Stress Gradient 65
5.7 PZT CTE Measurement 71

6. FEM Model and Material Property Validation **75**

6.1 Clamped-Clamped Beam Theory 75

6.2 Basic Finite Element Model ... 77
6.3 Clamped-Clamped Resonator Comparisons to 3-D FEM ... 82
6.4 Free-Free Resonator Comparison to 3-D FEM ... 89
6.5 Resonator Thermal Stability Comparison to 3-D FEM ... 92

7. Uncompensated Resonators ... 95

7.1 Generation I Resonator Design and Fabrication ... 95
7.2 Generation I Resonator Performance ... 96
7.3 Generation I Resonator Mode Shape Analysis ... 99

8. Stress Modified Resonators ... 111

8.1 Generation II Resonator Design and Fabrication ... 111
8.2 Generation II Resonator Performance ... 113
8.3 Generation II Resonator Poling ... 118
8.4 Generation II Resonator Thermal Stability ... 121
8.5 Generation II Resonator Linear Response Analysis ... 123
8.6 Generation II Resonator Nonlinear Response Analysis ... 129
8.7 Generation II Resonator Mode Shape Analysis ... 137
8.8 Additional Analysis of Generation II Clamped-Clamped Resonator Nonlinear Response ... 152

9. Stress Compensated Resonators ... 156

9.1 Generation III Resonator Design and Fabrication ... 156
9.2 Generation III Resonator Performance ... 162
9.3 Generation III Resonator Mode Shape Analysis ... 164
9.4 Generation III Resonator Thermal Stability ... 166

10. Conclusions and Future Work ... 168

10.1 Conclusions ... 168
10.2 Future Work ... 171

Bibliography ... 172

List of Tables

1.1 Electrostatic MEMS resonator references. 5

1.2 Reported piezoelectric properties for ZnO, AlN, and PZT. 8

4.1 Olympus microscope calibration. 51

5.1 dσ/dT slopes for oxide on silicon and quartz substrates. 57

5.2 dσ/dT slopes for platinum on silicon and quartz substrates. 58

5.3 Matrix of thin film thickness (microns). 62

5.4 Measured and modeled cantilever resonant frequencies by wafer (Hz). 64

5.5 Thin film residual stresses. 66

5.6 Measured and modeled stress-induced cantilever deflections. 68

5.7 Mapping of false CTE to film thickness. 69

5.8 Comparison of modeled to measured residual stresses. 71

5.9 Comparison of measured to modeled thermal-induced tip deflection. 74

6.1 Resonator undercut amount by wafer. 83

6.2 Resonant frequencies for resonators from wafers with prior material property and stress analysis. 87

6.3 Resonant frequencies for resonators from wafers without prior material property and stress analysis. 87

6.4 Modeled and measured values frequencies for a 400 μm resonator. 89

6.5 Comparison of free-free measured and modeled frequencies. 91

6.6 Stress gradient in x-direction, beam deflection, and frequency as a function of temperature. 94

7.1 Initial film thickness generation I resonators. 95

7.2 Comparison of modeled and measured mode frequencies. 102

7.3 Measured and predicted resonant frequencies for buckled generation I resonator. 109

8.1 Initial film thickness for generation II resonators. 111

8.2 Typical residual stress in each individual layer. 112

8.3 Typical cumulative residual stress in PZT stack. 112

8.4 Modeled PZT stress vs. PZT poling condition. 120

8.5 Film thickness for clamped-clamped beam resonators. 138

8.6 Critical euler buckling force and stress. 142

8.7 Measured static deflection at center of resonator. 149

8.8 Comparison of measured dual drive actuation to modeled modal analysis for a 400 μm resonator. 154

9.1 Material thickness for generation III resonators. 157

9.2 Measured stress in generation III resonators. 158

9.3 Effect of nitride layer position on beam deflection and resonant frequency. 162

10.1 Summary of measured and modeled material properties. 170

List of Figures

1.1 The Radio Frequency spectrum. 1

1.2 A typical transmitter schematic showing potential locations for MEMS resonator insertion.... 4

1.3 Concept for a piezoelectric resonator. 8

2.1 Unpoled and poled ferroelectric domain state orientations. 12

2.2 Typical hysteresis curve for a piezoelectric ceramic. 13

2.3 Perovskite crystal structure. 14

2.4 Unit cell distortion of PZT versus mole % $PbTiO_3$ at room temperature. 14

2.5 Sol-gel PZT deposition process flow diagram. 16

2.6 Visualization of the direct and converse piezoelectric effect. 17

2.7 Actuation and sensing mechanism using piezoelectric thin films. 18

2.8 Force-strain relationship for a piezoelectric element. 19

2.9 Top view and cross-section of a piezoelectric MEMS resonator. 23

2.10 Equation (2.30) plotted over a factor of 10 for the value of Q and d_{31}. 27

3.1 Piezoelectric resonator fabrication process flow. 28

3.2 Pt redeposition and fencing after photoresist removal. 31

3.3 Pt flake shorting the PZT structure. 32

3.4 PZT stack cross section after ion milling at a constant 40° angle. 32

3.5 PZT stack cross section after ion milling at a constant 5º with a hard baked photoresist mask. 33

3.6 PZT stack after ion milling with both 40º and 85º ion milling angles. 33

3.7 Backside of a triple-beam resonator viewed through the DRIE opening on the backside of the wafer. 35

3.8 Topside image of fabricated single and triple-beam PZT resonators released from the backside. 35

3.9 Topside image of fabricated single-beam PZT resonator released from the topside. 37

4.1 Tencor FLX-2908 system used for wafer bow and stress measurements................. 38

4.2 FLX-2908 internal configuration showing wafer placement and heating elements.. 38

4.3 Electrical and vacuum test set-up used for all electrical response measurements..... 40

4.4 Schematic of electrical test set-up.. 41

4.5 Magnitude and phase response for an 80 µm PZT resonator with full 100 x 200 µm electrodes. 42

4.6 Magnitude and phase response for an 80 µm PZT Resonator with reduced electrode area. 43

4.7 Magnitude and phase response for a 400 µm PZT resonator with 100 x 200 µm top electrodes. 44

4.8 Magnitude and phase response of a 400 µm PZT resonator with 100 x 50 µm top electrodes. 44

4.9 Magnitude and phase response with use of a unity gain op-amp. 45

4.10 Magnitude and phase response of a 400 µm PZT resonator with 100 x 50 µm top electrodes and 1 MΩ input impedance. 46

4.11 Polytech LDV test set-up used for measuring resonator frequency and mode shapes. 47

4.12 Schematic of LDV measurement technique. 48

4.13 Veeco optical profilometer used for static displacement measurements. 49

5.1 Plot of dσ/dT curves for SiO_2 on silicon and quartz. 56

5.2 Plot of dσ/dT curves for Pt on silicon and quartz. 57

5.3 Plot of dσ/dT curves for Si_3N_4 on silicon and quartz. 59

5.4 ANSYS output for cantilever resonance modeling.. 64

5.5 Example of stress-induced cantilever static deflection. 66

5.6 ANSYS output for residual stress deformation of a cantilever................................ 68

5.7 Modeled stress gradient at electrode transition... 70

5.8 ANSYS result for a 200 µm thermally deflected beam at 100 °C. 73

6.1 2-D FEM elements for clamped-clamped beam. 78

6.2 ANSYS boundary conditions. 82

6.3 SEM of anchor undercut area. 83

6.4 Comparison of ANSYS 8.0 model to measured first natural frequency.................... 84

6.5 Plot of errors associated with variations in beam length, anchor undercut, material properties, and residual stress. 85

6.6 Plot of modeled frequency data with associated error and measured first natural frequencies. 86

6.7 Modeled and measured first resonant mode for a 400 μm resonator......................... 88

6.8 Modeled and measured second resonant mode for a 400 μm resonator.................... 88

6.9 Modeled and measured third resonant mode for a 400 μm resonator. 89

6.10 Schematic of a single-side drive free-free resonator design. 90

6.11 Modeled and measured “teeter-totter” first resonant mode for a free-free beam resonator. 90

6.12 Modeled and measured “trampoline” second resonant mode for a free-free beam resonator. 91

6.13 Modeled and measured “bending” third resonant mode for a free-free beam resonator. 91

6.14 LDV velocity spectrum for a 200 μm free-free resonator 92

6.15 ANSYS model for resonator thermal stability modeling... 92

6.16 Comparison of ANSYS thermal model to measured resonant frequencies............. 93

7.1 SEM images of fabricated generation I resonators showing beam buckling............. 96

7.2 SEM image of a ZnO clamped-clamped beam resonator. 96

7.3 Typical performance of a ZnO clamped-clamped beam resonator........................... 97

7.4 Full frequency response of 400 μm generation I resonator. 98

7.5 First resonant peak for generation I PZT clamped-clamped resonator...................... 99

7.6 Second resonant peak for generation I PZT clamped-clamped resonator. 99

7.7 LDV velocity spectrum for a 400 μm generation I resonator. 100

7.8 Predicted and measured first mode for a generation I resonator. 101

7.9 Predicted and measured second mode for a generation I resonator. 101

7.10 Predicted and measured third mode for a generation I resonator. 101

7.11 Predicted and measured fourth mode for a generation I resonator. 102

7.12 3-D view of measured buckled mode shape for 400 μm generation I resonator. 104

7.13 Cross section of measured optical profilometer data showing buckled mode shape. 105

7.14 MATLAB modeled 1st buckled mode shape. 106

7.15 Nondimensional solution for resonant frequency versus buckling level for a buckled clamped-clamped beam. 108

7.16 Measured buckled-down mode shape for 400 μm generation I resonator from same wafer as device measured and reported in Figures 7.12 and 7.13. 110

8.1 400 μm released clamped-clamped resonator from wafer W4. 113

8.2 Magnitude and phase response for a 400 μm resonator from W11. 114

8.3 Magnitude and phase response for a 200 μm resonator from W11. 114

8.4 Magnitude and phase response for a 400 μm resonator from W12. 115

8.5 Magnitude and phase response for a 200 μm resonator from W12. 115

8.6 Magnitude and phase response for a 25 μm resonator from W11. 117

8.7 Loaded Qs for resonators from wafer W11. 117

8.8 Effect of poling condition on resonant frequency for a 200 μm resonator. 119

8.9 Effect of poling condition on the resonant frequency of a 80 μm resonator. 119

8.10 Temperature stability of a 200 μm resonator from W11. 121

8.11 Temperature stability of a 100 μm resonator from W11. 122

8.12 Fractional frequency change from Figures 8.10 and 8.11. 122

8.13 Effect of pressure on resonator Q. 124

8.14 Plot of the linear dampening coefficient vs. pressure. 126

8.15 Plot of the linear damping coefficient vs. frequency. 127

8.16 Calculated response based on measured values for damping and spring coefficients. 128

8.17 Measured response for 80 µm resonator from wafer W11. 128

8.18 Nonlinear Duffing behavior as a function of drive voltage and sweep direction. . 130

8.19 Calculated nonlinear damping coefficient. 132

8.20 Calculated nonlinear spring coefficient versus input power. 133

8.21 Measured nonlinear response of an 80 µm resonator driven at 60 mV. 135

8.22 Modeled response based on parameters extracted from Figure 8.21. 135

8.23 Overlaid response of a 100 and 400 µm resonator driven a 20 mV. 136

8.24 Nonlinear Duffing behavior as a function of operating pressure. 137

8.25 200 µm response from wafer W10 138

8.26 SEM of electrode area on 400 µm resonator shown in Figure 8.1. 139

8.27 LDV velocity spectrum for 400 µm resonator from wafer W3. 140

8.28 Measured mode shapes at frequencies 1 and 2 from Figure 8.27. 140

8.29 Measured mode shapes at frequencies 3 and 4 from Figure 8.29. 140

8.30 Electrical response of 400 µm resonator from W3 driven at the 10 mV drive voltage used for LDV testing. 141

8.31 LDV velocity spectrum for 400 µm resonator from wafer W9. 143

8.32 Measured mode shapes at frequencies 1 and 2 from Figure 8.31. 143

8.33 Measured mode shape at frequency 3 from Figure 8.31. 143

8.34 Alternative resonator design with a ½ length sense electrode. 144

8.35 LDV velocity spectrum response with ½ length sense electrode. 145

8.36 Measured mode shapes at frequencies 1 and 2 from Figure 8.35. 145

8.37 Second alternative design with PZT removed from center section. 146

8.38 LDV velocity spectrum of a 400 µm resonator with the PZT removed from between the electrodes. 146

8.39 Measured mode shapes at frequencies 1 and 2 from Figure 8.38. 146

8.40 Measured mode shapes at frequency 3 from Figure 8.38. 146

8.41 LDV velocity spectrum of a 400 µm resonator from wafer W9 with the PZT remove from between the electrodes. 147

8.42 Measured mode shape at frequency 2 from Figure 8.41. 147

8.43 Plot of ratio of neutral axis in the electrode section of the beam to the nonelectroded section of the beam. 148

8.44 Measured LDV velocity spectrum for resonators from wafers W1 - W9 149

8.45 LDV velocity spectrum for a 200 µm resonator from W1 at RT. 150

8.46 LDV velocity spectrum for same 200 µm resonator from W1 at 250 °C. 150

8.47 Measured mode shape at room temperature and 250ºC for a 400 µm resonator from wafer W8. 151

8.48 LDV velocity spectrum for single-drive excitation on W6. 152

8.49 LDV velocity spectrum for dual-drive excitation on W6. 152

8.50 LDV response for single-drive excitation of a 400 µm from W3. 153

8.51 LDV response for dual-drive excitation for a 400 µm resonator from W3. 153

8.52 LDV spectrum for a 400 µm resonator driven at a fundamental frequency. 155

8.53 LDV spectrum for a 400 µm resonator driven at the fundamental frequency. 155

9.1 Measured cantilever stress-induced tip deflections from wafer W13. 159

9.2 Modeled cantilever stress-induced deflection for a 300 µm resonator from wafer W13. 159

9.3 Measured cantilever stress-induced deflections from wafer W14. 160

9.4 Modeled cantilever stress-induced deflections for a 300 µm resonator from wafer W14. 160

9.5 SEM image of a fabricated generation III resonator from wafer W14. 161

9.6 Magnitude response for a 400 µm resonator from wafer W13. 163

9.7 Magnitude response for a 400 µm resonator from wafer W14. 163

9.8 LDV velocity spectrum response for 400 µm resonator from W14. 164

9.9 Measured mode shapes at frequencies 1 and 2 from Figure 9.9. 164

9.10 Measured mode shape at frequency 3 from Figure 9.9. 164

9.11 LDV velocity spectrum for a 400 µm resonator from wafer W13. 165

9.12 Measured mode shapes at frequencies 1 and 2 in Figure 9.11. 165

9.13 Measured mode shape at frequency 3 from Figure 9.11. 165

9.14 Comparison of measured frequency temperature response for oxide versus oxide-nitride-oxide beam structure. 166

Chapter 1. Introduction

1.1 Motivation for Research

The majority of filter and oscillator components used for Radio Frequency (RF) applications remain off-chip elements such as ceramic coaxial electromagnetic resonators or acoustic resonators such as surface acoustic wave (SAW) or bulk acoustic wave (BAW) resonators based on quartz or piezoelectric ceramic materials. These off-chip components typically offer relatively high quality factors (Q), smaller size, and increased temperature and frequency stabilities over traditional LC resonant circuits, but they remain a significant barrier to overall system miniaturization because of their inherent size, packaging complexity, and surrounding area required for assembly [1,2].

These resonators cover most of the RF spectrum shown in Figure 1.1 from Very Low Frequency (VLF) to Ultra High Frequency (UHF) and are used for applications such as AM, Ham, Short-wave, Citizen Band, and FM radios; Onstar; UHF and VHF television; radar; satellite communications; GPS; and wireless communications [3].

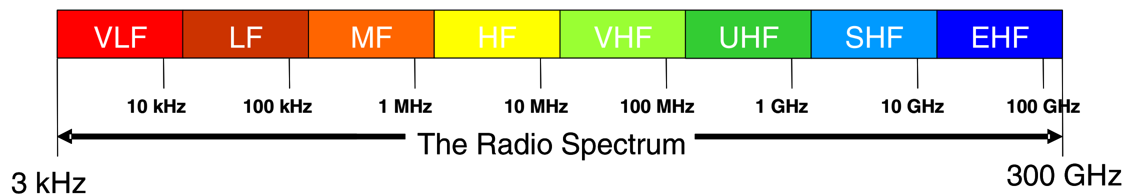

Figure 1.1 The Radio Frequency spectrum.

Film Bulk Acoustic Resonators (FBAR) are relatively new and are showing potential as a replacement for these off-chip components. They can be integrated on chip, have shown

performance similar to SAW devices, have good power handling capability, and only use an area of 50 to 300 μm^2 for the active device, or about 600 μm^2 for a full device, which is approximately 10% of the area of a traditional SAW resonator [4].

FBAR devices consist of thin film piezoelectric materials such as aluminum nitride (AlN), zinc oxide (ZnO), or lead zirconate titanate (PZT) sandwiched between metal electrodes and mounted on the surface of a substrate. When an alternating current is applied across the sandwich structure, the piezoelectric material expands and contracts, creating a vibration or acoustic wave within the material. In order to minimize loss into the substrate, either the substrate can be removed from under the device or the FBAR can be fabricated on top of an acoustic reflecting structure. For these devices, resonance occurs when the wavelength of the signal is equal to twice the thickness of the piezoelectric material. The wavelength within the material is given by

$$\lambda = \frac{c}{f} \tag{1.1}$$

where λ is the wavelength, c is the acoustic velocity in the material, and f is the frequency of the signal. Because of this relation to film thickness, and due to the current thickness ranges possible for the deposition of the piezoelectric thin films, FBAR devices are only applicable to the 2 GHz to 10 GHz frequency range.

One reason for the lack of commercialization for FBAR is this dependency on film thickness and the current manufacturing tolerances for the deposition processes used to set the resonator frequency and frequency tolerances. For example, the required

frequency tolerance for cell phone applications is 0.1%, which translates to a thickness tolerance of 0.1%, far below the typical process deposition tolerance of 5.0% [5]. Another disadvantage for some applications is that because the frequency is determined by the film thickness, the resonators on a single chip are typically limited to a single frequency unless several additional processing steps are used to either add or remove material in order to obtain resonators with different thickness and thus different frequencies.

The original resonant gate transistor was demonstrated by Nathanson *et al.* more than 35 years ago [6]. The work was abandoned because of poor Qs, temperature instabilities, and aging, but with improvements in materials and Microelectromechanical Systems (MEMS) processing over the years, work on MEMS resonators started again in the early 1990s [7]. Among the components currently targeted for replacement by MEMS are RF filters ranging from 800 MHz to 2.5 GHz, Intermediate Frequency filters ranging from 455 kHz to 254 MHz, and high-Q low-phase noise local oscillators ranging from 10 MHz to 2.5 GHz [8]. Nguyen has shown devices that could be replaced with MEMS resonators; Figure 1.2 shows a typical transmitter with current devices highlighted that could potentially be replaced by MEMS technology [8].

The majority of MEMS RF resonator research to date has been directed at using electrostatic transduction as the drive and sense mechanism for the resonator. These devices have ranged from comb-drive configurations for low frequency applications to clamped-clamped beam, free-free beam, and disk resonators for high frequency applications [9 - 13].

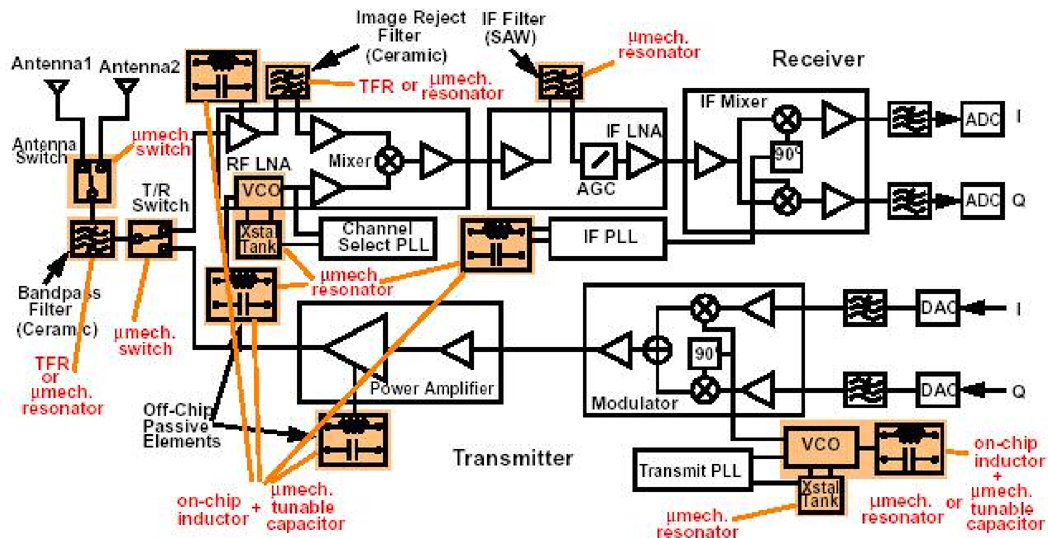

Figure 1.2 A typical transmitter schematic showing potential locations for MEMS resonator insertion.

While the resonant frequency of FBAR and related devices depends on film thickness, the resonant frequency of MEMS-based resonators operating in either bending modes or longitudinal (in-plane) modes depends on resonator length. Therefore, through photolithographic techniques there no longer needs to only be one filter or set of filters at one frequency, but hundreds to thousands of resonators in the same area as today's technology to enable the fabrication of parallel banks of switchable MEMS filters for tunable or variable band pass filters.

Electrostatic MEMS resonators have Qs above typical SAW, ceramic, and FBAR devices, and in some designs they approach the Qs of quartz BAW devices. Their demonstrated frequency range matches that of quartz but has not yet been demonstrated up to the UHF frequency range obtainable by SAW, ceramic, and FBAR devices. As

these electrostatic resonators are scaled to allow higher frequencies, the capacitive transducer gaps must also be scaled downward so that the electromechanical coupling strength can keep up with rising resonator stiffness to insure an adequately small series motional resistance for the device. As a consequence, for VHF and above frequencies, capacitive transducer gaps of less than 500 Å to 1000 Å are required. This constraint is driving electrostatic MEMS devices towards lateral and disk resonator designs, which tend to be easier to fabricate with these small gaps [15]. A concern regarding implementation of electrostatic MEMS resonator technologies for RF applications is the nonlinearity in its capacitive transducer for VHF resonator applications and low power handling due to the need for small electrode to resonator gaps [16]. Table 1.1 summarizes the performance of several electrostatic RF MEMS resonators reported in recent years.

Table 1.1 Electrostatic MEMS resonator references.

Device Type	Typical Frequency Range	Typical Q	Reference
Electrostatic comb drive	8 kHz-0.5 MHz	80000	[14]
Electrostatic clamped-clamped beam	8.5 MHz	8000	[8]
Electrostatic vertical free-free beam	92 MHz	7450	[8]
Electrostatic lateral free-free beam	10.47 MHz	10743	[15]
Electrostatic disk resonator	156 MHz	9400	[15]
Hollow disk ring resonator	1.2 GHz	14,600	[2]

Piezoelectric transduction is an alternative to electrostatic transduction for MEMS resonators and offers the potential advantage of increased electromechanical coupling strength, inherently linear performance, and an elimination of the need for small electrode gaps potentially leading to larger power handling. Piezoelectric transduction is already being considered for use in UHF applications through the use of FBAR devices, and MEMS fabrication technologies could extend this application range for piezoelectric materials to the LF to VHF frequency ranges.

Devices using piezoelectric thin films as the piezoelectric material have been used as actuators and sensors in MEMS applications [17 - 19]. DeVoe applied this technology for RF resonators by exploring the use of ZnO for piezoelectrically actuating and sensing resonance in a piezoelectric MEMS resonator [20]. DeVoe showed that the ratio of the piezoelectric coupling strength for a clamped-clamped beam to that of a parallel capacitive plate is given by

$$\frac{\eta_{piezo}}{\eta_{plate}} = \left(\frac{2.91 d_{31} E_p h_c b g^2}{h \varepsilon_0 V_b} \right) \frac{1}{L^2} \tag{1.2}$$

where η is the respective coupling coefficient, b is the beam width, d is the transverse piezoelectric modulus, E_p is the Young's Modulus of the piezoelectric film, h_c is the thickness of the piezoelectric film, h is the thickness of the electrostatic beam, g is the capacitive gap spacing, ε is the air permittivity, V_b is the applied electrostatic voltage, and L is the beam length. Then, since resonant frequency for a clamped-clamped beam is inversely proportional to the square of the beam length

$$\omega \propto 1/L^2, \tag{1.3}$$

the ratio of the coupling strength of a piezoelectric device to an electrostatic parallel plate device is proportional to the resonant frequency

$$\frac{\eta_{piezo}}{\eta_{plate}} \propto \omega_1. \tag{1.4}$$

DeVoe also showed that

$$\frac{Y_{piezo}}{Y_{plate}} \propto \omega_1^2, \tag{1.5}$$

where Y is the resonator admittance which is a measure of the output current for a given input voltage [20]. Equations (1.4) and (1.5) indicate that for higher resonant frequencies, piezoelectric transduction should offer increasingly stronger electromechanical coupling relative to capacitive resonators and therefore potentially better performance as bending-mode MEMS resonators are pushed higher into the VHF frequencies.

DeVoe fabricated and demonstrated clamped-clamped single and triple-beam piezoelectric resonators that utilized ZnO for the piezoelectric material. A sketch for the single beam clamped-clamped resonator concept is shown in Figure 1.3 [20]. An explanation of the operational concept for these resonators is given in Chapter 2.

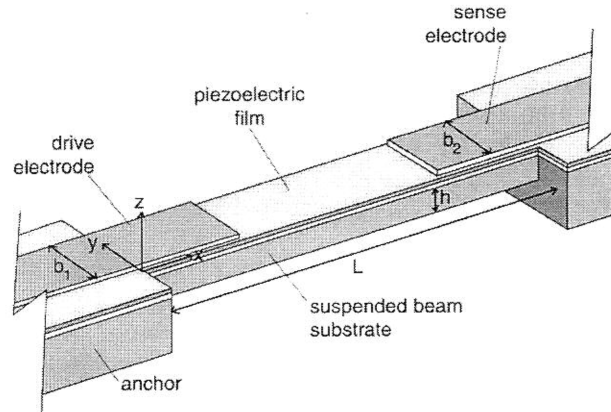

Figure 1.3 Concept for a piezoelectric resonator.

The relative admittance for these clamped-clamped piezoelectric beam resonators can be given as

$$Y_{21} = \frac{j\omega(2.46(d_{31}E_p h_c b / L))^2}{M\omega_1^2[1-(\omega/\omega_1)^2 + j(\omega/\omega_1)(1/Q)} \text{ [20].} \quad (1.6)$$

Therefore, higher admittance for a piezoelectric resonator can be obtained by achieving higher Qs and by using piezoelectric materials with higher piezoelectric coupling parameters. Table 1.22 shows some relative piezoelectric constants for various piezoelectric materials [18].

Table 1.2 Reported piezoelectric properties for ZnO, AlN, and PZT.

Material	d_{33} (pC/N)
ZnO	12.4
AlN	5.0
sol-gel PZT	233

From Table 1.2, PZT has an order of magnitude higher d_{33} coefficient than ZnO and AlN. While devices using PZT thin films have been used as actuators and force sensors, little work has been reported on thin-film PZT resonators for communication systems in the LF to VHF frequency range. Examples of lower frequency applications using PZT thin films can be found in the following:

- Brooks *et al.*, used PZT thin films for silicon cantilever beam resonance [21]. These devices ranged from 200 μm to 1000 μm with resonant frequencies below 350 kHz.

- Hong *et al*. fabricated and tested PZT-based resonant cantilevers for BioMEMS applications with resonant frequencies below 50 kHz [22].

- Zang *et al.*, fabricated PZT bridge resonant structures with the application to accelerometers. These were relatively large structures (300 μm x 1000 μm) with a fundamental mode of 8.2 kHz and a low Q of less than 500 [23].

This research focuses on examining the potential benefits and limitations of sol-gel PZT piezoelectric thin films versus ZnO thin films for application to piezoelectrically driven RF microeletromechanical systems (MEMS) resonators in the LF to VHF frequency range. Issues addressed include fabrication methods, stress gradients resulting from the inherently asymmetric multi-material/layer designs, lack of characterized material properties, requirement to electrically pole the PZT films, temperature stability, development of finite element models (FEM), validation of the resonator mode shapes, the boundaries for linear performance, and a comparison of the overall quality factor and

electrical response versus reported values for electrostatic and ZnO piezoelectric resonators. Some of the initial research results have been published and can be found in references [24 - 26].

1.2 Additional Research

During the course of this research, the techniques developed for fabricating devices, some of the actual fabricated devices, and many of the test results reported within this dissertation have been used to support additional research, including three masters' degree theses at the University of Maryland and associated publications on MEMS free-free beam PZT resonators [27], finite element modeling of clamped-clamped beam PZT resonators [28], and clamped-clamped beam resonator equivalent circuit simulation [29].

Chapter 2. Background

2.1 Piezoelectricity

The piezoelectric effect was discovered by Pierre and Jacques Curie in the late 1800s and occurs in materials with dipole moments resulting from non-centrosymmetric crystal structures. The direct piezoelectric effect occurs when a charge is generated due to a change in the dipole movement caused by the application of a mechanical stress to the crystal. The converse piezoelectric effect occurs when a strain is generated on the crystal by the application of an electric field. A full review of piezoelectric crystals and piezoelectric ceramics can be found in the work by W. G. Cady and B. Jaffe [30, 31].

Quartz crystals in bulk resonators are examples of natural piezoelectric crystals. A subclass of piezoelectric materials consists of pyroelectric materials that are spontaneously polarized during deposition, contain a unique polar axis in the unstrained condition, and thus exhibit piezoelectric properties in the as-deposited state. Because of this unique polar axis, pyroelectric materials generate a charge when uniformly heated. In a quartz crystal, the dipoles are arranged in several compensating directions such that no net charge is seen with application of uniform heating. ZnO and AlN are examples of common pyroelectric materials.

Ferroelectric materials are a further subclass of pyroelectric materials that require the application of an electric field after deposition to polarize them. A unique feature of a ferroelectric material is that the polarity can be reversed by applying an electric field in the opposite direction.

PZT is an example of a ferroelectric ceramic that is made up of randomly oriented small crystals. Areas of uniform polarization, called domains, are formed to minimize intergranular stress as the PZT is cooled during processing. In the as-deposited state, these domains are typically randomly oriented within the film and cancel each other out so that there is no net piezoelectric effect when a small electric field is applied. However, if an electric field of enough strength is applied to the film, the dipoles will reorient themselves in the direction of the field, and the film will become polarized as shown in Figure 2.1

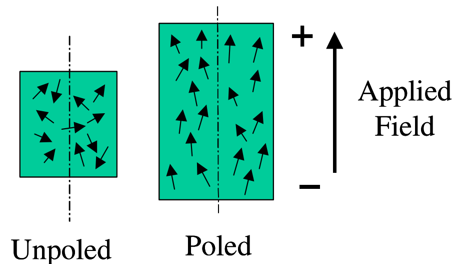

Figure 2.1 Unpoled and poled ferroelectric domain state orientations.

The field required to cause this reorientation of the domains is called the coercive field (E_c). The remnant polarization (P_R), or charge remaining on the film after polarization, is a measure of the piezoelectric performance of the material. Figure 2.2 shows a typical hysteresis loop of dielectric displacement versus applied field [31]. Typically, a high P_R value is required for a ceramic film to exhibit good piezoelectric properties.

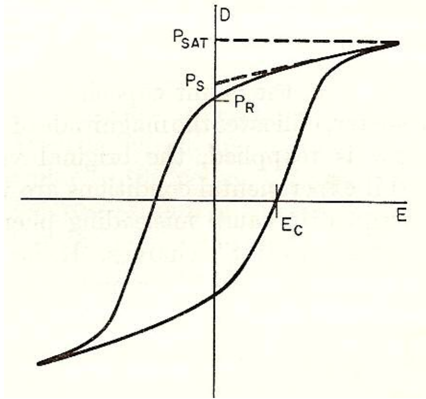

Figure 2.2 Typical hysteresis curve for a piezoelectric ceramic.

It is important to note that above a certain temperature, there will be enough energy for the dipoles to shift without the application of an external field and the film will transition to an unpolarized state. The temperature at which this transition occurs is called the Curie temperature. The piezoelectric response for ferroelectric materials has both intrinsic and extrinsic contributions. The intrinsic contribution is due to the response of the single domains and the extrinsic response is due the actual domain wall switching.

2.2 Sol-Gel PZT

PZT is a ferroelectric ceramic that exhibits some of the highest thin film piezoelectric properties and it has the perovskite cubic crystalline structure depicted in Figure 2.3. Below the Curie temperature, in the composition range typically used by MEMS devices, PZT exhibits a non-cubic rhombohedral or tetragonal distortion depending on the Zr to Ti ratio. Figure 2.4 shows the different non-cubic structures as a function of PZT composition [31]. These non-cubic structures have shifted Ti or Zr cations leading to the creation of dipoles. The position of the cation within the oxygen cage can be shifted with an applied electric field, giving PZT its ferroelectric properties.

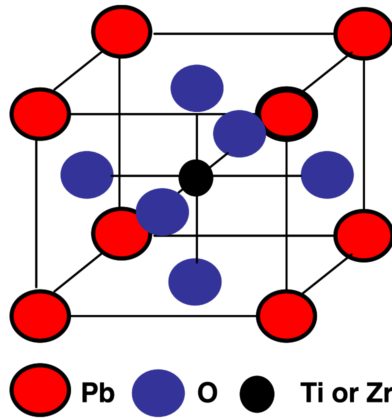

Figure 2.3 Perovskite crystal structure.

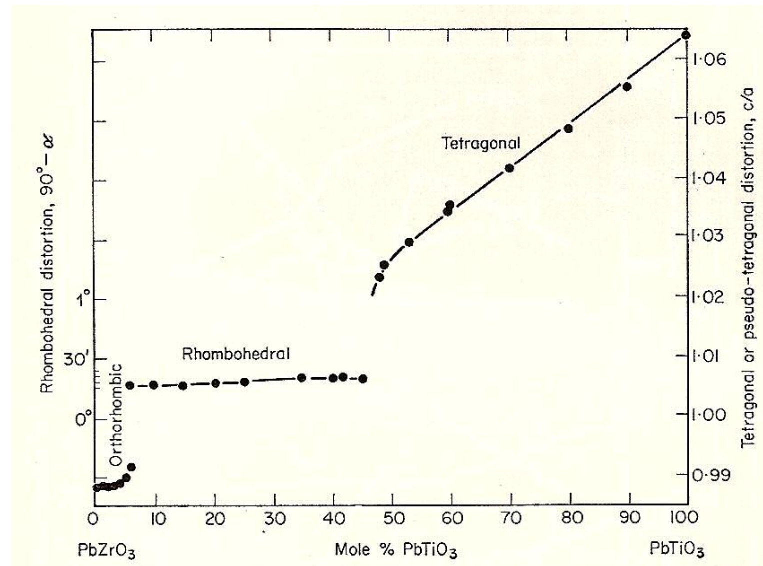

Figure 2.4 Unit cell distortion of PZT versus mole % $PbTiO_3$ at room temperature.

A morphotropic phase boundary occurs near the 52/48 percent Zr/Ti ratio. PZT compositions near this morphotropic phase boundary have both rhombohedral and tetragonal structure, increasing the number of polarization directions and giving the highest piezoelectric constants, dielectric constants, and electromechanical coupling factors [32]. For this reason, a process to develop sol-gel based 52/48 PZT thin film was developed at the U.S. Army Research Laboratory (ARL) under a joint DARPA program

with Penn State University [33]. This process uses a modification of the procedure described by Budd, Dey, & Payne [34]. The ARL process uses lead acetate trihydrate, titanium-IV isopropoxide, and zirconium-IV propoxide as precursors and 2-methoxyethanol as a solvent. Formamide (4 vol%) is added as a drying control agent after refluxing. The resultant PZT solution has a concentration of 0.4 M.

The starting substrates for the sol-gel PZT deposition are prepared by initially depositing a 0.05 μm to 2.0 μm plasma enhanced chemical vapor deposition (PECVD) silicon dioxide layer on a (100)-oriented silicon wafer, followed by a sputtered 200 Å Ta or Ti adhesion layer, and finally a 850 to 1700 Å sputtered Pt layer. The PZT deposition process starts by using a syringe with a 0.1 μm filter to deposit the PZT solution onto the stationary substrate prior to spinning for 30 seconds at 2500 rpm. The wafer is then transported to a hotplate for pyrolysis at 350°C for 2 minutes. A crystallization process is performed after every four deposition and pyrolysis loops. The crystallization is performed in a rapid thermal annealing (RTA) furnace using a dwell at 700°C for 30 seconds. This final crystallization step is performed in a RTA above 650°C in order to avoid the formation of the metastable pyrochlore phase that does not have the ferroelectric properties of the pervoskite phase [35, 36]. Deposition, pyrolysis, and crystallization continued until the final desired film thickness of 0.25 μm to 2.0 μm is achieved. This Si/SiO_2/Pt/PZT stack is the typical starting substrate for many MEMS applications. The 850 to 1700 Å Pt top electrode can either be sputter-deposited in a blanket film for later patterning by etching or by sputtering over photoresist for lift-off patterning of the top electrode. The basic process is described in Figure 2.5, and a

detailed description can be found in the ARL technical report ARL-TR-2895 [37]. The resulting PZT films typically have a coercive field above 45 kV/cm, dielectric constants above 800, and remnent polarizations above 20 $\mu C/cm^2$.

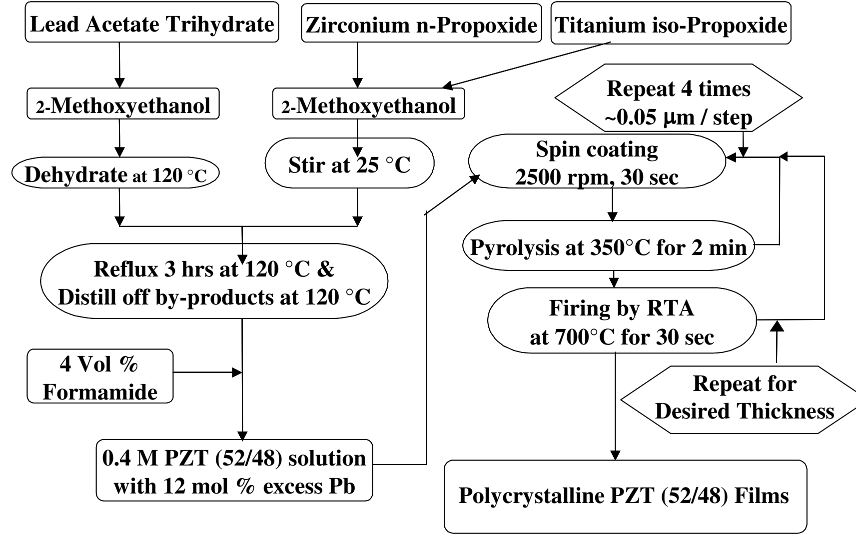

Figure 2.5 Sol-gel PZT deposition process flow diagram.

2.3 Piezoelectric Actuation and Sensing

Figure 2.6 depicts the direct and converse piezoelectric effects. The equations of state relating the electric and elastic variables for the piezoelectric element are [31]

$$S_1 = s_{11}^E T_1 + s_{12}^E T_2 + s_{13}^E T_3 + d_{31} E_3 \tag{2.1}$$

for strain generated in the x direction by an applied stress and electric field and

$$D_3 = d_{31}(T_1 + T_2) + d_{33} T_3 + \varepsilon_3 E_3 \tag{2.2}$$

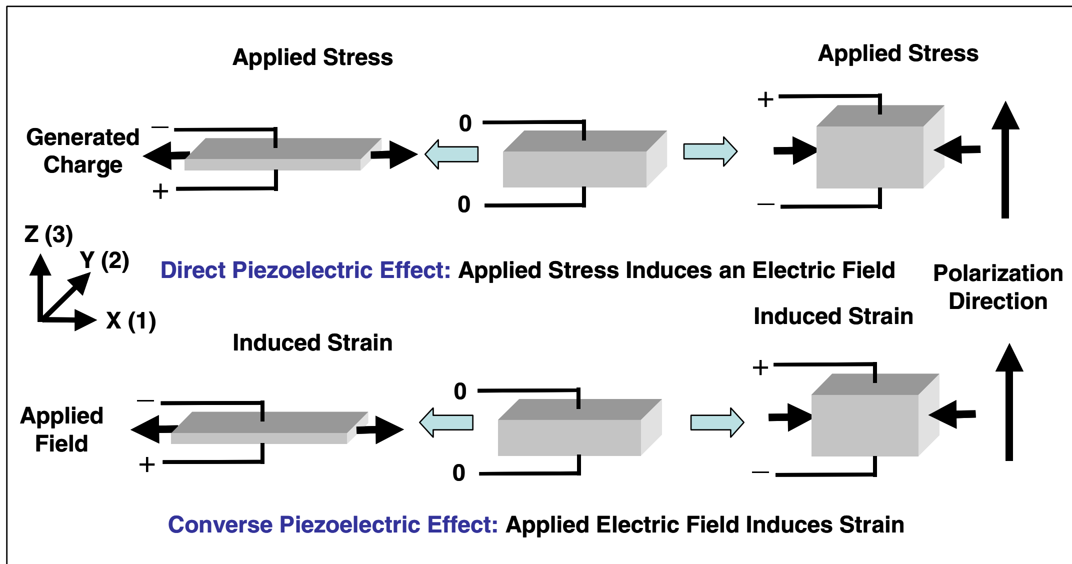

Figure 2.6 Visualization of the direct and converse piezoelectric effect.

for the electric charge generated by an applied stress and electric field. In (2.1) and (2.2) *S* is the strain, *T* is the stress, *s* is the elastic compliance, *d* is the piezoelectric constant, *E* is the electric field intensity, *D* is the electric charge generated, and ε is the material permittivity. Therefore from (2.1), in the absence of an applied stress, an applied electric field in the z or (3) direction results in a strain in the x or (1) direction via the piezoelectric coupling coefficient d_{31}. Likewise, from (2.2) in the absence of an electric field, an applied stress in the x direction results in a charge in the z direction via the piezoelectric coupling coefficient d_{31}. The efficiency of this conversion of mechanical energy to charge or charge to mechanical energy is given by the piezoelectric coupling coefficient

$$k^2 = \frac{Mechanical\ Energy\ Converted\ to\ Electrical\ Charge}{Mechanical\ Energy\ Input} \tag{2.3}$$

$$k^2 = \frac{Electrical\ Energy\ Converted\ to\ Mechanical\ Displacement}{Electrical\ Energy\ Input} \qquad (2.4)$$

If an additional material layer is used to move the piezoelectric material off of the neutral axis of a beam, the induced strain in the piezoelectric material when an electric field is applied generates a moment that causes the beam to bend. Figure 2.7 illustrates this where E is the direction of the applied field, P is the direction of polarization, and D is the polarity of the generated charge if the tip is mechanically deflected in the absence of an applied electric field. The direction of movement depends on the direction of polarization and the polarity of the applied field.

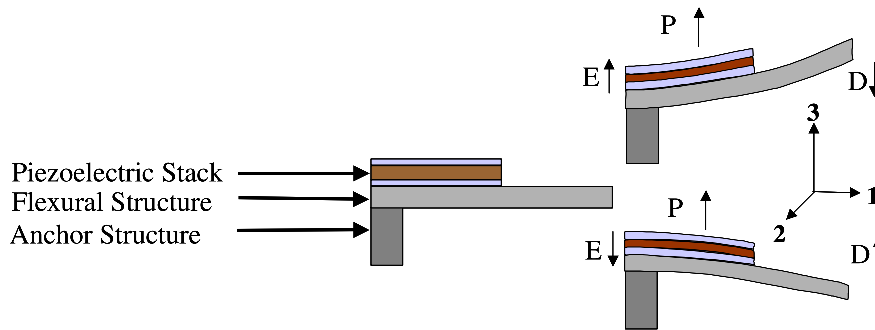

Figure 2.7 Actuation and sensing mechanism using piezoelectric thin films.

If the input electric field is an RF signal that matches the natural resonant frequency of the beam, the resultant strain from the converse piezoelectric effect can induce resonance of the beam. Likewise, a resonating beam can generate a charge via the direct piezoelectric effect at the resonance frequency of the beam.

From (2.1), the maximum strain that can be induced in the piezoelectric element by an applied field is given by

$$\varepsilon_{\max} = d_{31}\left(\frac{V}{t_p}\right), \qquad (2.5)$$

where V is the applied voltage and t_p is the thickness of the piezoelectric layer. The maximum force (block force) that can be generated when the piezoelectric element is held in the zero strain condition is given by

$$F_{\max} = d_{31}EbV, \qquad (2.6)$$

where E is the Young's modulus of the piezoelectric element, b is the width of the element, and V is the applied voltage. In almost all applications, the piezoelectric element is mounted or attached to a substrate. The inclusion of a substrate can cause a reaction force to the piezoelectric-induced strain that reduces the actual amount of induced strain from the maximum that can be achieved in (2.5). The relation between the maximum strain and maximum force can be plotted as the force-strain relation for the element, as shown in Figure 2.8.

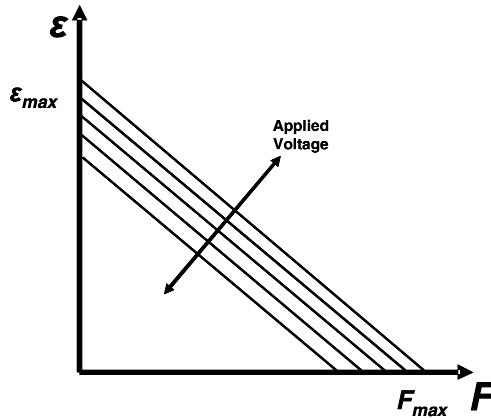

Figure 2.8 Force-strain relationship for a piezoelectric element.

When the piezoelectric element is attached to the surface of a beam such as the cantilever in Figure 2.7, the force generated by the piezoelectric element generates an applied moment at the end of the electrode

$$M_b = F_p \frac{t_b}{2}, \tag{2.7}$$

where M_b is the moment generated on the beam, F_p is the force generated by the piezo element, and t_b is the underlying material thickness. If the electrode thickness and material are not considered, the strain on the top surface of the beam can then be given as

$$\varepsilon_b = \frac{M_b t_b}{2E_b I_b} = \frac{F_p}{E_b I_b}\left(\frac{t_b}{2}\right)^2, \tag{2.8}$$

where E_b is the Young's Modulus of the beam and I_b is the area moment of inertia for the beam. The elongation of the top surface of the beam is then given by

$$\Delta l_b = \frac{F_p}{E_b I_b}\left(\frac{t_b}{2}\right)^2 l_p, \tag{2.9}$$

where l_b is the beam length and l_p is the piezoelectric element length. The induced bending moment is a reactive force that will reduce the piezoelectric element extension by the following

$$\Delta l_p = d_{31}\frac{V}{t_p} l_p - \frac{F}{E_p b_p t_p} l_p. \tag{2.10}$$

For displacement compatibility $\Delta l_b = \Delta l_p$, then by substituting and reducing, the resultant equation for the force generated in the piezoelectric element is given by

$$F_p = 12 \frac{d_{31} V}{t_p t_b^2} \frac{E I_b E I_p}{3 E I_b + 4 E I_p}, \tag{2.11}$$

and likewise, the generated moment is given by

$$M = F \frac{t_b}{2} = 6 \frac{d_{31} V}{t_p t_b} \frac{E I_b E I_p}{3 E I_b + 4 E I_p}. \tag{2.12}$$

If (2.11) is substituted back into (2.9), the amount of strain induced into the beam is given by [38]

$$\varepsilon_b = \frac{\Delta l_b}{l_p} = \frac{F_p}{E_b I_b} \left(\frac{t_b}{2} \right)^2 = 3 \frac{d_{31} V}{t_p} \frac{E I_p}{3 E I_b + 4 E I_p}. \tag{2.13}$$

Therefore, the amount of strain induced into the beam is not only dependent on the voltage applied but also on the thickness and stiffness of both the beam and the piezoelectric element.

From equation (2.13), if the oxide beam is too stiff, the actuator will not induce any displacement. Likewise, if the beam is too soft, the beam will only stretch under the drive electrode. The optimization of the SiO_2 thickness for a given PZT thickness can be done by mechanical impedance matching the piezoelectric actuator and the beam as shown in

equations (2.14) through (2.16) [39]. The mechanical impedance of the piezoelectric actuator can be given by

$$Z_p = \frac{bt_p k E_p}{j\omega \tan\left({kL_e}/{2} \right)}, \tag{2.14}$$

where b is the width, t_p is the thickness, E_p is the Young's modulus, ω is the frequency, L_p is the piezoelement length, and k is the wave number. The beam impedance is given by

$$Z_p = \frac{4M_p}{j\omega \left(\frac{t_b}{2} + t_{pt} + \frac{t_{PZT}}{2} - t_{off} \right)^2 \left(w_{x_2} - w_{x_1} \right)}, \tag{2.15}$$

where M_p is the moment acting on the beam, t_b is the beam thickness, t_{pt} is the bottom Pt thickness, t_{pzt} is the PZT thickness, t_{off} is the neutral axis offset and w_x is the deflection at the beginning and end of the top electrode. Impedance matching is performed by setting Z_p=Z_b and solving for t_b by using the beam boundary conditions to reduce the problem to

$$\frac{E_b}{6E_p} = \frac{t_p}{t_b} \left(\frac{t_b}{2} + t_{pt} + \frac{t_p}{2} - t_{off} \right)^2. \tag{2.16}$$

Equation (2.16) can then be solved to optimize the beam thickness for a given PZT thickness.

2.4 Piezoeletric Resonator Concept

The resonator concept used for this work follows that demonstrated by DeVoe for ZnO based piezoelectric resonators and is shown in Figure 2.9.

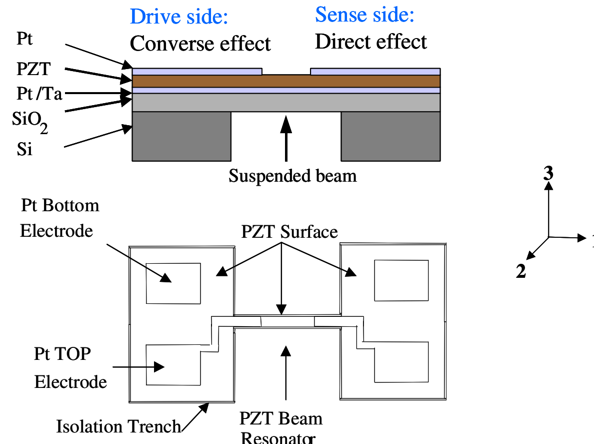

Figure 2.9 Top view and cross-section of a piezoelectric MEMS resonator.

The input drive voltage generates an electric field between the top and bottom electrode and induces a strain in the drive side (port 1) of the resonator through the converse piezoelectric effect. This strain results in a concentrated moment applied at the terminal edge of the input electrode. When the input voltage frequency is near the fundamental frequency of the beam, resonance occurs in the beam and amplifies the piezoelectric strain on the sense side (port 2) of the resonator. This induces a current in port 2 at the resonant frequency of the beam through the direct piezoelectric effect. Therefore, the device can be used to drive a given frequency as in a clock application or filter frequency data in a filter application.

Admittance is the overall ability of an electric circuit to pass alternating current. By using the piezoelectric constitutive equations and modal analysis DeVoe followed a similar method to Tilmans *et al.* to show that the transfer function describing the admittance Y_{21} of a clamped-clamped resonator in terms on the electro-mechanical properties as

$$Y_{21} = \left(\frac{Z(j\omega)}{F(j\omega)}\right)\left(\frac{F(j\omega)}{V_1(j\omega)}\right)\left(\frac{I_2(j\omega)}{Z(j\omega)}\right) = \frac{I_2(j\omega)}{V_1(j\omega)} = j\omega\frac{Z(j\omega)}{F(j\omega)}\eta_1\eta_2 \qquad (2.17)$$

$$\eta_1 = \frac{F(j\omega)}{V1(j\omega)} \qquad (2.18)$$

$$\eta_2 = \frac{Q_2(j\omega)}{Z(j\omega)} = \frac{1}{j\omega}\frac{I_2(j\omega)}{Z(j\omega)} \qquad (2.19)$$

where Q_2 is the generated charge at port 2, I_2 is the output current at port 2, V_1 is the input voltage at port 1, Z is the generalized beam displacement, F is the distributed normal load, and η_1 and η_2 are the electromechanical coupling coefficients at port 1 and port 2 [20]. The modal force can be given by

$$F_1 = \int_0^L F(x)'\phi_1(x)dx\,, \qquad (2.20)$$

where the equation for the fundamental mode shape of a clamped-clamped resonator is given by

$$\phi(x) = \sinh(\beta x) - \sin(\beta x) + \alpha[\cosh(\beta x) - \cos(\beta x)]\,. \qquad (2.21)$$

Considering only the fundamental mode, the first term in (2.17) or the modal transfer function is given by

$$\frac{Z(j\omega)}{F(j\omega)} = \frac{1}{M\omega_1^2\left(1-\left(\omega/\omega_1\right)^2 + j\left(\omega/\omega_1\right)\left(1/Q\right)\right)} \tag{2.22}$$

where M is the generalized mass and Q is the generalized quality factor given by

$$M = \int_0^L \rho bh\phi^2(x)dx \cong 1.036\rho bhL \tag{2.23}$$

$$Q = \omega_1 \frac{M}{C} \tag{2.24}$$

$$\omega_1 = (\beta L)^2 \sqrt{\frac{EI}{\rho bhL^4}} \tag{2.25}$$

where C is the generalized damping term, ω_1 is the fundamental frequency, ρ is density, b is beam width, h is beam thickness, βL is a constant and equal to 4.73 for doubly clamped beams, and L is the beam length. From these it can be shown that the overall admittance is given by [20]

$$\frac{I_2}{V_1} = \frac{-j\omega\left(\frac{d_{31}t_eE_p}{2}\right)^2\left(\int_0^L b_1(x)\phi(x)dx\right)\left(\int_0^L b_2(x)\phi''(x)dx\right)}{M\omega_1^2\left[1-\left(\frac{\omega}{\omega_1}\right)^2 + j\frac{\omega}{\omega_1}\frac{1}{Q_1}\right]}. \tag{2.26}$$

From Equation (2.26), in addition to d_{31} and Q, the electrode shape has an effect on the admittance or amount of charge generated by the resonator for a given input voltage. By looking at equation (2.21), a maximum for ϕ'' occurs at x=L/4 and x=3L/4 and therefore the maximum admittance can be achieved by using quarter-length electrodes. For electrodes clipped at the quarter- and three-quarter lengths, the electrode width can be written as

$$b_1(x) = b[1 - u(x - L/4)] \text{ and} \tag{2.27}$$

$$b_2(x) = b[1 - u(x - 3L/4)] \tag{2.28}$$

where $u(x-x_0)$ is the unit step function. Then, coupling coefficients and the overall resonator admittance reduce down to

$$|\eta_1| = |\eta_2| = -\left(\frac{4.92}{2}\right)\frac{d_{31}h_e E_p b}{L} \text{ and} \tag{2.29}$$

$$\frac{I_2}{V_1} = \frac{-j\omega\left(2.46\left(d_{31}h_e E_p b \big/ L\right)\right)^2}{M\omega_1^2\left[1 - \left(\frac{\omega}{\omega_1}\right)^2 + j\frac{\omega}{\omega_1}\frac{1}{Q_1}\right]}. \tag{2.30}$$

Figures 2.10 shows equation (2.30) plotted as a function of frequency, over a factor of 10 range in the value of Q and d_{31}.

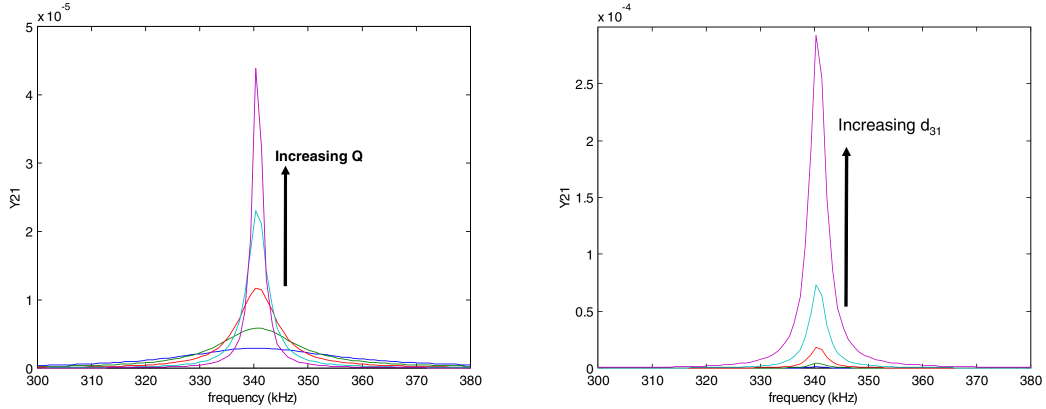

Figure 2.10 Equation (2.30) plotted over a factor of 10 for the value of Q and d_{31}.

From Figure 2.10, increasing the Q of the resonator and especially going to piezoelectric materials with higher d_{31} coefficients can have a significant effect on the admittance or magnitude of the filtered signal. One of the goals of this work is to demonstrate that the higher piezoelectric coefficient of PZT versus ZnO would lead to larger admittance and resonator response. Discussions on the electrical equivalent circuit for the clamped-clamped beam resonator can be found in the work of DeVoe and Lynch [29, 40] and for general piezoelectric resonators in the work of Ballato, Söderkvist, and Zelenka [41 - 44].

Chapter 3. Fabrication Process Development

3.1 Overall Process Flow

A five-mask process was developed to define and suspend the resonators fabricated for this research. The basic process flow is shown in Figure 3.1.

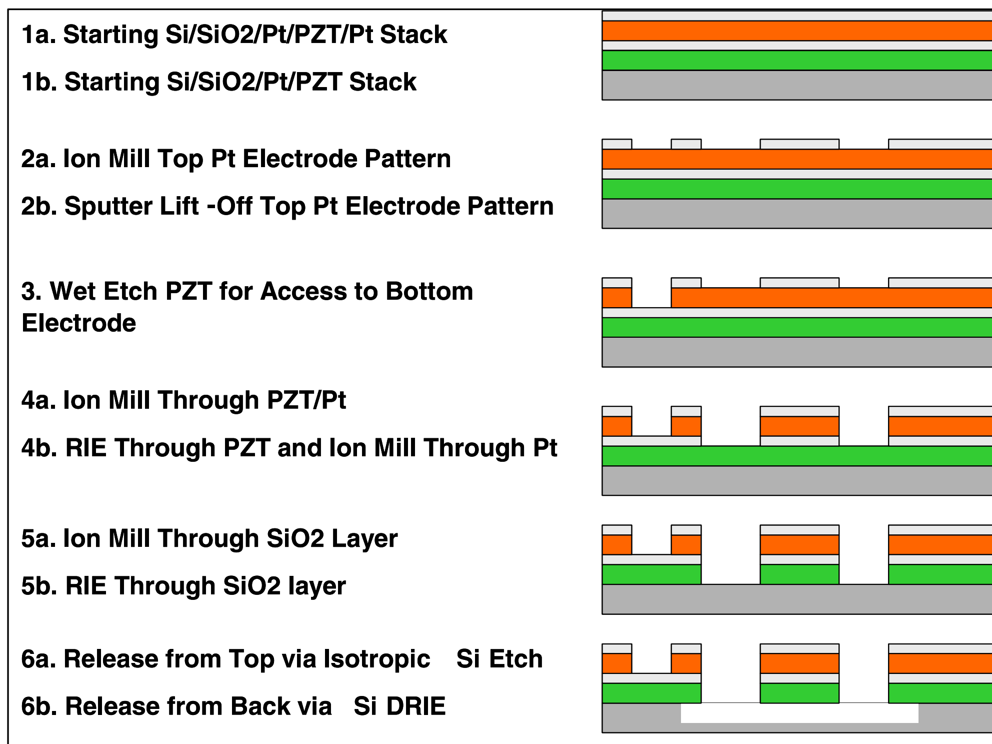

Figure 3.1 Piezoelectric resonator fabrication process flow.

There are several processing options for the process flow depicted in Figure 3.1, even with the same mask set, as depicted by options (a) and (b) for several of the processing steps. For example, the top electrode can be patterned by blanket coating the Pt film and then etching back or by performing standard Pt lift-off techniques.

The starting substrates were made by depositing sol-gel PZT films with a 52/48 Zr/Ti ratio on metalized (Si/SiO_2/Ti/Pt) 100 mm silicon wafers per the method described in Chapter 2. The next steps involved patterning the top electrode, creating an opening for contacting the bottom electrode, defining the resonator beam length and width, and finally releasing the resonator to created a suspended beam structure.

3.2 Top Electrode

Two methods were used for forming the top electrodes for the resonators fabricated during this research. The first method used a Varian 3190 sputter deposition system to deposit a blanket film of Pt over the starting PZT substrate surface. Typically a RF clean was performed and a 200 nm Ti adhesive layer was deposited prior to the Pt deposition. This Pt surface was subsequently patterned with photoresist using a light field mask and a positive tone resist (AZ 5214e) to define the electrode areas. The unwanted top Pt was then removed in a Commonwealth argon ion milling system. The argon ion milling process is not selective to the underlying PZT and the etch depth is controlled by knowing the etch rate and using a timed etch. This is represented by steps 1a and 2a in Figure 3.1.

The second method sputter deposits the Pt film over a patterned photoresist layer on top of the starting PZT substrate. This photoresist layer uses the same light field mask as the blanket coat but uses a reverse image process with AZ 5214e photoresist. The openings in the resist then represent the desired electrode contact areas whereas in the previous process they represented the metal to be removed. Pt lift-off was then performed by placing the wafers in acetone or PRS-3000 photoresist stripper to dissolve the photoresist

and lift off the unwanted Pt leaving behind the top electrode pattern. This technique requires fewer steps than the blanket coat approach with the trade-off of requiring a lower metal deposition temperature (100 °C or less) because of the photoresist and potentially reduced adhesion to the PZT.   This process is represented by steps 1b and 2b in Figure 3.1.

3.3 Bottom Electrode

Two different PZT etching methods were then employed to create openings to access the bottom electrode through the PZT layer. In the first method, an isotopic wet etch (H_20/HCL/HF - 280ml/120ml/4 drops) was used. This method can be used when there is no top Pt around the opening, pattern accuracy is not a priority, and a totally dry process is not required. The advantage is that it is simple and quick, requiring only a dark field photoresist mask, patterned positive tone photoresist, and approximately 40 seconds of wet etching. The disadvantage is that if there is top Pt is present around the opening, undercutting of the Pt can occur and the Pt can sag and potentially short the device. This process is represented by step 3 in Figure 3.1.

In the second method, reactive ion etching (RIE) of the PZT was performed in a Plasma Therm 720 Shuttlelock system using HC_2ClF_4 as the etch gas. This process was detailed by Zeto *et al*. [45]. The method uses the same mask and tone resist as the wet etch. Both methods have been successfully demonstrated for resonator fabrication. The disadvantage of the RIE technique that was used is that for the temperatures and pressures used the etch is primarily a milling process with no reactive species, so it is slow and there is a potential for resist burning and potential loss of the device. This technique was used to

fabricate some early devices, but it was eventually dropped for the quicker and easier wet etch process.

3.4 Resonator Formation

The third step was to pattern and form the resonator shape (length and width). Again, two different processes were used during the course of this research. In the first method, the resonator shape was patterned using a light field mask and positive tone resist to protect the area and the surrounding bottom Pt/PZT stack is removed by using argon ion milling. In the initial device, re-deposition of the Pt was a problem because of the near-normal incident ion milling process. This showed up as shorting between the top and bottom electrodes or as fencing on the photoresist as is shown in Figure 3.2 after resist removal.

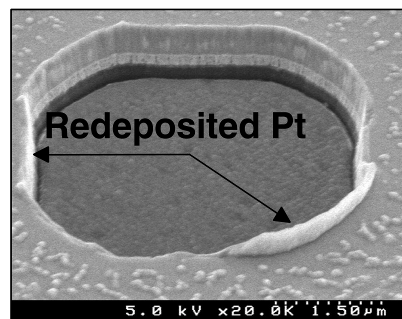

Figure 3.2 Pt redeposition and fencing after photoresist removal.

This redeposited Pt fence had a tendency to break off and lead to additional shorting problems across the wafer as shown in Figure 3.3.

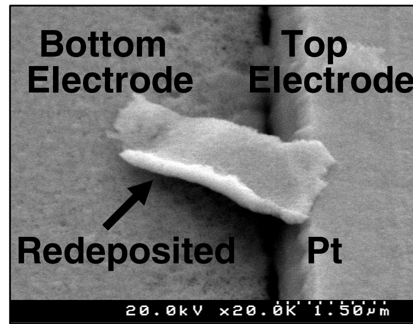

Figure 3.3 Pt flake shorting the PZT structure.

A process was developed to Ion mill at a 40° angle from the incident beam during the Pt portion of the ion mill process to eliminate the redeposition of Pt by milling the redeposited Pt from the sidewalls at the same time as the vertical etch. If the 40º angle ion milling process defined for the top and bottom electrode is used through the entire stack, redeposition will not be a problem. However, very uneven sidewall profiles result from angled milling through the entire structure as seen in Figure 3.4 because of mask erosion.

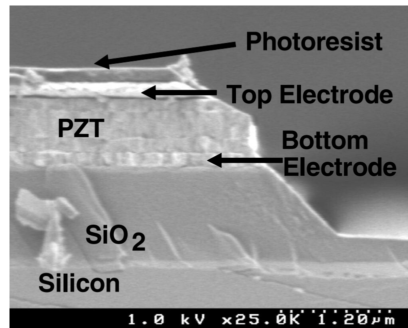

Figure 3.4 PZT stack cross section after ion milling at a constant 40° angle.

Another solution that was tried was using hard baked photoresist and ion milling with a near normal incident beam at 5° from normal incidence. This created an eroding mask and an angled sidewall profile enabling the ion mill to etch away any redeposited Pt from the sidewalls as shown in Figure 3.5. The drawback to this method is that pattern

resolution is reduced and the beams will have a nonuniform cross-section due to the sloping sidewalls.

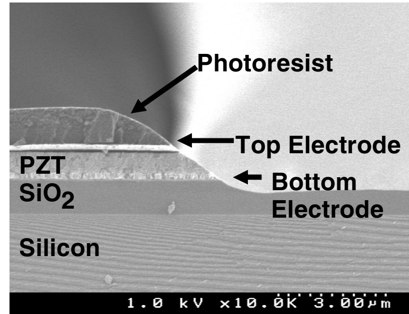

Figure 3.5 PZT stack cross section after ion milling at a constant 5° with a hard baked photoresist mask.

The best results were obtained by going to a combination ion milling approach that uses multiple angles to perform the ion milling. A 40° angle is used for ion milling through both the top and bottom Pt and a 5° angle is used for ion milling through the PZT. The resultant structure has very good pattern resolution and near vertical sidewalls resulting in well-defined beams with less the one-half micron variation in beam width from top to bottom as seen in Figure 3.6.

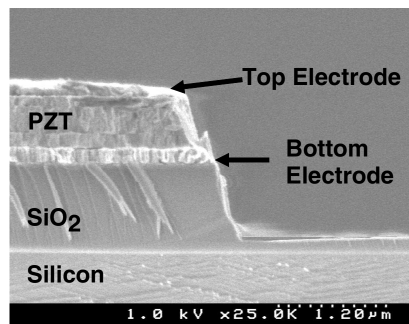

Figure 3.6 PZT stack after ion milling with both 40º and 85º ion milling angles.

This ion milling can be continued through the oxide layer into the silicon substrate or it can be stopped after the Pt etching and a standard oxide RIE can be used to finish etching to the silicon substrate if a topside release process will be used. The advantage of using the RIE process is better wall definition and the minimization of Pt redeposition from exposure of the bottom Pt to the ion milling process. If a backside release process is used, the oxide is left on the substrate until after the Silicon DRIE process is complete. This process is represented in steps 4a, 5a, and 5b in Figure 3.1.

The dry etch described in section 3.2 for the bottom electrode etch was also used on early devices for forming the PZT etch to form the resonator dimensions. This process, although successful in fabricating devices, was dropped in favor of the ion milling process once the multi-angle process was developed because the entire stack could be etched in one step and in one tool. This process is represented in step 4b in Figure 3.1.

3.5 Resonator Release

The final step is the release of the resonator structure to form the suspended clamped-clamped bridge structure used for the resonators fabricated for this study. Again two different techniques were demonstrated. The first process demonstrated was to etch an opening all the way through the 500 μm of silicon from the backside of the wafer. The pattern for the opening was done using front-back photolithography with a dark field mask and 6+ μm of AZ9245 positive tone photoresist. The wafer was then placed device layer down in a Plasma Therm 770 silicon deep reactive ion etch (DRIE) process. This

system uses the Bosch process, which is a multi-step (C_4F_8/Ar deposition and SF_6/Ar etch) process with very anisotropic, near 90º, sidewalls and an etch rate of approximately 3 μm/minute. The Si was removed down to the SiO_2 layer under the PZT that acts as an etch stop for the process and prevents the full release of the structure while in the DRIE system. The wafer is then placed device layer up in a oxide RIE system and the oxide in the trenches between the resonator and the substrate is removed, leaving a suspended SiO_2/Pt/PZT/Pt structure. Figure 3.7 shows the backside of a triple-beam resonator, through the 500 μm deep opening in the silicon. Figure 3.8 shows the top side of the same triple beam resonator as Figure 3.7 along with the adjacent single beam resonator [24].

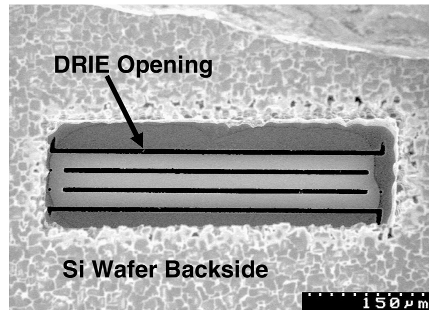

Figure 3.7 Backside of a triple-beam resonator viewed through the DRIE opening on the backside of the wafer.

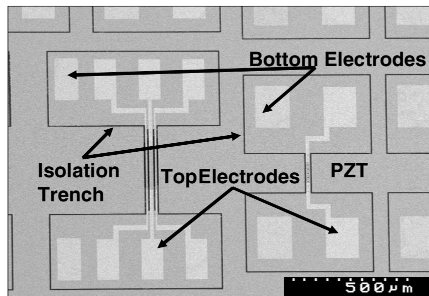

Figure 3.8 Topside image of fabricated single and triple-beam PZT resonators released from the backside.

The drawback to this technique is that the front-to-back alignment and the alignment of the DRIE opening to the resonator anchor points is very difficult, as seen in Figure 3.7 where the resonator is not centered within the opening. Another problem is that the etch used does have a slight taper and, even at only a 1° positive taper over the 500 μm etch, it will create an opening that is 16 μm larger than the original etch mask opening. Therefore, it is difficult to get the resonator anchors to fall exactly on the etch opening without any undercutting, as seen on the right hand side of Figure 3.7.

A second technique was developed to release the resonators from the topside through an isotropic Si etch process. This process was also done in the Plasma Therm 770 system except that only an isotropic SF_6/Ar etch was used. The process has also been demonstrated using a XeF_2 isotropic etch in place of the SF_6/Ar etch. One modification to a previous step was to open up the narrow trenches that had previously defined the beam geometry ion mill steps 4 and 5 in Figure 3.1 in order to be able to visually determine if the devices were released. As the Si was etched isotropically, the resonator was undercut and eventually released. The one problem with devices using this technique was that not only was the resonator undercut, but the anchor points were as well. This was eventually solved by the addition of an extra photoresist step after ion milling the large rectangular opening. This effectively moved the starting point of the isotropic etch so that as the beam was undercut, the resist, and not the anchor, was undercut. A resonator fabricated with this technique is shown in Figure 3.9. This device had a thin oxide layer under the extra photolithography step as well and the remaining oxide, after resist removal, can be seen showing how the oxide/resist layer was undercut and not the anchor points. This technique still requires a well-timed etch to minimize any undercutting.

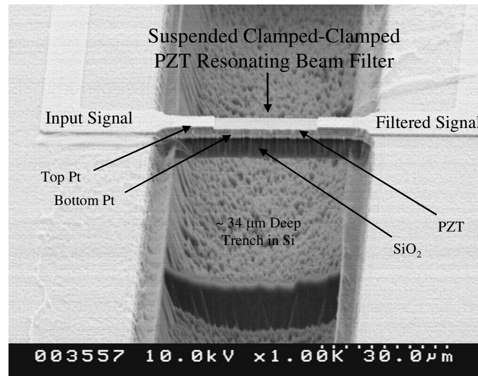

Figure 3.9 Topside image of fabricated single-beam PZT resonator released from the topside.

3.6 Final Overall Process

The final process flow that has been optimized for the resonator fabrication uses Pt lift-off for the top electrodes, wet etch for the bottom electrodes, ion milling for the resonator beam definition, and isotropic silicon topside release. This follows steps 1b, 2b, 3, 4a, 5a, and 6a from Figure 3.1. The initial resonators fabricated under this research were the first fabricated and demonstrated devices using the sol-gel PZT films developed at ARL.

Chapter 4. Experimental Apparatus

The following experimental test set-ups were used in the course of this work and the data from these systems are discussed in subsequent chapters.

4.1 Wafer Bow Stress Gauge

Figures 4.1 and 4.2 show the Tencor FLX-2908 system used to measure residual stresses as a function of temperature for the material property testing and the stress studies discussed in Chapter 5 and 7.

Figure 4.1 Tencor FLX-2908 system used for wafer bow and stress measurements.

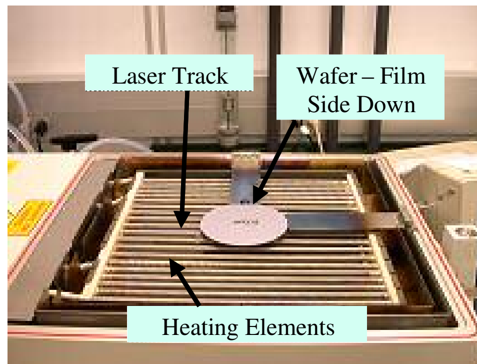

Figure 4.2 FLX-2908 internal configuration showing wafer placement and heating elements.

The wafer is positioned, film side down, on quartz pins in the middle of the system via mechanical locator plates. The laser is scanned in a single pass across the center of the wafer in a direction parallel to the heating elements shown in Figure 4.1. This is a two laser system (670nm and 750nm) and the system automatically chooses the one returning the highest signal to solve problems caused by transparent thin films such as silicon nitride. The heating elements are resistive heaters capable of temperatures up to 900 ºC and a nitrogen purge during the testing is an option that can be turned on via a manual valve.

The system measures the initial radius of curvature of the wafer by first scanning the substrate prior to deposition of the thin film and then again after the thin film is deposited. The residual stress in the deposited film causes a change in the radius of curvature of the substrate. The radius of curvature is defined as

$$R = \frac{\left(R_1 R_2\right)}{\left(R_1 - R_2\right)}. \quad (4.1)$$

Once the radius of curvature is known, the thin film residual stress can be calculated from Stoney's equation

$$\sigma = \frac{Eh^2}{\left(1-\upsilon\right)6Rt}. \quad (4.2)$$

In this equation, σ is the average film stress, E is the Young's modulus of the substrate, ν is Poisson's ration, h is the substrate thickness, R is the substrate radius of curvature, and t is the film thickness.

4.2 Network Analyzer and Vacuum Probe Station

The test set-up for all of the electrical measurements for this work is shown in Figure 4.3.

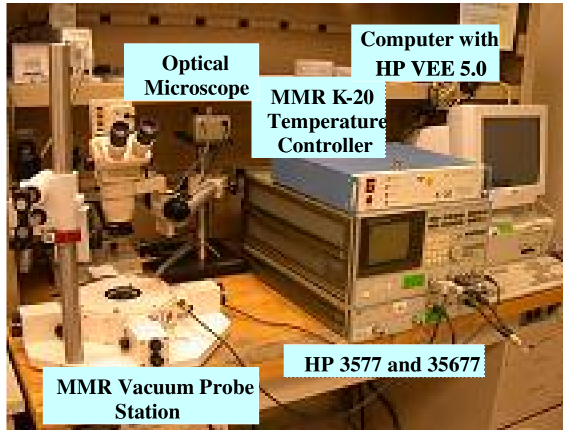

Figure 4.3 Electrical and vacuum test set-up used for all electrical response measurements.

The MMR vacuum probe station used for this research has four probes with x, y, and z motion control. Three of the probes were used to make contact to the drive (Port 1), sense (Port 2), and ground resonator electrodes (see Figure 2.7), and the fourth probe was not used. The probe station has a manual vacuum controller that allows for operation from approximately 10 mTorr to atmospheric pressures. The system also comes with a MMR model K-20 temperature controller and a stage that couples a Joule-Thomson refrigerator and a resistive heater to allow temperature testing from 80 K to 400 K. Only the heater was used for this work, even at vacuum levels of 10mTorr, there was enough moisture within the system to get ice formation at freezing temperatures which can cause mass loading and spurious results in measuring the true resonant frequency of the devices.

A HP 3577A network analyzer was used to measure the electrical response of the resonators. The network analyzer was used to set the frequency test range (5 Hz to 200 MHz), the measurement parameters (A/R or S-parameters and phase), frequency sweep direction (up or down), drive amplitude (-40 db to +15dB), receiver impedance (50 ohm or 1 Mohm), and measurement averaging. A schematic of the electrical test set-up is shown in Figure 4.4.

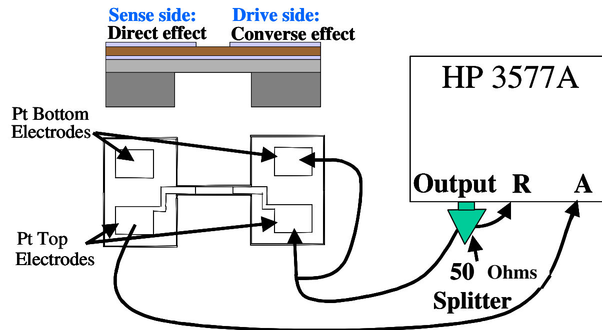

Figure 4.4 Schematic of electrical test set-up.

The output of the network analyzer is split with one coaxial cable routed to the reference port (R) on the network analyzer, and the second one is routed to the drive probe on the MMR vacuum probe station that contacts the drive electrode on a given resonator. The ground of the coaxial cable is routed to a second probe on the MMR vacuum probe station and this probe is contacted to a ground pad on the resonator. A third probe was contacted to the sense side top electrode and this probe was connected via coaxial cable back to the input (A) on the network analyzer. The response of the resonator is then obtained by measuring magnitude and phase of the A/R signal inputs. The measured A/R magnitude and phase data is collected by a program written in HP VEE 5.0 software

which remotely controls and collects data from the HP3577. The data is saved in a text format so it can be read into an excel spreadsheet for plotting and data analysis.

4.3 Electrode Area and Impedance Matching

The amount of capacitance between the top and bottom electrode can affect the noise floor of the measurement. Figure 4.5 shows the magnitude and phase response of an 80 µm resonator with a full 100 µm x 200 µm top electrode. Figure 4.6 shows a second 80 µm resonator from the same wafer with a portion of the top electrode removed.

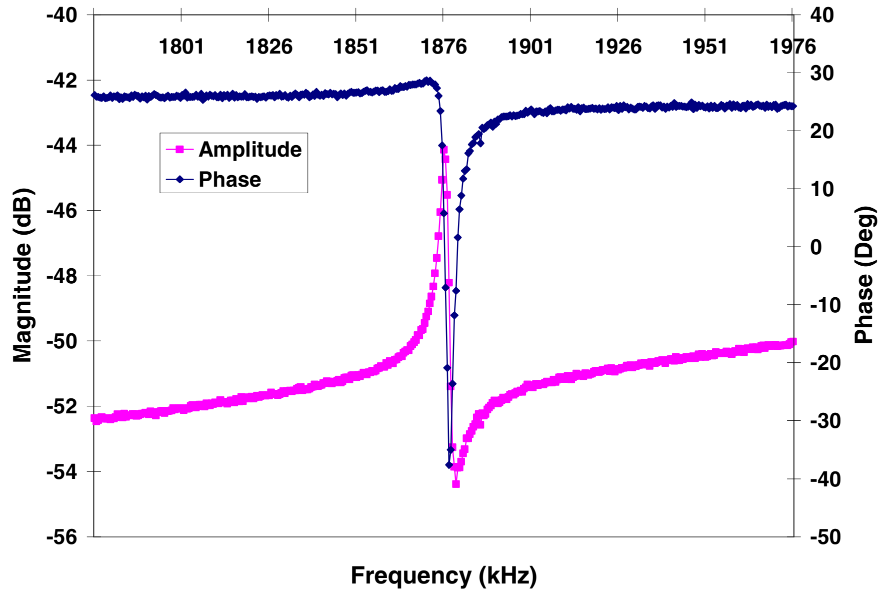

Figure 4.5 Magnitude and phase response for an 80 µm PZT resonator with full 100 x 200 µm electrodes.

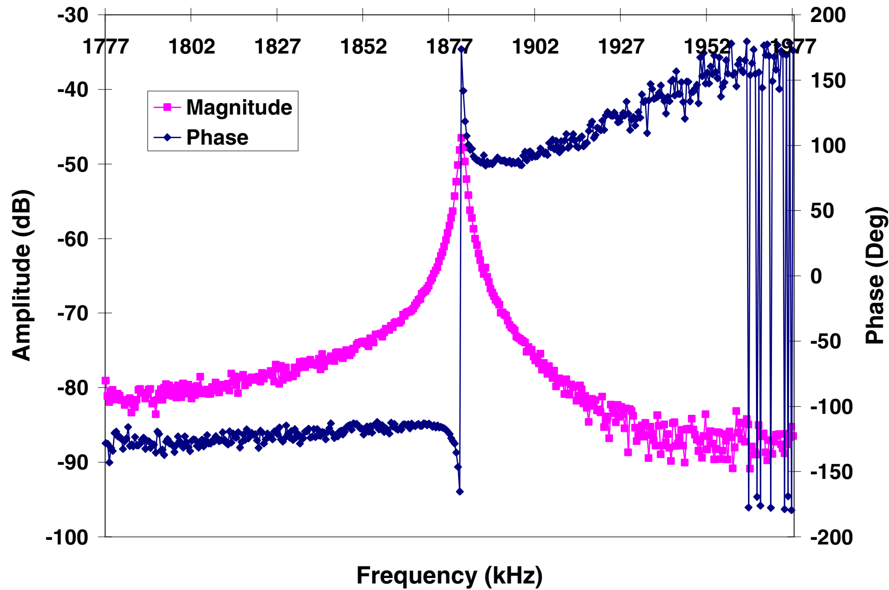

Figure 4.6 Magnitude and phase response for an 80 µm PZT Resonator with reduced electrode area.

From the difference between Figures 4.5 and 4.6, by reducing the top electrode area the amount of capacitive feed-through can be significantly reduced and the noise floor drops down to –80 dB from the original –52 dB. The same overall loss of approximately 44 dB was maintained so the signal peak went from 12 dB to 36 dB. The removal of the excess capacitance also eliminated the anti-resonant peak seen in Figure 4.5 and resulted in a 180º phase shift versus a 0 degree phase shift. The electrode size and capacitance is more of an issue at higher frequencies. Figures 4.7 and 4.8 show the change in a 400 µm resonator when going from a full 100 µm x 200 µm top electrode to a 100 µm x 50 µm top electrode.

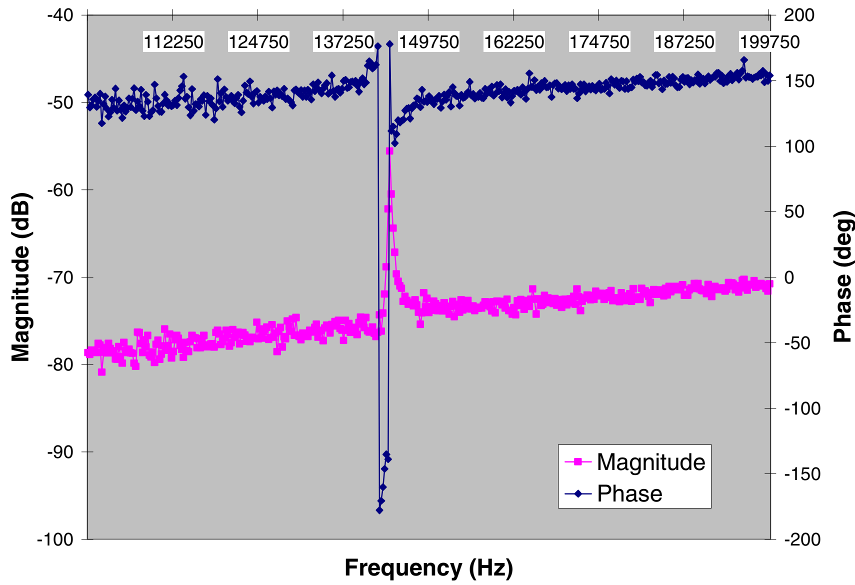

Figure 4.7 Magnitude and phase response for a 400 μm PZT resonator with 100 x 200 μm top electrodes.

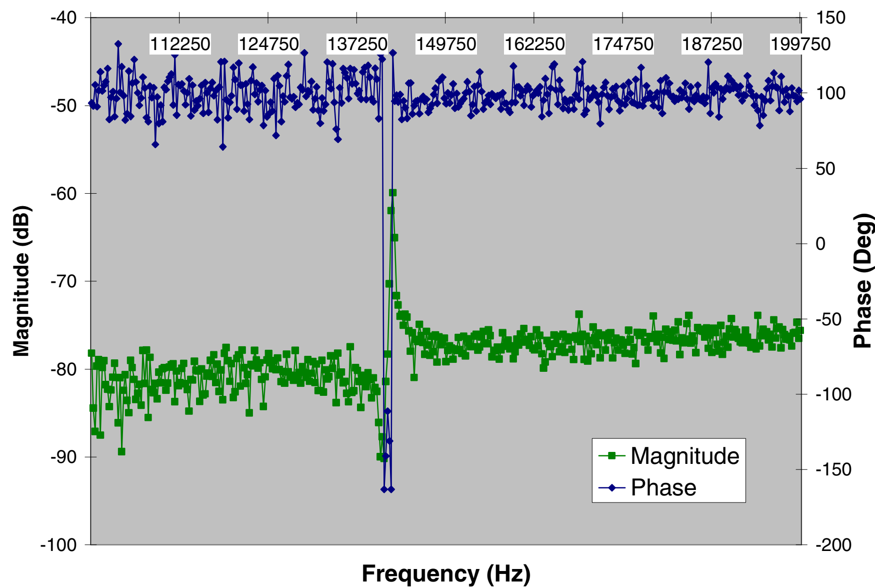

Figure 4.8 Magnitude and phase response of a 400 μm PZT resonator with 100 x 50 μm top electrodes.

From Figures 4.7 and 4.8, the 400 μm long resonator only experienced a drop of approximately 5 dB in the noise floor versus the approximately 30 dB seen for the 80-μm

resonator. The reduction of the electrode size did produce an anti-resonant peak below the resonant peak for the 400 μm resonator. This varies from the 80 μm resonator that showed an anti-resonant peak above the resonant peak for the large electrode area and then no anti-resonance peak with the reduced electrode area.

The PZT resonators are high impedance devices resulting in large reflected signals and large loss values. The use of a unity gain op-amp on the output of the probe station was tried to improve the impedance matching and improve the signal response. Figure 4.9 shows the same 80 μm clamped-clamped beam from Figure 4.6 with the unity gain op-amp installed in the circuit.

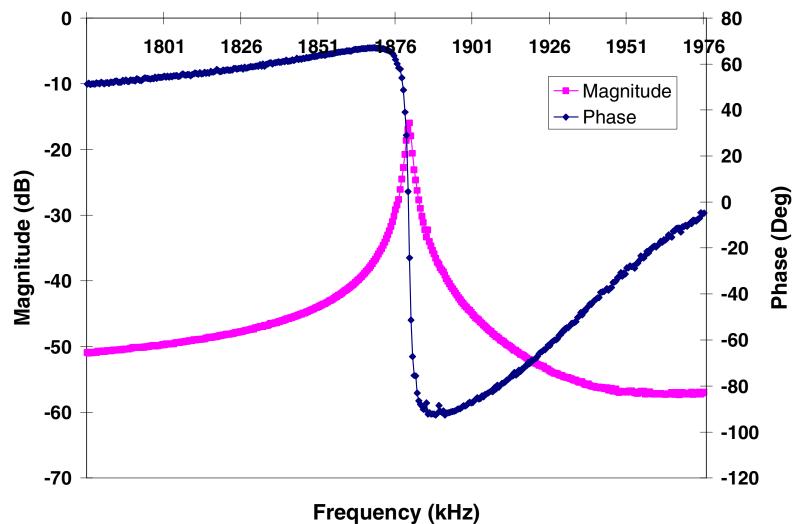

Figure 4.9 Magnitude and phase response with use of a unity gain op-amp.

From Figure 4.9, the op-amp drastically improved the impedance matching and reduced the loss of the resonator from –44 dB to –15 dB. It also introduced an additional 90º phase shift resulting in an approximately 0º phase shift at resonance. A charge amplifier

was also tried with similar results as the unity gain op-amp but it began to break down at higher frequencies and was not used for any of the reported data. A unity gain op-amp was used for some of the reported data for this research and can be identified by low loss (<20 dB) and ~0 phase shift values. A similar effect can be achieved by using a 1 MΩ impedance on the input to the network analyzer versus the typical 50 ohms. Figure 4.10 shows the output from the same 400 μm shown in Figure 4.8 but with the input impedance change to 1 MΩ.

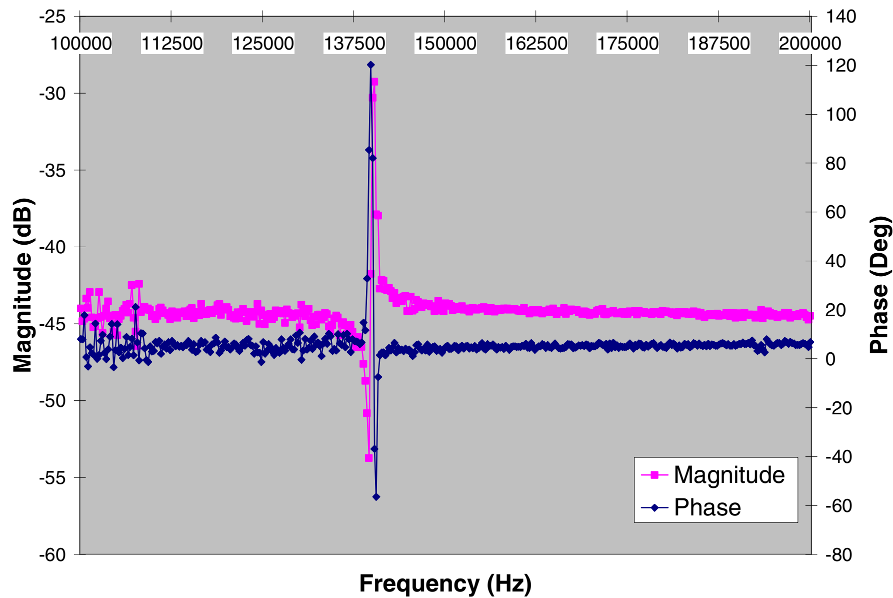

Figure 4.10 Magnitude and phase response of a 400 μm PZT resonator with 100 x 50 μm top electrodes and 1 MΩ input impedance.

From Figure 4.10, the loss has been reduced from 60 dB to 30 dB and the phase at resonance has changed from 180 degrees to 0 degrees. It is important to note that for a final application impedance matching circuitry could be built to greatly reduce the loss seen in the resonator data published here. Also, since the LDV data only looked at the

mechanical and not the electrical response of the resonators, full 100 x 200 μm top electrodes were used for the LDV testing.

4.4 Laser Doppler Vibrometer

The test set-up for all of the Laser Doppler Vibrometer (LDV) mode shape data is shown in Figure 4.11.

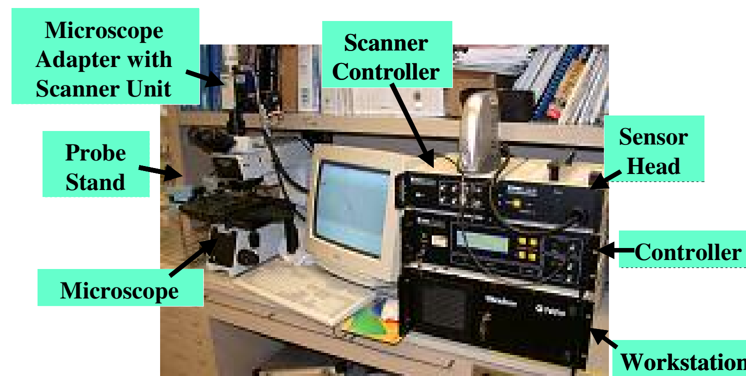

Figure 4.11 Polytech LDV test set-up used for measuring resonator frequency and mode shapes.

The system is a Polytech Microscope Scanning Vibrometer (MSV 300). The workstation is the computer that runs the software and records the data; the controller decodes the interferometer signal; the sensor head contains the interferometer which is linked via fiber optic to the scanner unit; the scanner controller is the interface between the system components; the scanner unit uses piezoelectric elements to scan the laser beam; the probe stand supports two probes for contacting the resonator electrodes; and the microscope is used to focus the laser spot onto the resonator. The laser spot size can be reduced from 50 μm at 1x to 5 μm with the 10x objective and 2.5 μm with the 20x

objective used for this research. Figure 4.12 shows the operational system overview for the LDV system.

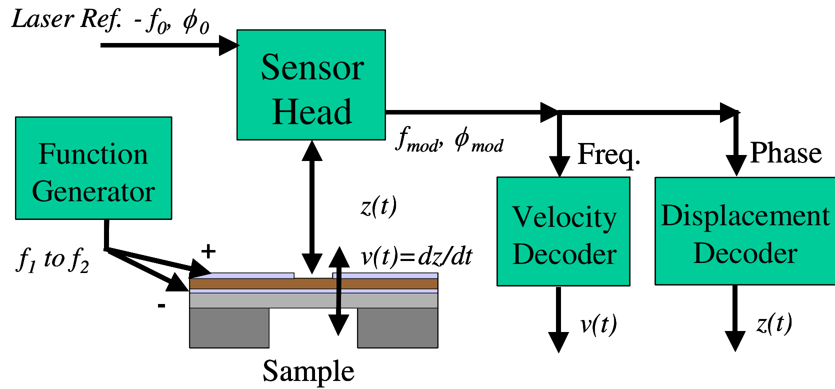

Figure 4.12 Schematic of LDV measurement technique.

The Polytech LDV actuates the resonator by sending out an RF electrical signal from the an internal function generator (range from 0 to 500 MHz). One leg is connected by a coaxial cable to a probe on the probe stand which is contacted to the drive-side top electrode. The minimum signal that can be put out from the generator is 10 mV. A ground is connected to the second probe that is contacted to the bottom Pt or ground pad on the resonator. The out-of-plane velocity is interrogated by a helium neon laser by using an interferometer that compares the reflected light to that of a reference beam. The frequency difference is proportional to the instantaneous velocity and the phase difference to the instantaneous displacement. This point is then scanned across the sample using the piezoelectric elements in the scan head to deflect the laser beam from point to point. From the velocity and phase data at each point, the software can construct the frequency response spectrum, the beam displacements at each point, and the overall mode shape of vibration.

The function generator for this system is limited to 1 MHz and the scanning mode is limited to 500 kHz, which limited its use to the larger lower frequency devices tested within this research. Single point measurements can be made up to 20 MHz.

4.5 Optical Profilometer

The beam curvatures were measured using the Veeco Optical Profilometer pictured in Figure 4.13.

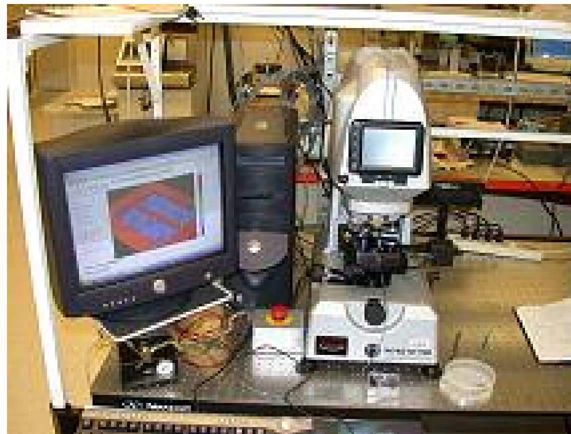

Figure 4.13 Veeco optical profilometer used for static displacement measurements.

The optical profilometer is used in vertical scanning interferometry (VSI) mode. In the VSI mode, white light reflected from the sample is combined with the light reflected from a reference mirror to produce interference fringes, and the system measures the degree of fringe modulation [46]. The sample is then moved in the z direction through the optical focus. Fringes are seen in only a very small depth of field and by knowing the relative z position of the sample; the system can determine the vertical position of each point on the sample. The VSI mode has a vertical range up to 2 mm and a resolution of 3

nm. It cannot accurately measure the relative height of transparent materials on top of opaque materials such as thin film oxides and PZT on top of Pt. This is the result of a phase change that occurs as the light passes through the thin film and reflects off of the opaque substrate layer. For the case of PZT over Pt, the PZT shows up as a negative height. For the research presented here, the PZT thickness is a uniform thickness over the Pt bottom electrode. The relative height between two points consisting of PZT over Pt is valid, while the relative height between a Pt surface (top or bottom electrode) and a PZT over Pt surface will be inaccurate. The beam deflection and curvature data measured for this work was taken as the difference between points in the center of the beam between the top electrodes (PZT over Pt) to a point on the substrate without top Pt (PZT over Pt) so that the measured beam deflections are accurate even though the beam center is offset compared to the top Pt surface by this phase-shifted bias.

4.6 Optical Microscope

The static, stress-induced, cantilever tip vertical deflections approached 400 µm and near vertical (90º) slopes for the 400 µm cantilevers tested for this research. Because of the severe curvatures and amount of deflection, optical profilometry could not be used. For the static cantilever tip deflection measurements, an optical defocusing technique was employed using an Olympus microscope and a 20x lens. The microscopes focusing knob vernier scale was calibrated by first focusing on the top and then the bottom of a known depth flat feature on each wafer, as measured by a stylus profilometer, and monitoring the number of increments turned on the focus knob. Table 4.1 shows the calibration data for the Olympus microscope.

Table 4.1 Olympus microscope calibration.

Wafer #	Profilometer Measured Step (microns)	Optical Vernier Measured Increments (clicks)	microns/click
W1	29.89	27	1.11
W2	32.75	31	1.06
W3	33.76	33	1.02
W4	34.75	34	1.02
W5	15.11	15	1.01
W7	12.84	12	1.07
W9	31.39	29	1.08
		Avg	1.05
		Std Dev	0.03

The calibration resulted in a 1.05 increment/micron ratio with a standard deviation of 0.03 microns over 7 wafers. A much larger error was seen in practice, +/- 2 to 3 microns, because of the uncertainty of when only the tip was in focus vs. the planar structures used for the calibration.

Chapter 5. Material Characterization

5.1 Approach

A problem in designing MEMS devices and developing accurate models is the lack of thin film material properties such as Young's modulus, coefficient of thermal expansion (CTE), and residual stress. Most designers are relegated to using values for bulk films or values from thin films deposited by processing techniques and tools different than what they will eventually be using to fabricate their own prototypes and eventual commercial devices. This constraint is especially true for thin film sol-gel PZT, which has received little attention compared to more traditional films used in MEMS processing such as silicon or polysilicon. This is a serious problem in the MEMS community leading to much trial and error in product development and increased research and technology transition cycle times.

The method of using wafer bow for obtaining mechanical properties has been used by others for films such as BN, SiO_2, Au, Al, and Cu [47 - 50]. The method uses wafer curvature to measure the thermal stresses of thin films of the same material deposited on two different substrates. If the substrates are both isotropic in the plane of the wafer, the biaxial modulus and coefficient of thermal expansion can be determined. In this technique, the Poisson's ratio needs to be assumed based on bulk values to determine the Young's modulus. If the second wafer is anisotropic, the Poisson's ratio and the Young's modulus can be determined.

The stress in a thin film deposited on a isotropic substrate can be expressed by Stony's equation

$$\sigma_{f0} = \frac{E_s t_s^2}{6(1-\nu_s)t_f}\left(\frac{1}{R} - \frac{1}{R_0}\right) \tag{5.1}$$

where *s* designates substrate, *f* designates thin-film, *E* is Young's modulus, *t* is thickness, *R* is radius of curvature, and *v* is the Poisson's ratio. The measured stress is a combination of intrinsic stress from the growth of the material and an extrinsic stress arising from the CTE mismatch between the film and the substrate. The thermal component can be given by

$$\sigma_f = \frac{E_f}{(1-\nu_f)}\int_{T_1}^{T_2}(\alpha_s - \alpha_f)dT\,. \tag{5.2}$$

The slope of the measured stress-temperature curve is

$$\frac{d\sigma_f}{dT} = \frac{E_f}{1-\nu_f}(\alpha_s - \alpha_f)\,. \tag{5.3}$$

If two different isotropic substrates are used, the following two equations and three unknowns result:

$$\frac{d\sigma_1}{dT} = \frac{E_f}{1-\nu_f}(\alpha_{s1} - \alpha_f) \text{ and} \tag{5.4}$$

$$\frac{d\sigma_2}{dT} = \frac{E_f}{1-\nu_f}(\alpha_{s2} - \alpha_f)\,. \tag{5.5}$$

The subscripts 1 and 2 designate the two different substrates. By solving for the biaxial modulus instead of the Young's modulus, one variable can be eliminated and a solution for the biaxial modulus and the CTE for the film can be obtained. Rearranging and substituting leads to

$$\frac{E_f}{1-\nu_f} = \frac{d\sigma_1}{dT}\frac{1}{\alpha_{s1} - \alpha_f} = \frac{d\sigma_2}{dT}\frac{1}{\alpha_{s2} - \alpha_f}\,, \tag{5.6}$$

and then solving for α_f

$$\alpha_f = \left(\frac{d\sigma_2}{dT}\alpha_{s1} - \frac{d\sigma_1}{dT}\alpha_{s2}\right)\left(\frac{1}{d\sigma_2/dT - d\sigma_1/dT}\right) = \frac{K_2\alpha_{s1} - K_1\alpha_{s2}}{K_2 - K_1}\,, \tag{5.7}$$

where $K = \frac{d\sigma}{dT}$ which is measured experimentally, and

$$\frac{E_f}{1-\nu_f} = \frac{K_2 - K_1}{\alpha_{s2} - \alpha_{s1}}\,. \tag{5.8}$$

Therefore, by measuring the slope of a stress versus temperature plot for a film on two different substrates, the slope of the stress/temperature curve can be used to determine the CTE and biaxial modulus of the film if the properties for the substrates are known.

For this research, two different isotropic substrates were used to measure the biaxial Young's modulus and the CTE for the PECVD SiO_2, PECVD Si_3N_4 and the sputtered Pt thin films used to fabricate the PZT MEMS resonators. A Poisson's ratio for each material was assumed to be equivalent to reported values for bulk and or thin films in order to obtain the value of the Young's modulus. The first substrate was a 100 mm <100> silicon wafer that is isotropic in the plane of the wafer and has a biaxial Young's modulus of 180.5 GPa and a CTE of 2.841 x 10^{-6}/ºC. The second was a single crystal quartz wafer with a biaxial Young's modulus of 119.4 GPa and a CTE of 7.48 x 10^{-6}/ºC.

The actual SiO_2 and Pt thin films used for the resonators are annealed at temperatures up to 700°C during processing to modify their residual stress levels. For this work, the quartz wafers could not be heated above 573ºC because the α-quartz to β-quartz transition at this temperature would fracture the wafer during the rapid thermal anneal (RTA) anneal process. The temperature cycle chosen for this testing was a slow ramp up to 400ºC under nitrogen to bring the thin-film up beyond the 250ºC deposition temperature for the PECVD SiO_2 and Si_3N_4 films as well as the 100ºC sputter deposition temperature for the Pt thin-film deposition to perform a partial anneal on the films. The wafers were then cooled to room temperature and then ramped back up to 400ºC, and the data for this second ramp-up to temperature was used for calculating the slopes of the stress versus temperature curves. All testing was performed on the Tencor FLX Wafer Bow Stress system described in Chapter 4 with a N_2 flow turned on to help obtain uniform temperature across the wafers.

5.2 SiO_2 Material Properties

Figure 5.1 shows a plot for the SiO_2 thin films on the Silicon and Quartz substrates.

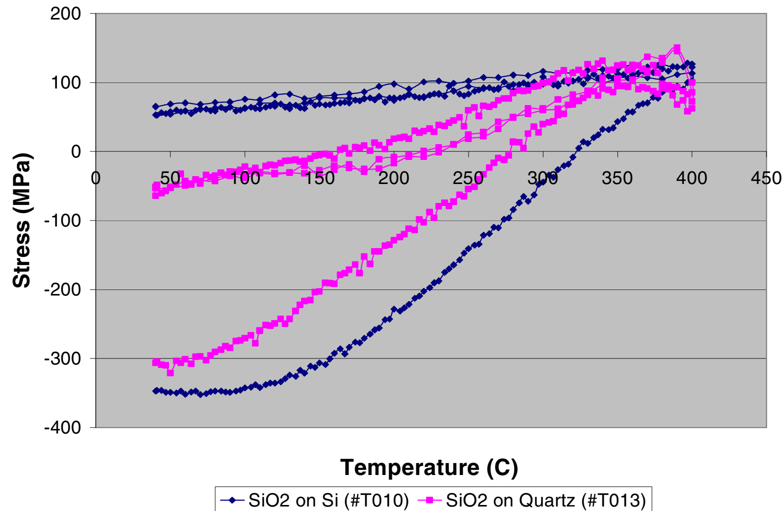

Figure 5.1 Plot of dσ/dT curves for SiO_2 on silicon and quartz.

From Figure 5.1, the change in the intrinsic stress of the SiO_2 cause by the 400 ˚C anneal can be seen from the large change in slope from the first temperature ramp to the second temperature ramp. The difference from the second to the third temperature ramp is small, meaning that the change in wafer bow is coming from extrinsic stress arising from the CTE mismatch between the film and the substrate, and the slopes can be used for calculating CTE and Biaxial modulus. The measurements were repeated on a second wafer and the calculated slope for the PECVD SiO_2 films on the two wafers from two different substrates are reported in Table 5.1. Using the average values for the slopes in Table 5.1 and the previously reported values for the silicon and quartz CTEs, equations (5.7) and (5.8) were used to calculated the Young’s modulus and CTE for the PECVD oxide thin film. The calculated biaxial Young’s modulus was 816 GPa and the CTE was

0.7 x 10^{-6}/ºC. If the Poisson's ratio is assumed to be 0.17 [51], the resultant Young's modulus is 68 GPa. These values are reasonable given reported values of for SiO_2 of E=73GPa and CTE=0.55 x 10^{-6}/ºC [51].

Table 5.1 dσ/dT slopes for oxide on silicon and quartz substrates.

Measurement	Slope on Si (x 10^5)	Slope on Quartz (x 10^5)
1	1.86	6.04
2	1.62	5.00
Average	1.74	5.52

5.3 Pt Material Properties

Figure 5.2 shows the plot for the Pt thin films on the silicon and quartz substrates, and the calculated slopes are reported in table 5.2 for each substrate.

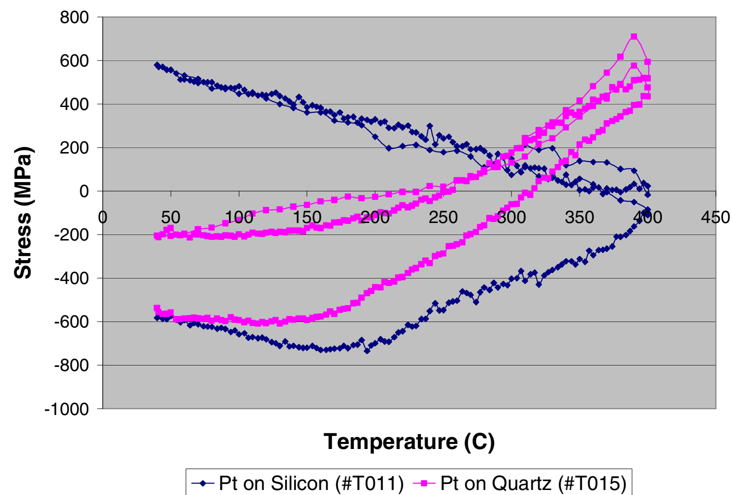

Figure 5.2 Plot of dσ/dT curves for Pt on silicon and quartz.

For the case of Pt on quartz, only the linear portion of the curve between room temperature and 150 °C was used for the calculations. The second and third temperature

ramps are repeatable with the same nonlinear curvature at the higher temperatures. This is assumed to be caused by the large deflections caused by the large difference in CTE and Young's modulus between the Pt and the Quartz substrate.

Table 5.2 $d\sigma/dT$ slopes for platinum on silicon and quartz substrates.

Measurement	Slope on Si (x 10^6)	Slope on Quartz (x 10^5)
1	-1.72	1.68
2	-1.77	1.29
Average Slope	-1.75	1.49

Using the average values for the slopes from Table 5.2 and the previously reported values for the silicon and quartz CTEs, equations (5.7) and (5.8) were used to calculate the Young's modulus and CTE for the sputtered Pt thin films. The calculated biaxial Young's modulus was 408 GPa and the CTE was 7.1 x 10^{-6}/ºC. If the Poisson's ratio is assumed to be 0.39 [52, 53] the resultant Young's modulus is 250 GPa. The value for the CTE is close reported CTE value of 9.1 x 10^{-6}/ºC but the Young's modulus for these sputtered films is much higher than the value used in the initial modeling and typically reported in literature of 170 GPa [52, 53].

5.4 Si_3N_4 Material Properties

Figure 5.3 shows the plot, including trend lines used for calculating slopes, for the Si_3N_4 thin films on the silicon and quartz substrates.

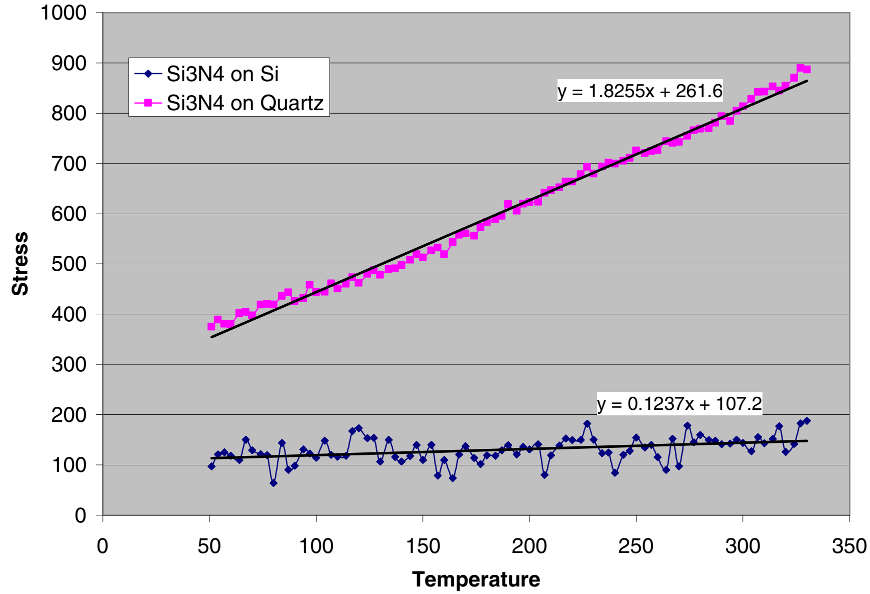

Figure 5.3 Plot of dσ/dT curves for Si_3N_4 on silicon and quartz.

Using the slopes from Figure 5.3 an the previously reported values for the silicon and quartz CTEs, equations (5.7) and (5.8) were used to calculated the Young's modulus and CTE for the PECVD Si_3N_4 thin films. The calculated biaxial Young's modulus was 391 GPa and the CTE was 2.81 x 10^{-6}/ºC. If the Poisson's ratio is assumed to be 0.25 [51] the resultant Young's modulus is 293 GPa. The values for the Young's modulus and CTE are reasonable and close to reported values of 323 GPa for the Young's modulus and 2.8 x 10^{-6}/ºC for the CTE [51].

For future work, if an anisotropic substrate is substituted for one of the isotropic substrates, the Poisson's ratio can also be determined because the anisotropy adds a third equation for the three unknowns. For the case of using an anisotropic substrate the following equations would be used:

$$\sigma_{fx} = \frac{E_{sx} t_s^2}{6(1-\nu_{sx}\nu_{sy})t_f}\left(\frac{1}{R_x} + \nu_{sy}\frac{1}{R_y}\right) \text{and} \tag{5.9}$$

$$\sigma_{fy} = \frac{E_{sy} t_s^2}{6(1-\nu_{sx}\nu_{sy})t_f}\left(\frac{1}{R_y} + \nu_{sx}\frac{1}{R_x}\right) \tag{5.10}$$

where the subscripts x and y designate two directions in the plane of the wafer. Equations (64) and (65) can be combined to give the stress vs. temperature via

$$k_0 = \frac{d\sigma_{f0}}{dT} = \frac{E_f}{1-\nu_f^2}(\alpha_{s0} - \alpha f) \tag{5.11}$$

$$k_x = \frac{d\sigma_{fx}}{dT} = \frac{E_f}{1-\nu_f^2}\left[(\alpha_{sx} - \alpha_f) + \upsilon_f(\alpha_{sy} - \alpha_f)\right] \tag{5.12}$$

$$k_y = \frac{d\sigma_{fy}}{dT} = \frac{E_f}{1-\nu_f^2}\left[(\alpha_{sy} - \alpha_f) + \upsilon_f(\alpha_{sx} - \alpha_f)\right] \tag{5.13}$$

where α is the coefficient of thermal expansion and T is temperature. Equations (5.11) through (5.13) can then be solved for

$$\alpha_f = \frac{(k_s + k_y)\alpha_{s0} - k_0(\alpha_{sx} - \alpha_{sy})}{k_x + k_y - 2k_0} \tag{5.14}$$

$$E_f = \frac{(2k_0 - k_x - k_y)(k_x - k_y)}{k_0(\alpha_{sx} - \alpha_{sy}) + k_s(\alpha_{s0} - \alpha_{sx}) + k_y(\alpha_{sy} - \alpha_{s0})} \tag{5.15}$$

$$\nu_f = \frac{k_0(\alpha_{sx} - \alpha_{sy}) + k_x(\alpha_{sy} - \alpha_{s0}) + k_y(\alpha_{s0} - \alpha_{sx})}{k_0(\alpha_{sx} - \alpha_{sy}) + k_s(\alpha_{s0} - \alpha_{sx}) + k_y(\alpha_{sy} - \alpha_{s0})} \tag{5.16}$$

leaving three equations and three unknowns that can be solved for the Young's modulus, Poisson's ratio, and the CTE for the thin film.

5.5 PZT Young's Modulus

PZT was not directly measured by the wafer bow technique since sol-gel PZT needs to be deposited on top of a Si/SiO_2/Pt stack in order to get the correct grain growth and crystallization. To obtain the Young's modulus and CTE values for the PZT thin films, a combination of cantilever resonance testing, clamped-clamped resonator testing, and FEM using the values previously obtain for SiO_2 and Pt was used.

Cantilever beam resonance has been reported by several groups for the determination of Young's modulus for films used in MEMS devices [54-57]. Once the value for the Young's modulus was determined for the SiO_2 and Pt films by the wafer bow methods described in the previous section, cantilevers beams were fabricated on the same wafers as the generation II PZT MEMS resonators to be discussed in Chapters 6 and 8. A matrix of eight wafers, given in Table 5.3, was fabricated to support this work and that of Currano [28] for validating finite element models. Wafer W9, which was fabricated for the initial generation II resonator testing, was also included for the following work.

Table 5.3 Matrix of thin film thickness (microns).

Wafer #	Beam Width	Oxide Thickness	Bottom Pt Thickness	PZT Thickness	Top Pt Thickness
W1	20.0	1.06	0.135	0.530	0.200
W2	19.5	1.08	0.135	1.04	0.190
W3	20.0	2.13	0.135	0.547	0.200
W4	19.5	2.12	0.135	1.06	0.195
W5	13.0	1.03	0.850	1.09	0.100
W6	20.0	1.03	0.850	0.516	0.105
W7	16.9	1.97	0.850	0.552	0.100
W8	20.0	1.99	0.850	1.01	0.105
W9	20.0	2.03	0.190	0.440	0.165

The first resonant frequency of a cantilever beam is [54]

$$\omega_0 = \frac{1.875^2}{2\pi}\sqrt{\frac{EI}{mL^4}} = \frac{3.52}{2\pi L^2}\sqrt{\frac{EI}{m}}, \tag{5.17}$$

where E, I, and m are the equivalent Young's modulus, Moment of Inertia, and mass. For the PZT cantilevers, the composite Young's modulus and the frequency are the unknowns. By testing the structures, the resonant frequencies can be determined leaving the Young's modulus of the PZT as the only unknown since the material properties of the Pt and SiO_2 films have been characterized. The PZT Young's modulus can then be calculated by using equation (5.17).

Cantilevers were chosen for this testing since their frequency is minimally affected by the residual stresses or the deformed shapes caused by residual stresses within the beams. Measurements were taken at atmospheric pressure on the Polytech LDV system

described in Chapter 4. Air damping can affect the first resonance frequency of a resonator, and for cantilevers this has been shown to be

$$f_r = f_0\sqrt{1-\frac{1}{4Q^2}} \text{ [54].} \tag{5.18}$$

From (5.18), it can be seen that if Q is relatively large, there is little effect on the resonant frequency. From the LDV data, it can be seen that the Q is on the same order as that for the measured loaded Qs for the clamped-clamped beams which are around 500 in air, so for these results, air damping effects were neglected.

Cantilevers with lengths of 100, 200, 300, and 400 microns were fabricated and tested. ANSYS 8.0 finite element models were then made of the same 100, 200, 300, and 400 μm cantilevers and the values for Young's modulus for the SiO_2 and Pt films obtained from the wafer bow testing were put into the FEM. The value of the Young's modulus of the PZT was then varied within the FEM until the resonant frequency matched the measured resonant frequency for that beam. For these cantilever tests, wafers W1, W3, W7, and W9 from Table 5.3 were used.

Because of residual stress, not all cantilevers survived fabrication and the 400 μm devices were not included in this analysis. Figure 5.4 shows a typical output from the ANSYS model.

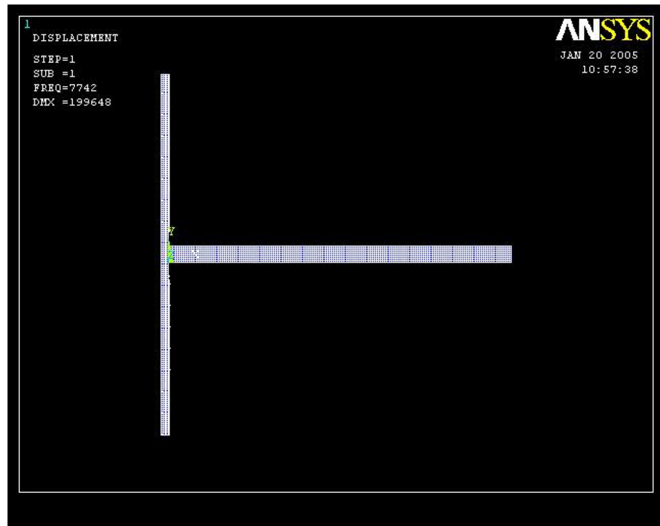

Figure 5.4 ANSYS output for cantilever resonance modeling.

The resonators fabricated for these tests were released from the topside by the isotropic silicon etch process prior to the additional photoresist step described in Section 3.4, and all of the anchor points were undercut by varying amounts. The amount of undercut for each wafer was measured by physically breaking the overhanging area with a probe and then measuring the amount of undercut with an optical line width measuring microscope. This undercut amount was incorporated into the FEM model and results in the large width of the anchor seen in Figure 5.4. The boundary conditions are fixed on the back and sides of this additional area. Table 5.4 list the results of the ANSYS testing and compares the final modeled resonance frequency to that of the measured devices.

Table 5.4 Measured and modeled cantilever resonant frequencies by wafer (Hz).

Cantilever length	W1 Modeled	W1 Measured	W3 Modeled	W3 Measured	W7 Modeled	W7 Measured	W9 Modeled	W9 Measured
100	109850	112375	194990	200550	192260	204300	173170	178300
200	29327	28718	51414	50940	48837	49920	46650	46840
300	13325	12719	23261	22890	21818	21950	21259	21090

The overall fit of the modeled data to the measured data was within 5% for all data points and within 3% for all but one data point. From this data the Young's Modulus of the PZT was determined to be 75 GPa which is considerably higher than the initial 25 GPa value estimated for generation I and II devices tested prior to this material testing but is reasonable given the range of published values for bulk PZT films of 58 to 86 GPa [25, 58].

5.6 PZT Stack Residual Stress and Stress Gradient

As will be shown in the following chapters, the residual stress within each layer of the PZT stack can have a significant effect on the resonant frequency of a clamped-clamped beam as well as the initial static deflection or beam shape. For the initial resonators, the wafer bow stress gauge describe in chapter 4 was used to measure the stack and individual layer stress during fabrication of the PZT device wafers by leaving a strip down the middle of the wafer with the full SiO_2/Pt/PZT/Pt stack for the wafer bow measurement. This resulted in the estimated value of 80 MPa for the average wafer stack stress that was used in the initially reported stress compensated data [26]. This stress was assumed to be uniform throughout the thickness of the beam. A more accurate model would be to obtain the stress levels in each layer and utilize the stress gradient to modify the resonant frequency of the clamped-clamped beams. Residual stresses are a major issue in the fabrication of any MEMS structure and several researchers have used wafer bow techniques on blanket thin-films to investigate the residual stresses associated with the sol-gel PZT process at ARL [59 - 60]. The stresses, as measured by wafer bow, for the generation II matrix of wafers listed in Table 5.3 are shown in Table 5.5.

Table 5.5 Thin film residual stresses.

Wafer #	SiO_2 thick (nm)	SiO_2 stress (Mpa)	Bottom Pt thick (nm)	Bottom Pt stress (Mpa)	PZT thick (nm)	PZT stress (Mpa)	Top Pt thick (nm)	Top Pt stress (Mpa)
W1	1060.2	55	135.0	1677	5303	184	200.0	24
W2	1084.2	-13.5	135.0	1682	10430	153	190.0	26
W3	2133.5	0.5	135.0	1733	5473	139	200.0	66
W4	2120.6	1.1	135.0	1803	10632	158	195.0	28
W5	1034.7	24.1	85.0	2520	10883	260	100.0	126
W6	1028.8	31.9	85.0	2590	5159	318	105.0	178
W7	1974.3	-52.9	85.0	2572	5195	325	100.0	29
W8	1987.4	21	85.0	3350	10125	224	105.0	100

From Table 5.5, the SiO_2 layer is lightly stressed and ranged between -50 and +50 MPa, the bottom Pt is highly stressed with the thin bottom Pt ranging from 1600-1800 MPa and the thick bottom Pt ranging from 2500-3300 MPa, the PZT ranged from 140-325 MPa and the top Pt from 24-178 MPa. From this data it is easy to see that there is a large stress gradient within the as deposited films. Typically this stress gradient results in an upward curvature of the PZT MEMS device as seen for the severe case in Figure 5.5 for a cantilever from a generation I device wafer.

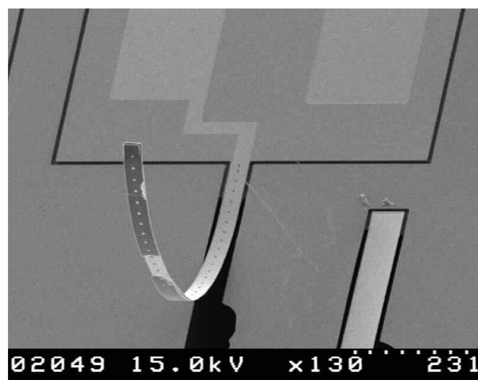

Figure 5.5 Example of stress-induced cantilever static deflection.

The overall average stack stress for these films varied from approximately 100 MPa to 200 Mpa tensile, slightly larger than the 80 MPa measured on the initially reported devices. This overall tensile stress is generally given as the reason for the increase in resonance frequency found in the clamped-clamped beam resonators over their expected unstressed modeled resonant frequencies. These stress measurements were taken after each thin film deposition and anneal step and they do not account for relaxation and modification to the stress within each layer during subsequent anneal, etch, and deposition steps for the remaining thin films or for the final release step where the underlying silicon is removed.

To verify the actual final stress gradient in the as fabricated devices, the ANSYS 8.0 FEM model used for the cantilever resonance testing was modified to model cantilever tip deflection from a residual stress gradient created by inputting false CTEs for each material and then applying a uniform temperature (-50 °C) to strain the material and create the appropriate stress gradient. The static FEM analysis was performed with nonlinear geometries options turned on to account for the large tip deflections seen in actual devices. The modeled data was then compared to actual residual stress induced deflections for the 100, 200, and 300 μm SiO_2/Pt, SiO_2/Pt/PZT, and SiO_2/Pt/PZT cantilever beams.

An iterative process was then used that started with values for the residual stresses similar to those listed for the as deposited films in Table 5.5. The values for the false CTEs used for each film were varied until the model matched the measured cantilever deflection. These values were then put into a clamped-clamped beam FEM model to verify that the

stress would give the proper resonant frequency for a stressed clamped-clamped resonator.

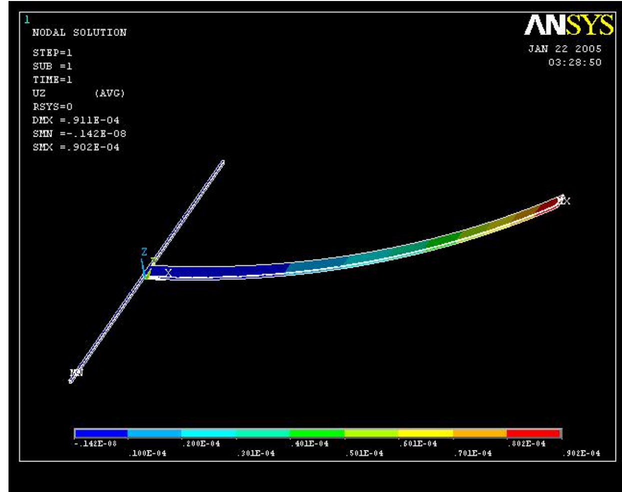

Figure 5.6 ANSYS output for residual stress deformation of a cantilever.

Figure 5.6 shows a typical ANSYS output for the residual stress measurements and Table 5.6 shows a comparison of the actual cantilever deflections to the modeled cantilever deflections.

Table 5.6 Measured and modeled stress-induced cantilever deflections.

Length	W1 Measured (μm)	W1 Modeled (μm)	W4 Measured (μm)	W4 Modeled (μm)	W7 Measured (μm)	W7 Modeled (μm)	W9 Measured (μm)	W9 Modeled (μm)
100	8.62	8.6	8.62	4.5	8.62	6.7	10.5	7.2
200	30.45	30	17.85	16	26.25	25.6	26.25	25
300	57.75	63.9	31.5	34.5	52.5	56.4	52.5	53.1

From Table 5.6, the data matched to within +/- 5 μm over the four different cantilever structures (varying film thickness) and three different lengths. From this testing, a matrix of false CTEs was developed based on varying film thickness. The goal of generating this

mapping was to be able to apply the data to future FEM models and new resonators designs to get good estimates of the stress-induced changes to the resonant frequencies. The mapping of film thickness to false CTE (used with an applied -50ºC Temp load) is given in Table 5.7.

Table 5.7 Mapping of false CTE to film thickness.

Material	Thickness (μm)	False CTE (x 10^{-6}/ºC)
Oxide	1.0	-20
Oxide	2.0	-15
Bottom Pt	0.085	50
Bottom Pt	0.135	33
Bottom Pt	0.2	33
PZT	0.5	40
PZT	1.0	25
Top Pt	0.1	25
Top Pt	0.2	15

As mentioned previously, these values were calculated by iterating between measured cantilever deflection data, modeled cantilever deflection data, measured clamped-clamped resonator data, and modeled clamped-clamped resonator data. The clamped-clamped beam data used for the validation of these values as well as the clamped-clamped data used to validate the ability to predict new designs is given in Chapter 6. For the clamped-clamped beam case these values were able to predict the resonant frequency for alternative film stack thickness to within 7% in all but one case.

In performing comparisons between modeled and measured cantilever deflections and the measured clamped-clamed resonance, a clearer picture of the overall stress gradient was obtained. The stress gradients in Table 5.5 gave the appropriate cantilever deflections but

resulted in a clamped-clamped resonance frequency that was too high. Figure 5.7 shows the modeled stress gradient at the electrode for a clamped-clamped resonator from wafer W9.

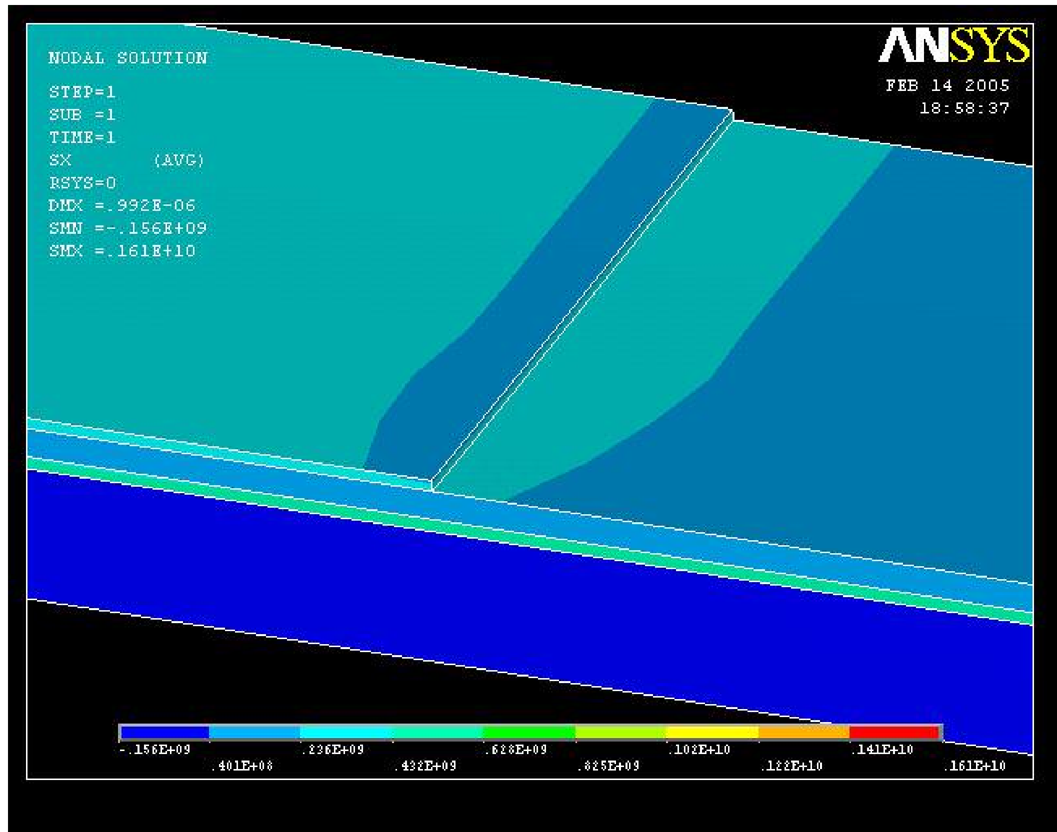

Figure 5.7 Modeled stress gradient at electrode transition.

Table 5.8 shows a comparison of the wafer bow measurements from Table 5.5 versus the modeled stress gradients across each layer determined by the iteration between the cantilever deflection and resonator resonance data. Validation of the resonance data is given in Chapter 6.

Table 5.8 Comparison of modeled to measured residual stresses.

Wafer #	SiO_2 stress Modeled (MPa)	SiO_2 stress Measured (MPa)	Bottom Pt stress Modeled (MPa)	Bottom Pt stress Measured (MPa)	PZT stress Modeled (MPa)	PZT stress Measured (MPa)
W1	-62 to -90	55	134 to 631	1677	196 to 263	184
W2	-48 to -61	-13.5	225 to 734	1682	91 to 179	153
W3	-44 to -58	0.5	205 to 632	1733	208 to 284	139
W4	-47 to -57	1.1	266 to 716	1803	115 to 194	158
W5	-79 to -95	24.1	322 to 733	2520	110 to 154	260
W6	-70 to -94	31.9	250 to 714	2590	194 to 236	318
W7	-43 to -58	-52.9	342 to 703	2572	204 to 254	325
W8	-46 to -57	21	367 to 728	3350	122 to 163	224

From Table 5.8, the modeled data and the iterative process described above reveals that the residual stress in the oxide layer in the final fabricated devices was actually compressive, and that the stress in the bottom Pt was significantly reduced from the values measured for the individual layers during fabrication.

5.7 PZT CTE Measurement

The next material property needed is the CTE for the PZT. The values for the Pt and SiO_2 were measured in the previous wafer bow experimentation. Bimorph cantilever beams have been used previously to measure the thermal properties through measuring the tip deflection for a given temperature input [61]. For a simple bimorph, the temperature induced curvature is given by

$$k = \frac{6b_1b_2E_1E_2t_1t_2(t_1+t_2)(\alpha_2-\alpha_1)}{(b_1E_1t_1^2)^2+(b_2E_2t_2^2)^2+2b_1b_2E_1E_2t_1t_2(2t_1^2+3t_1t_2+2t_2^2)}\Delta T\,. \tag{5.19}$$

From equation (5.19) it can be seen that for a given ΔT, the amount of curvature is dependent on the beam geometry, thickness of both materials, Young's modulus of both materials, and the CTE for both materials. So if the beam geometry is defined, the material properties for material 1 are known, the Young's modulus or CTE can be determined for material 2 given that the other one of them is known. This can be extended to multimorph materials such as the PZT stacks being studied for this work.

The ANSYS 8.0 FEM model used in section 5.6 for modeling the static cantilever tip deflection was modified to perform a second static thermal analysis with the proper CTEs inserted in place of the false CTEs used to create the initial static deflection. Again, the CTE for the PZT film is the only unknown in the model. Analysis was done with nonlinear geometries turned on to account for the large tip deflections that for some cantilevers was over 100 μm.

Fifty-four cantilevers from wafer W8 were tested and compared to the FEM model to verify the SiO_2 and Pt CTEs and to calculate the PZT CTE. Cantilever beams of 100, 200, and 300 μm and the following material stacks SiO_2/Pt, SiO_2/Pt/PZT, and SiO_2/Pt/PZT/Pt were subjected to temperatures of 23 ºC, 100 ºC, 150 ºC, and 200 ºC. Figure 5.8 shows a typical ANSYS result for a 200 μm cantilever at 100 ºC for the temperature deflected versus the initial stress induced deformed shape.

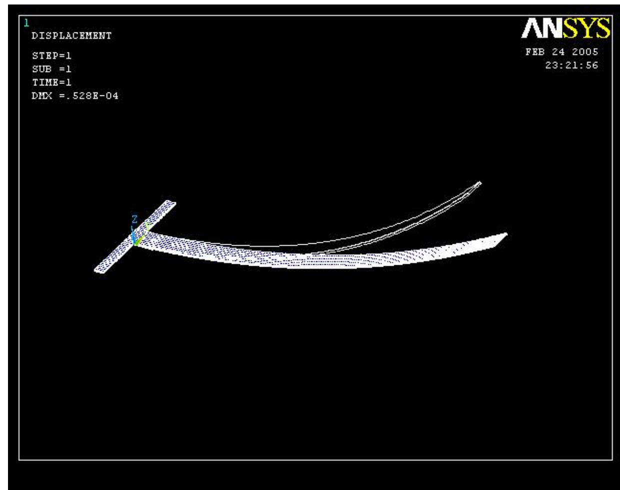

Figure 5.8 ANSYS result for a 200 μm thermally deflected beam at 100 °C.

The actual cantilever beam deflections were measured by first focusing on the tip of the deformed cantilever and then on the base of the cantilever using the optical defocusing technique described in chapter 4. Data from wafers W1, W4, W7, and W9 were used for this testing in order to include one device with each film thickness from the matrix of wafers listed in Table 5.3.

Initially the values for the CTE of Pt (7.12 x 10^{-6}) and SiO_2 (0.7 x 10^{-6}) obtained via the wafer bow measurements were put into the model of an Oxide/Pt cantilever to validate the model for the SiO_2 and Pt CTE values. A comparison to the actual data is given in Table 5.9. The data matched within the expected error except for the two data points on the 300 μm cantilever.

Table 5.9 Comparison of measured to modeled thermal-induced tip deflection.

		Initial Deflection (microns)	Wafer W8 Modeled/Measured Cantilever Temperature Induced Deflection Data (microns displaced from initial position)					
Stack Configuration	Cantilever Length	Measured 23 ºC	Measured 100 ºC	Modeled 100 ºC	Measured 150 ºC	Modeled 150 ºC	Measured 200 ºC	Modeled 200 ºC
Ox/Pt	100	5.1	1.4	1.1	1.4	1.8	3.2	2.5
Ox/Pt	200	17.7	3.0	3.9	4.6	6.5	7.9	9.0
Ox/Pt	300	44.6	12.3	8.5	16.8	14.0	24.2	19.5
Ox/Pt/PZT	100	6.7	0.7	0.7	0.7	1.2	1.2	1.6
Ox/Pt/PZT	200	25.9	5.1	2.5	5.1	4.2	6.8	5.8
Ox/Pt/PZT	300	55.1	6.5	5.5	9.5	9.0	14.2	12.5
Ox/PT/PZT/Pt	100	4.6	0.7	0.9	0.9	1.5	1.1	2.0
Ox/PT/PZT/Pt	200	16.6	2.5	3.3	3.5	5.5	6.8	7.3
Ox/PT/PZT/Pt	300	37.6	6.5	7.2	9.1	11.8	13.7	16.5

A model for an oxide/Pt/PZT cantilever was then developed and the value of the CTE for PZT was varied within the model until the modeled data closely approximated experimental deflection data for the same cantilever structures. This test resulted in a CTE for PZT of 3.5 x 10^{-6}/ºC, which is reasonable given reported values for PZT from 1 x 10^{-6}/ºC to 8 x 10^{-6} /ºC [62, 63]. All of the data points were within the error of the measurement technique and are listed in Table 5.9.

Finally, an Oxide/Pt/PZT/Pt cantilever stack was modeled and tested against an actual cantilever of the same structure and the data is reported in Table 5.9. A good approximation was obtained for all cantilever structures validating the values for the CTE of SiO_2 and Pt obtained via wafer bow and the value for PZT obtained by this technique.

Chapter 6. FEM Model and Material Property Validation

6.1 Clamped-Clamped Beam Theory

The boundary-value problem for an undamped beam in bending and under an axial load can be derived by means of the extended Hamiltion's principle or from the Lagrange's equations as [64, 65]

$$m\frac{\partial^2 y}{\partial t^2}+\frac{\partial^2}{\partial x^2}\left(EI\frac{\partial^2 y}{\partial x^2}\right)-\frac{\partial}{\partial x}\left(P\frac{\partial y}{\partial x}\right)=f\left(x,t\right) \tag{6.1}$$

where m is mass, y is the transverse motion, EI is the beam stiffness, P is an axial load, and $f(x,t)$ is an applied transverse force. Assuming a uniform beam along its length, equation (6.1) can be rewritten as

$$EI\frac{\partial^4 y}{\partial x^4}-P\frac{\partial^2 y}{\partial x^2}=-m\frac{\partial^2 y}{\partial t^2} \tag{6.2}$$

where the sign of P is positive for a tensile force and negative for a compressive force. When the beam vibrates transversely, the deflection at any point along the beam can be given by

$$y\left(x,t\right)=Y\left(x\right)\left(C_1\sin\omega t+C_2\cos\omega t\right). \tag{6.3}$$

Then substituting equation (6.3) back into (6.2) gives the following at t=0

$$EI\frac{d^4Y\left(x\right)}{dx^4}-P\frac{d^2Y\left(x\right)}{dx^2}+m\omega^2Y\left(x\right)=0. \tag{6.4}$$

The solution of Y(x) can be assumed to be

$$Y(x) = B_1 \cos \lambda_1 x + B_2 \sin \lambda_1 x + B_3 \cosh \lambda_2 x + B_4 \sinh \lambda_2 x \,. \tag{6.5}$$

Then by applying the following boundary conditions

$$Y(0) = Y^{'}(0) = Y(L) = Y^{'}(L) = 0 \tag{6.6}$$

to equation (6.5), leads to the characteristic equation

$$\cos \lambda_1 L \cosh \lambda_2 L - \frac{1}{2}\left(\frac{\lambda_2}{\lambda_1} - \frac{\lambda_1}{\lambda_2}\right)\sin(\lambda_1 L)\sinh(\lambda_2 L) = 1 \tag{6.7}$$

and expression for the mode shape of

$$\phi(x) = \cos(\lambda_1 x) - \cosh(\lambda_2 x) + \frac{\cos(\lambda_1 L) - \cosh(\lambda_2 L)}{\frac{\lambda_1}{\lambda_2}\sinh(\lambda_2 L) - \sin(\lambda_1 L)}\left(\sin(\lambda_1 x) - \frac{\lambda_1}{\lambda_2}\sinh(\lambda_2 x)\right). \tag{6.8}$$

Tilmans *et al.* reported that the approximate solution for (6.8) by the Rayleigh's energy method is [66]

$$\omega_n(P) \approx \frac{\alpha_n^2}{L^2}\sqrt{\frac{EI}{\rho A}\left(1 + \gamma_n \frac{PL^2}{12EI}\right)} \tag{6.9}$$

where α_n=4.73 and γ_n=0.295 for the fundamental mode and α_n=7.853 and γ_n=0.145 for the second mode. From (6.9) an applied tensile axial force will increase the resonant

frequency of the beam and an applied compressive axial force will decrease the resonant frequency which will approach zero until the compressive force equals the critical Euler Buckling load and the beam buckles at which point (6.9) is no longer valid.

The above development assumes Euler-Bernoulli beam theory where there are no shear deformation or rotary inertia effects. Euler-Bernoulli beam theory is valid for slender beams with a length-to-thickness ratio greater than 10 [40]. For this work, resonators with length to thickness ratios from 7.1 to 208 where tested with the smaller beams being on the edge of valid Euler-Bernoulli theory. The Timoshenko Beam model includes shear and rotation effects and has been shown by others to improve modeling at higher frequencies [67]. For a simply supported Timonshenko beam, the total correction compared to a Euler-Bernoulli beam will be ~1.7% [65]. For this work, only the Euler-Bernoullli beam model is used since most of the research is performed on resonators with length to thickness ratios greater than 60 and as will be seen later in this chapter, the errors associated with correct measurement of material properties, beam length, and anchor undercut are much larger than those expected from neglecting shear deformations and rotary inertia.

6.2 Basic Finite Element Model

The natural frequency and associated mode shapes of a clamped-clamped beam can also be obtained by finite element modeling. The FEM method presented here and used for the initial resonators was a 2-D FEM routine that was outlined by Baz [39].

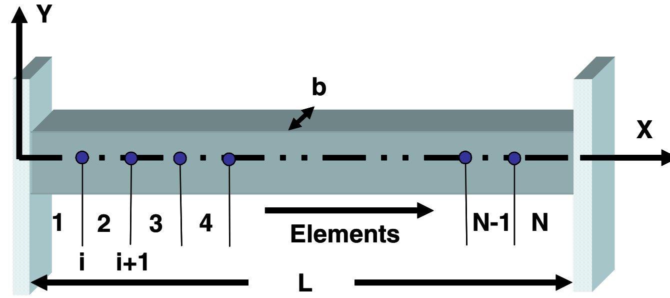

Figure 6.1 2-D FEM elements for clamped-clamped beam.

Figure 6.1 shows a generalized clamped-clamped beam cross-section where *L* is the beam length, *b* is the beam width, and *N* is the number of elements. The kinetic and potential energy for any element along the beam can be given as

$$KE = \frac{1}{2} m \int_0^L y_t^2 dx \text{, and} \tag{6.10}$$

$$PE = \frac{1}{2} EI \int_0^L y_{xx}^2 dx \tag{6.11}$$

where *m* is the mass of the element, *E* is the Young's Modulus, and *I* is the area moment of inertia. The deflection at any point along the beam can be described by the cubic shape function

$$y(x) = a_1 + a_2 x + a_3 x^2 + a_4 x^3 = \{f\}^T \{\alpha\} \tag{6.12}$$

where $\{f\} = \{1, x, x^2, \ldots\}$ and $\{\alpha\} = \{a_1, a_2, a_3, \ldots\}$ and the beam slope can be given by

$$y_x(x) = a_2 + 2a_3 x + 4a_4 x^2 \,. \tag{6.13}$$

Given the boundary conditions for a clamped-clamped beam of $y(0)=0$, $y(L)=0$, $y_x(0)=\theta_i$, and $y_x(L)= \theta_j$, equations (6.12) and (6.13) the following can be written for the displacement and rotation of each element along the beam:

$$\begin{Bmatrix} y_i \\ \theta_i \\ y_j \\ \theta_j \end{Bmatrix} = \begin{bmatrix} 1 & 0 & 0 & 0 \\ 0 & 1 & 0 & 0 \\ 1 & L & L^2 & L^3 \\ 0 & 1 & 2L & 3L^2 \end{bmatrix} \begin{Bmatrix} a_1 \\ a_2 \\ a_3 \\ a_4 \end{Bmatrix} \quad \text{or}$$

$$\begin{Bmatrix} a_1 \\ a_2 \\ a_3 \\ a_4 \end{Bmatrix} = \frac{1}{L^2} \begin{bmatrix} L^3 & 0 & 0 & 0 \\ 0 & L^3 & 0 & 0 \\ -3L & -2L^2 & 3L & -L^2 \\ 2 & L & -2 & L \end{bmatrix} \begin{Bmatrix} \upsilon_i \\ \theta_i \\ \upsilon_j \\ \theta_j \end{Bmatrix} = \{T\}\{\delta_e\}. \tag{6.14}$$

Rearranging and substituting into (6.12) gives

$$y(x) = \{f\}^T [T]\{\delta_e\} = \{A\}\{\delta_e\}. \tag{6.15}$$

Then by substituting (6.15) into (6.10) and (6.11) the following expressions for the kinetic and potential energy are obtained:

$$KE = \frac{1}{2} m \left\{ \dot{\delta} \right\}^T \left[\int_0^L \{A\}^T \{A\} dx \right] \left\{ \dot{\delta} \right\} \text{ and} \tag{6.16}$$

$$PE = \frac{1}{2} EI \{\delta_e\}^T \left[\int_0^L \{A_{xx}\}^T \{A_{xx}\} dx \right] \{\delta\}. \tag{6.17}$$

Then, using the Lagrangian method, the equation of motion for the beam can be derived as

$$\frac{d}{dt}\left[\frac{\partial L}{\partial\left\{\dot{\delta}_e\right\}}\right]-\frac{\partial L}{\partial\{\delta_e\}}=\{Q_e\} \tag{6.18}$$

where

$$L = KE - PE\,, \tag{6.19}$$

and Q is the external loads. Substituting (6.16), (6.17), and (6.18) in (6.19) yields the equation of motion

$$[M_e]=\left\{\ddot{\delta}_e\right\}+[K_e]\{\delta_e\}=\{Q_e\} \tag{6.20}$$

Where the mass and stiffness matrices are given by

$$[K_e]=\frac{EI}{L^3}\begin{bmatrix} 12 & 6L & -12 & 6L \\ 6L & 4L^2 & -6L & 2L^2 \\ -12 & -6L & 12 & -6L \\ 6L & 2L^2 & -6L & 4L^2 \end{bmatrix} \text{ and} \tag{6.21}$$

$$[M_e]=\frac{mL}{420}\begin{bmatrix} 156 & 22L & 54 & -13L \\ 22L & 4L^2 & 13L & -3L^2 \\ 54 & 13L & 156 & -22L \\ -13L & -3L^2 & -22L & 4L^2 \end{bmatrix}. \tag{6.22}$$

The elements can then be assembled to represent the entire beam

$$\sum\nolimits_{e=1}^{n}[M_e]\left\{\ddot{\delta}\right\}+\sum\nolimits_{e=1}^{n}[K_e]\{\delta_e\}=\sum\nolimits_{e=1}^{n}Q_e \tag{6.23}$$

and boundary conditions can be applied to obtain the final equation of motion prior to determining the natural frequencies by solving the following eigenvalue problem for ω

$$[K_0][M_0]^{-1}\{\delta\} = \omega_n^2\{\delta\}. \quad (6.24)$$

The PZT beam resonators used for this work are composite structure so the mass and stiffness matrices must account for all layers by defining them as

$$m = \sum_{i=1}^{4} \rho_i A_i \text{ , and} \quad (6.25)$$

$$EI = \sum_{i=1}^{4} E_i I_i \text{ .} \quad (6.26)$$

Where i=1, 2, 3 and 4 represents the oxide, bottom platinum, PZT, and top platinum layers. Even with only ten elements, the 2-D FEM model matched the results for the exact solution given by equation (6.9), but they both overestimated the resonant frequency at shorter beam lengths or higher frequencies and underestimated the frequency at longer beam lengths or lower frequencies. These models assumed a uniform cross section along the length of the resonator (no step at electrode transition), a uniform stress gradient, and perfect boundary conditions. As will be seen in section 6.3, this is not the case and to better model these conditions, a full ANSYS 8.0 3-D FEM model was created for performing modal analysis and studying resonator behavior.

6.3 Clamped-Clamped Resonator Comparisons to 3-D FEM

The clamped-clamped beam anchors within the FEM were modified to simulate the anchor undercutting seen in the actual devices. The edges of this area were given rigid boundary conditions of zero translation and rotation. The model was also cut in half down the center of the beam using symmetry boundary conditions to reduce the number of elements. The general model geometry is shown in Figure 6.2.

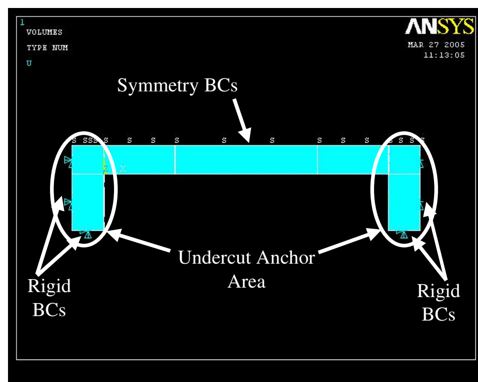

Figure 6.2 ANSYS boundary conditions.

FEM models for 25 µm through 400 µm clamped-clamped beams were developed and tested against fabricated clamped-clamped beam resonators. The values for the depth of the undercut area were measured for each wafer by physically breaking the overhang area with a probe and optically measuring the amount of undercut. The measured values for the undercutting are reported in Table 6.1.

Table 6.1 Resonator undercut amount by wafer.

Wafer #	Depth of Undercut (μm)
W1	9
W2	14
W3	4
W4	9
W5	7
W6	10
W7	5
W8	9
W9	10

Figure 6.3 shows a close up of the anchor area from wafer 9.

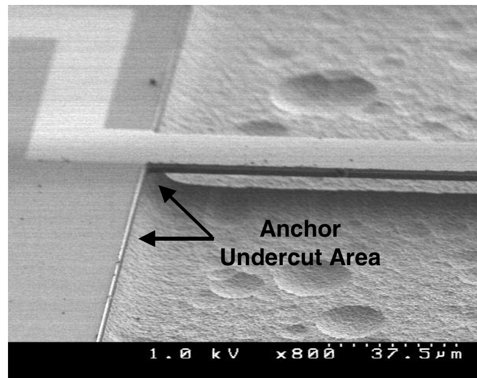

Figure 6.3 SEM of anchor undercut area.

The residual stress within each thin film was incorporated into the model by first performing a static analysis with the false CTEs and uniform temperature which are listed in Table 5.7. The method for developing the values for these parameters is also discussed in Chapter 5. This initial step prestressed the clamped-clamped beam structure. The nonlinear geometry and stress stiffening analysis options were turned on during this step. Once the solution was complete, the deflected beam geometry was uploaded using the

upcoord command and a modal analysis was performed with nonlinear geometry and stress stiffening options turned on.

Figure 6.4 shows a comparison of the ANSYS 8.0 model to the measured resonant frequency for a resonator from W7. The prestressed 3-D ANSYS 8.0 model is significantly better than the previous models at lower frequencies or longer beam lengths and overall gives a good estimate, within 10% over entire range, of the resonator frequency.

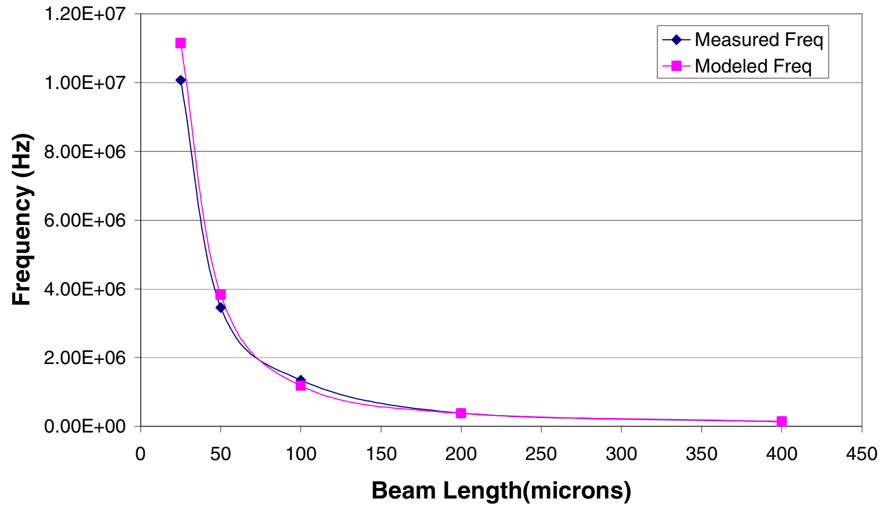

Figure 6.4 Comparison of ANSYS 8.0 model to measured first natural frequency.

There are four main sources of error between the model and measured resonance values. These are errors in measurement of the actual beam geometry, measurement of the amount of anchor undercut, material properties used, and errors in the stresses incorporated into each layer. Figure 6.5 shows a plot of the fractional frequency error, $\Delta f / f_o$, associated with a +/- 1 μm error in beam length, a +/- 1 μm error in measured

beam undercut, a +/- 10% error in value of material properties, and a +/- 10% error in the amount of stress incorporated into the model.

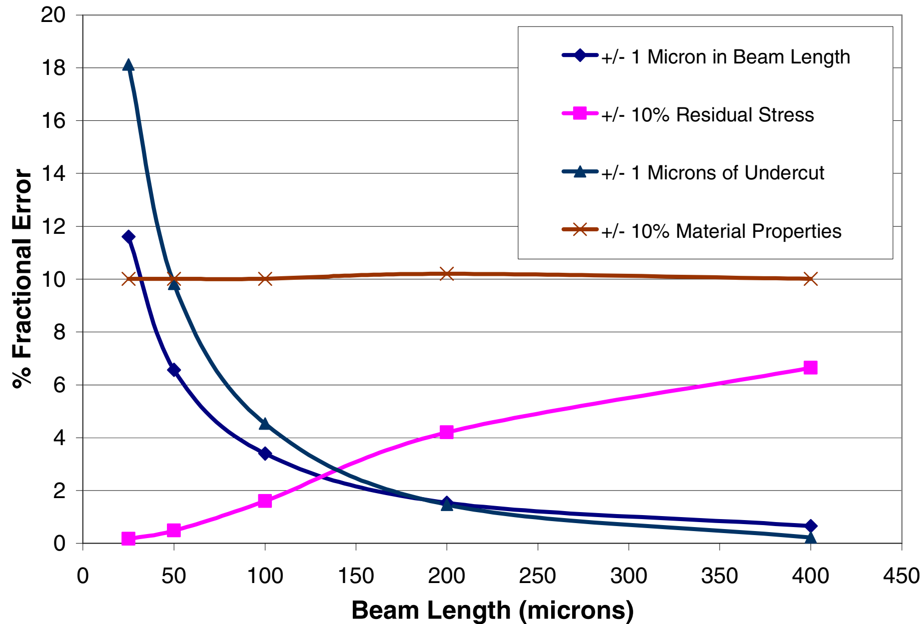

Figure 6.5 Plot of errors associated with variations in beam length, anchor undercut, material properties, and residual stress.

From Figure 6.5, errors in measuring beam length and undercutting, as expected, increase exponentially since frequency goes as the inverse of the length squared. Errors associated with the material properties remain constant as beam lengths are varied and the error associated with residual stress decreases and beam lengths are decreased to increase the resonant frequency. This is also expected by examining equation (6.9) which shows that the change in frequency associated with a residual stress goes as $P^{0.5}$ for the induced force but as L^{1} for the beam length. Figure 6.6 plots the accumulated error associated with these four parameters against the measured and modeled frequency of the data plotted in Figure 6.4.

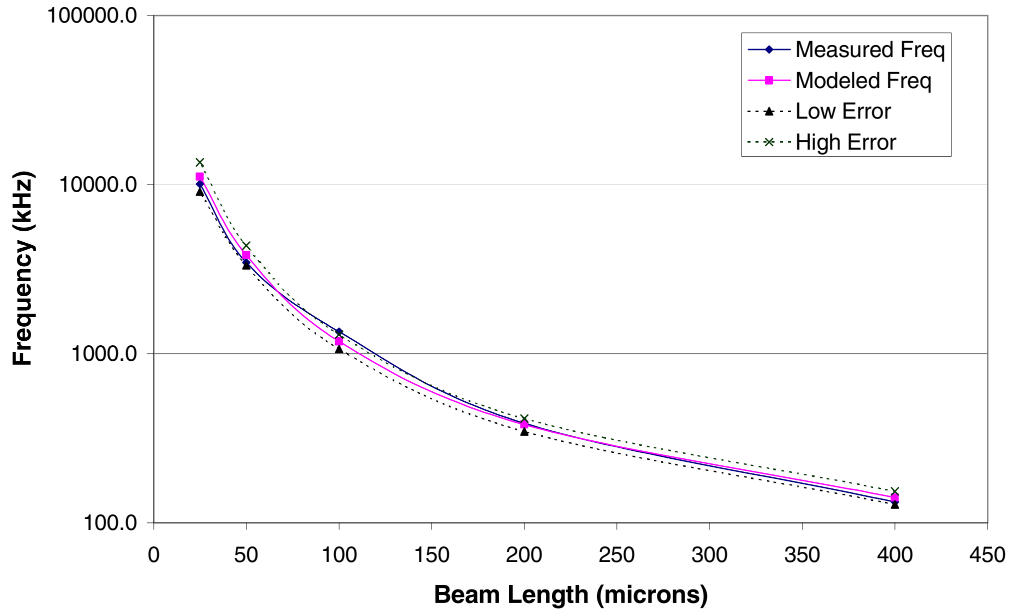

Figure 6.6 Plot of modeled frequency data with associated error and measured first natural frequencies.

From Figure 6.6, the measured data points are within the error except the point at 100 μm that falls just outside of the error bounds. Therefore, the model does well in predicting the resonant frequencies but from Figures 6.5 and 6.6, the estimated errors may be a little low.

Next, the model was used to predict the resonant frequencies and modes shapes for other resonator geometries and for devices fabricated on wafers that were not used in the development of the material property values. The goal was to test how well the model, and derived material properties, could be used for new clamped-clamped PZT designs as well as for alternative resonator designs such as free-free resonators. Resonators from wafers W1, W4, W7 and W9, which were used for the material property data developed in Chapter 5, were used as an initial validation test. Then resonators from wafers W3,

W5, W6, and W8, which all have different material thickness values from the previous set of wafers, were modeled to see how well the developed values could predict the resonance frequency for new clamped-clamped beam resonator structures. Table 6.2 shows a comparison of the measured and modeled resonance frequencies for the initial set of wafers used to develop the material properties in Chapter 5.

Table 6.2 Resonant frequencies for resonators from wafers with prior material property and stress analysis.

Wafer	Measured 400 µm beam (Hz)	Modeled 400 µm beam (Hz)	Measured 200 µm beam (Hz)	Modeled 200 µm beam (Hz)
W1	148000	151312	359000	343637
W4	160000	163936	444000	431310
W7	132650	141107	386750	380291
W9	140000	142404	382000	372325

From Table 6.2, the measured and modeled resonant frequencies on the wafers for which the residual stress was developed are all within 6%. Table 6.3 shows the measured and modeled resonance frequencies for the remaining wafers for which previous material and stress analysis was not done.

Table 6.3 Resonant frequencies for resonators from wafers without prior material property and stress analysis.

Wafer	Measured 400 µm beam (Hz)	Modeled 400 µm beam (Hz)	Measured 200 µm beam (Hz)	Modeled 200 µm beam (Hz)
W3	151000	147517	452000	431238
W5	136250	139307	313000	334306
W6	132000	151225	317000	339271
W8	138875	141114	406000	381261

From Table 6.3, all results are within +/- 7% except one, which falls at approximately 13%. Therefore the values determined for false CTEs developed in Chapter 5 for inducing residual stress can be reasonably applied generally across to other clamped-clamped beam resonator designs with varying thickness combinations and stress levels.

The model was also compared to measured values for the first, second, and, where possible, the third resonant modes for each resonator. Figures 6.7 through 6.9 show the first three modeled mode shapes for a 400 µm clamped-clamped beam resonator from wafer W5 compared to the actual measured mode shape via the LDV test setup described in Chapter 4.

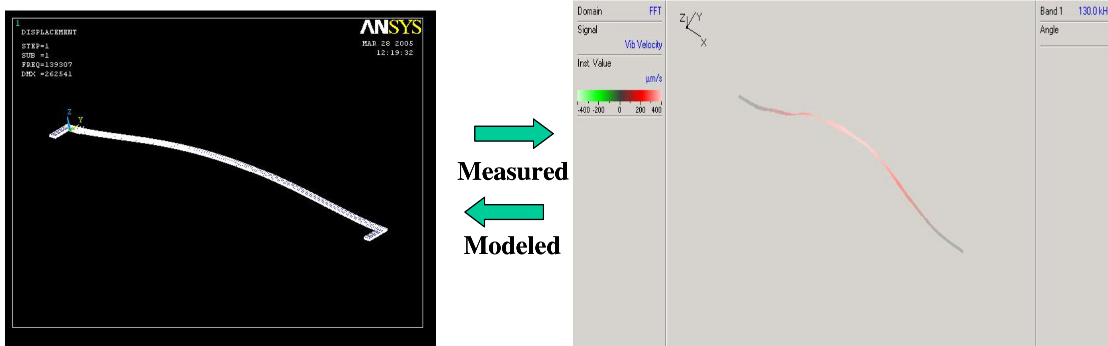

Figure 6.7 Modeled and measured first resonant mode for a 400 µm resonator.

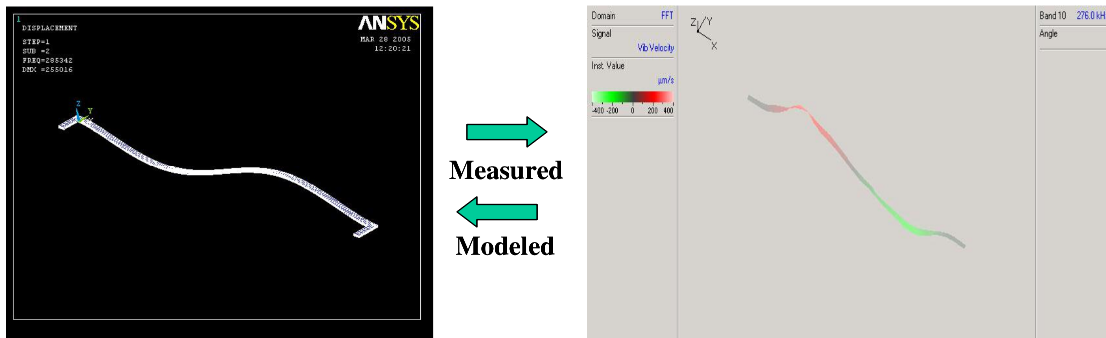

Figure 6.8 Modeled and measured second resonant mode for a 400 µm resonator.

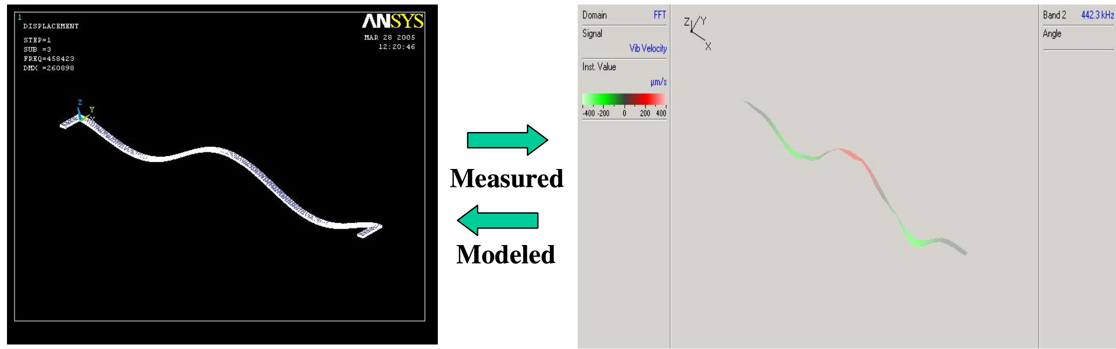

Figure 6.9 Modeled and measured third resonant mode for a 400 μm resonator.

Table 6.4 shows the frequency comparison of the first, second, and were possible the third modes for all of the test wafers. Good approximations for the resonant frequencies for the first three modes of vibration for all test wafers were achieved.

Table 6.4 Modeled and measured values frequencies for a 400 μm resonator.

Wafer	Measured mode 1 (Hz)	Modeled Mode 1 (Hz)	Measured mode 2 (Hz)	Modeled Mode 2 (Hz)	Measured mode 3 (Hz)	Modeled Mode 3 (Hz)
W1	148000	151312	295859	295653	462813	459802
W3	151000	147517	328000	314746	NA	546649
W4	160000	163936	347031	346543	NA	588693
W5	136250	139310	281016	285340	451016	458420
W6	132000	151123	265078	298340	415313	462380
W7	133750	141107	295781	298867	NA	509223
W8	138875	141114	308281	305881	NA	527917
W9	140000	142404	300000	299150	NA	505660

6.4 Free-Free Resonator Comparison to 3-D FEM

Free-free beam resonators have been studied for electrostatic resonator designs and have shown improved Qs through reduced anchor loss, but typically result in an increase number of vibration modes that can impact the overall performance of the resonators [68]. For the fabricated free-free resonators, beam lengths were held consistent with those

for the clamped-clamped beam case and the anchor lengths were set at one-quarter the beam length, a fixed 50 μm, and a fixed 20 μm. The anchors were not optimized for these initial designs. A subsequent work was performed to develop design rules for free-free PZT based resonators [27]. Figure 6.10 shows a schematic of a free-free resonator with a single-side drive electrode where both the drive and sense electrodes are equally distributed around an anchor point.

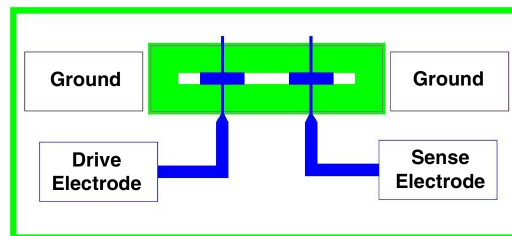

Figure 6.10 Schematic of a single-side drive free-free resonator design.

Figures 6.11 through 6.13 show the results for modeled and measured vibration modes for a single-side drive 200 μm free-free resonator with 50 μm anchors from wafer W9.

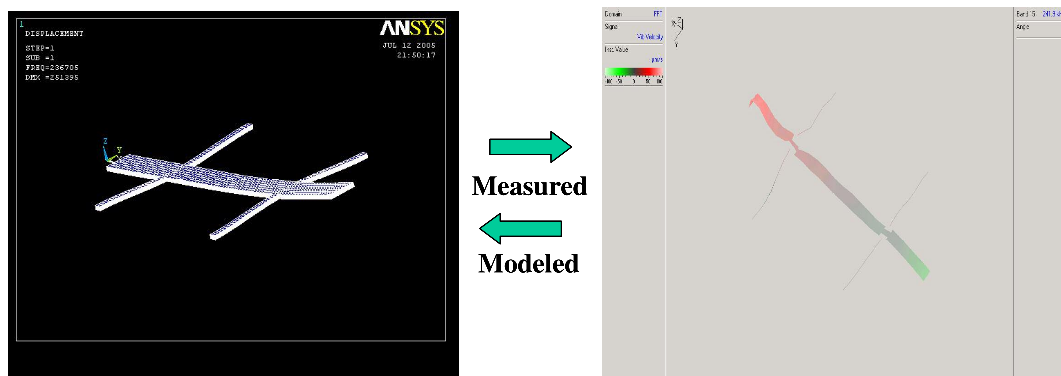

Figure 6.11 Modeled and measured "teeter-totter" first resonant mode for a free-free beam resonator.

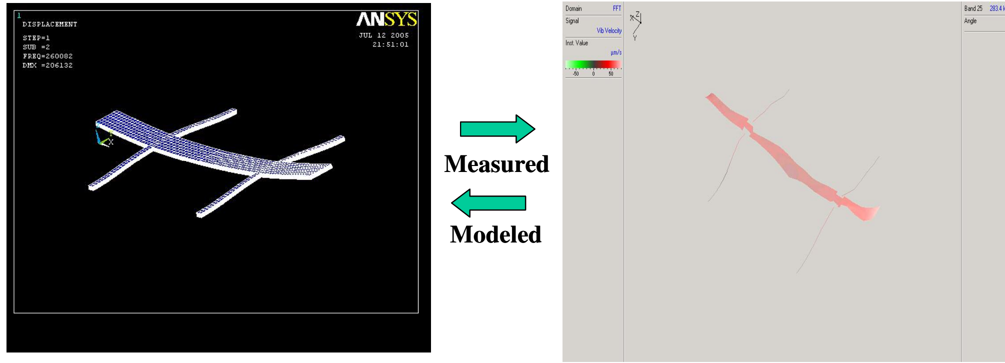

Figure 6.12 Modeled and measured "trampoline" second resonant mode for a free-free beam resonator.

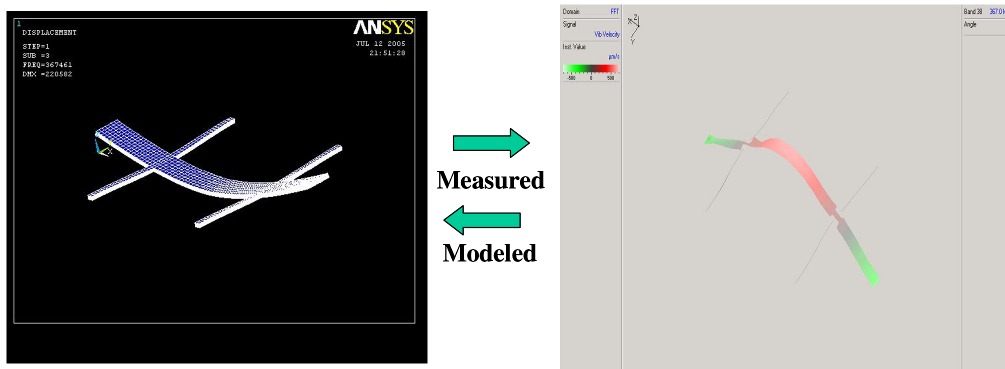

Figure 6.13 Modeled and measured "bending" third resonant mode for a free-free beam resonator.

A comparison of these modeled values to actual measured frequency values is listed in Table 6.5 and the velocity spectrum from the LDV measurement is shown in Figure 6.14. The first peak is the teeter-totter mode, the second is the trampoline mode, and the third is the bending mode.

Table 6.5 Comparison of free-free measured and modeled frequencies.

Mode	Measured Frequency (kHz)	Modeled Frequency (kHz)
Mode 1	240	237
Mode 2	283	260
Mode 3	367	368

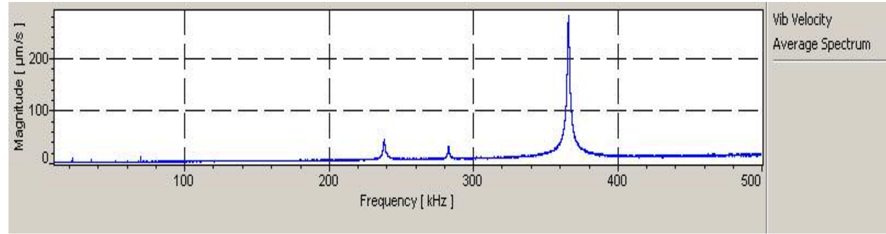

Figure 6.14 LDV velocity spectrum for a 200 µm free-free resonator.

The sequence/order and frequency of the teeter-totter, trampoline, and bending mode shapes are very sensitive to residual stress levels and material properties so the close agreement for the free-free resonators further validates the material properties and stress levels determined for the PZT structure.

6.5 Resonator Thermal Stability Comparison to 3-D FEM

During thermal cycling, the ratio of the substrate CTE to that of the composite CTE of the resonator determines the overall thermal stability along with stress gradient effects for the multi-material resonator stack structures. For modeling thermal effects on the resonators, a new FEM model that incorporated the silicon substrate was built. Figure 6.15 shows the structure used for the thermal stability modeling.

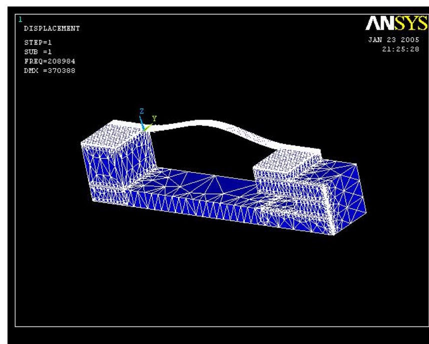

Figure 6.15 ANSYS model for resonator thermal stability modeling.

The effect of an applied temperature on the structure was accomplished by first performing a static analysis with the measured CTEs from Chapter 5 and a uniform applied temperature. This initial step prestressed and deformed the clamped-clamped beam structure. The nonlinear geometry and stress stiffening analysis options were turned on during this step. Once the solution was complete, the deflected beam geometry was uploaded using the "upcoord" command and a modal analysis was performed with nonlinear geometry and stress stiffening options turned on. Multiple thermal analysis are not possible prior to performing the modal analysis, so these models did not include an initial prestressed condition prior to the application of temperature and only show the relative change in stress and frequency about the unstressed condition for a given temperature change.

Figure 6.16 shows a comparison of the measured values for a 200 μm long clamped-clamped beam resonator from wafer W1 to the modeled values for the same device.

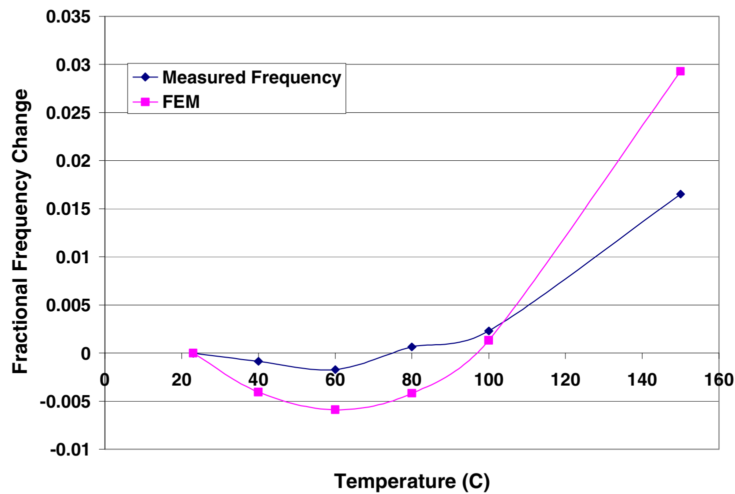

Figure 6.16 Comparison of ANSYS thermal model to measured resonant frequencies.

The modeled data approximates the measured data within a few percent up to approximately 100 °C and then slowly increases relative to the measured value. One item that was not considered and could account for the error at higher temperatures is that the model does not incorporate the temperature dependence of the Young's Modulus for the various materials in the stack. From Figure 6.16, the modeled and measured frequency initially drops as the temperature is increased from 20 to 60 °C and then begins to increase as the temperature is increased further. This dip and then increase in frequency is a result of the changing residual stresses and stress gradients within the PZT stack. Table 6.6 shows how the stress gradient within the stack at the quarter length point and the center beam deflection changes as the temperature is increased and the resultant effect on the resonant frequency from this change in the stress gradient. The center point of the beam is deflected downward with the application of temperature. This will be significant for the data presented in Chapters 8 and 9.

Table 6.6 Stress gradient in x-direction, beam deflection, and frequency as a function of temperature.

Temperature	Modeled Oxide Stress (MPa)	Modeled Pt Stress (MPa)	Modeled PZT Stress (MPa)	Modeled Center Deflection (μm)	Measured Frequency (Hz)
Room Temp	-53 to -85	115 to 608	154 to 220	0.75	364531
Δ at + 20 ºC	+3 to +4	-11 to - 24	+1 to –0.7	-0.08	364219
Δ at + 40 ºC	+6 to +8	-13 to -56	+1 to -5	-0.18	363906
Δ at + 40 ºC	+10 to +13	-20 to -87	+3 to -7	-0.28	364766
Δ at + 80 ºC	+13 to +18	-26 to -117	+4 to -10	-0.38	365371

Chapter 7. Uncompensated Resonators

7.1 Generation I Resonator Design and Fabrication

As stated earlier, the design of the initial clamped-clamped beam resonators for this work was based on the clamped-clamped ZnO resonators reported by DeVoe [40]. In fact, the first devices used the exact same mask set so that a direct comparison between the PZT and ZnO resonators could be made in order to see the impact of employing PZT for piezoelectric transduction. The mask set from DeVoe included the 200 μm and 400 μm long clamped-clamped beam resonators that were used as the basis for this initial design and comparison.

Resonators were fabricated using the backside release process described in Chapter 3. To implement the sol-gel PZT thin films in lieu of the ZnO films, a sputtered Pt bottom electrode with a Ta adhesive layer and a sputtered Pt top electrode were used in place of the Al electrodes used by DeVoe. The initial thickness of the SiO_2, Ta, Pt, and PZT layers was selected based on the standard process at ARL for PZT thin films at the time these resonators were fabricated. Table 7.1 shows the desired an actual thickness for each layer.

Table 7.1 Initial film thickness generation I resonators.

Material	Desired Thickness (μm)	Actual Thickness (μm)
SiO_2	1.0	0.9
Ta	0.02	0.02
Bottom Pt	0.17	0.17
PZT	0.5	0.48
Top Platinum	0.2	0.25

Figure 7.1 shows SEM images of a fabricated generation I resonator. From the SEM, severe bowing is present in these generation I resonators. This bow is caused by the residual stresses gradient within the thin films.

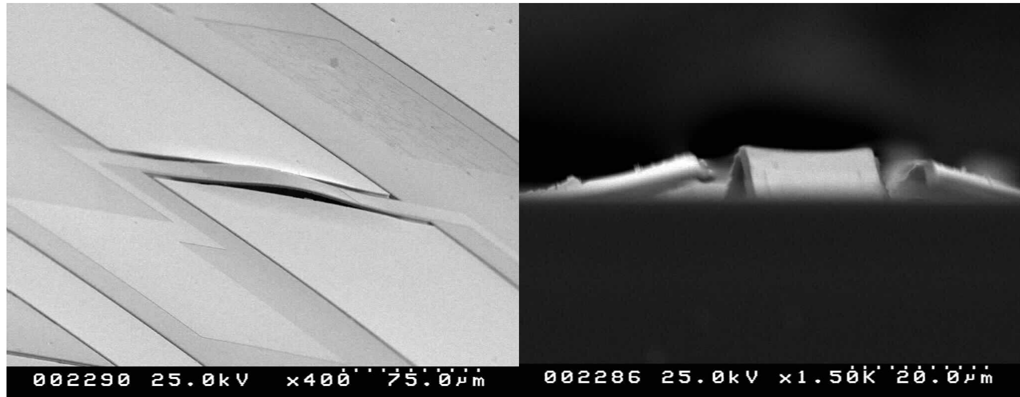

Figure 7.1 SEM images of fabricated generation I resonators showing beam buckling.

7.2 Generation I Resonator Performance

Figure 7.2 shows an SEM image of one of the ZnO clamped-clamped beam resonators fabricated by DeVoe, and Figure 7.3 shows the typical measured performance for a 400 μm ZnO resonator [20].

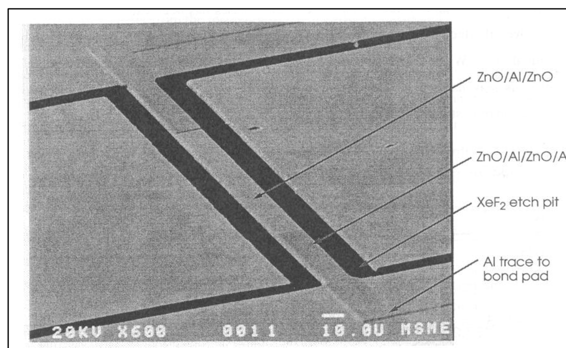

Figure 7.2 SEM image of a ZnO clamped-clamped beam resonator.

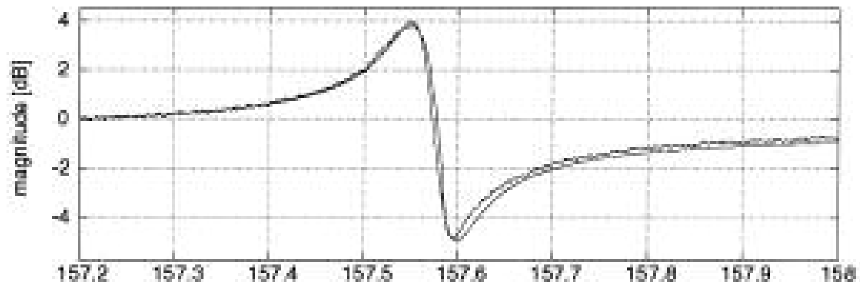

Figure 7.3 Typical performance of a ZnO clamped-clamped beam resonator.

For the 400 μm ZnO clamped-clamp beam resonator, the demonstrated resonance frequency was approximately 158 kHz with a Q of 3700. These Qs had to be backed out analytically since the resonant peaks were only approximately 4 dB and were not large enough to get good measurements for the 3 dB bandwidth. The 200 μm clamped-clamped beam ZnO resonator demonstrated a resonance frequency of ~859.6 kHz and a Q of 1580. The phase lag was 58 and 13 degrees respectively [20]. These measurements were the basis for the initial evaluation of feasibility of PZT and validation that the increase piezoelectric coefficient would lead to increased resonator admittance.

The magnitude response of the generation I resonators was tested on the vacuum probe station described in Chapter 4. Figure 7.4 shows the response of a 400 μm resonator between 0 and 500 kHz. Multiple peaks are present representing the different resonant modes.

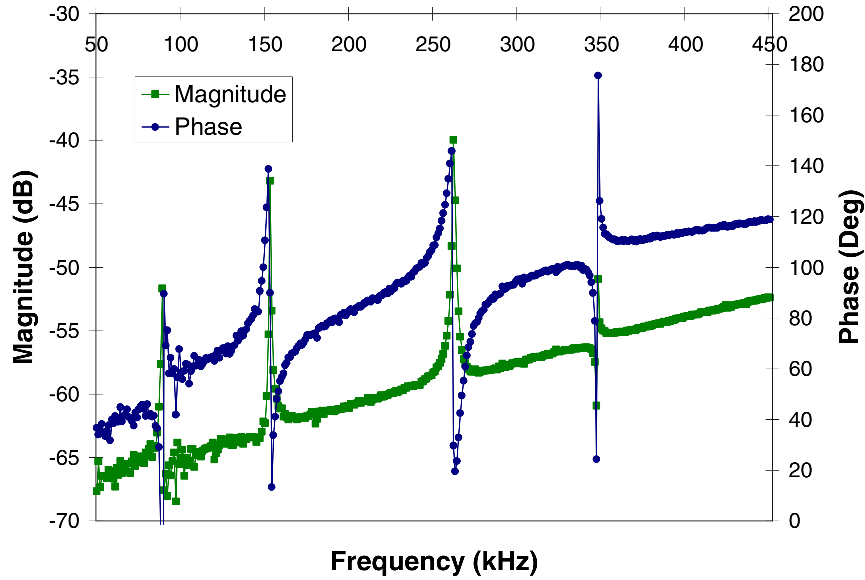

Figure 7.4 Full frequency response of 400 μm generation I resonator.

From Figure 7.4, the 400 μm resonator had resonant peaks at approximately 90 kHz, 153 kHz, 262 kHz, and 348 kHz representing four different vibration modes. As expected from the discussion in Chapter 2, all of the resonant peaks were significantly larger than the original ZnO resonator peaks seen in Figure 7.3. Resonant signals were as high as 20 dB above the noise floor vs. the 2-4 dB seen in the ZnO resonators with the same mask design [20]. Figures 7.5 and 7.6 show smaller frequency span views for the magnitude of the first two resonant peaks. Although the resonant peaks are much more distinguished that the ZnO resonators, the measured Qs for the two peaks in Figures 7.5 and 7.6 were only 390 and 331 respectively, which are significantly smaller that those observed in the ZnO devices.

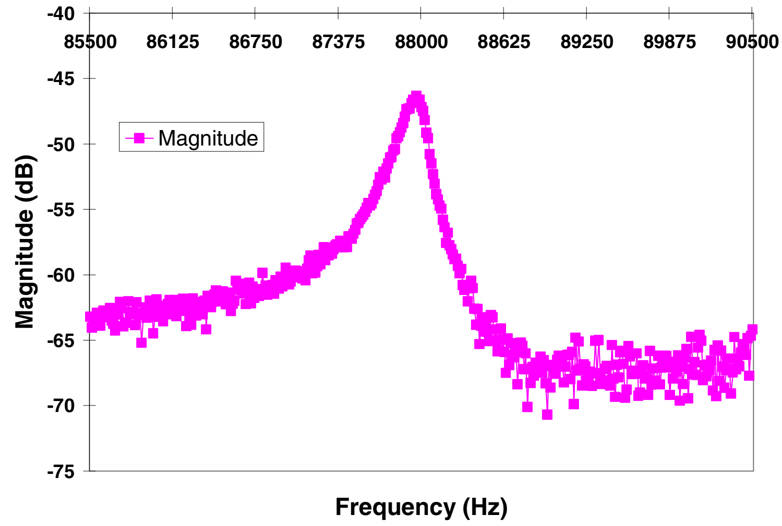

Figure 7.5 First resonant peak for generation I PZT clamped-clamped resonator.

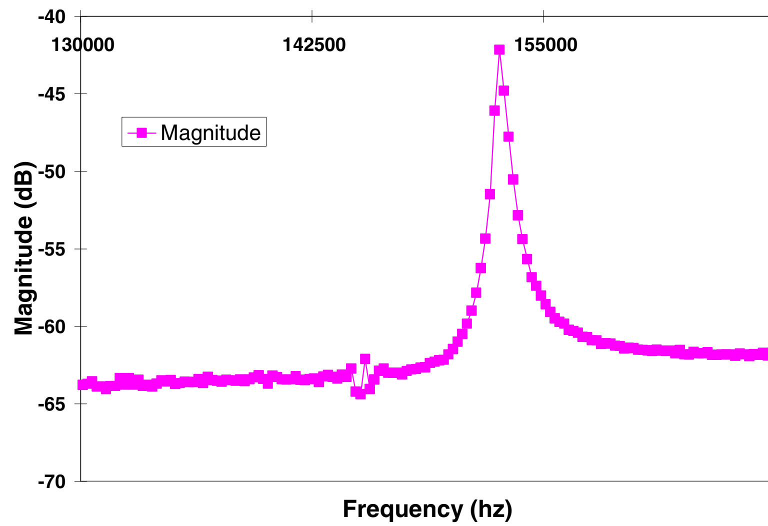

Figure 7.6 Second resonant peak for generation I PZT clamped-clamped resonator.

7.3 Generation I Resonator Mode Shape Analysis

Because these generation I resonators exhibited an obvious out-of-plane bow and their Qs were relatively low, their performance was not originally investigated in depth and work

was focused on modifying the stress gradient and producing the generation II resonators discussed in Chapter 8.

After acquisition of the LDV and optical profilometer test setup described in Chapter 4, development of the ANSYS models described in Chapter 6, and testing of the generation II resonators detailed in Chapter 8 was complete, these devices were reexamined using these updated techniques. Figure 7.7 shows the LDV velocity spectrum and the resonant peak frequencies for a 400 µm generation I resonator.

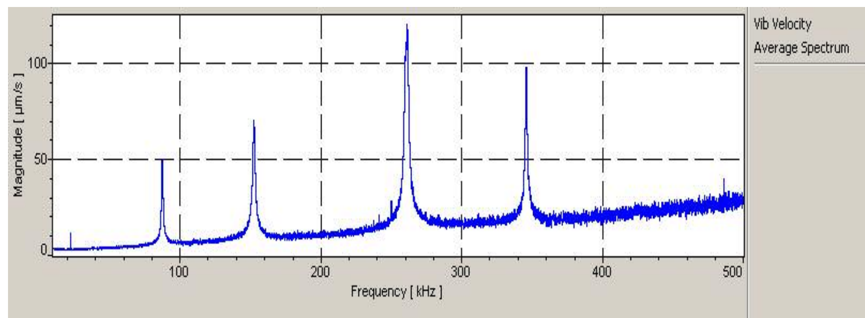

Figure 7.7 LDV velocity spectrum for a 400 µm generation I resonator.

The frequency peaks matched well with the original electrical measurements shown in Figure 7.6, but the measured mode shapes did not match the model predicted resonant frequencies or mode shapes. Figures 7.8 through 7.11 show the first four predicted mode shapes for a 400 µm resonator compared to the measured mode shapes measured by LDV for the first four peaks from Figure 7.7.

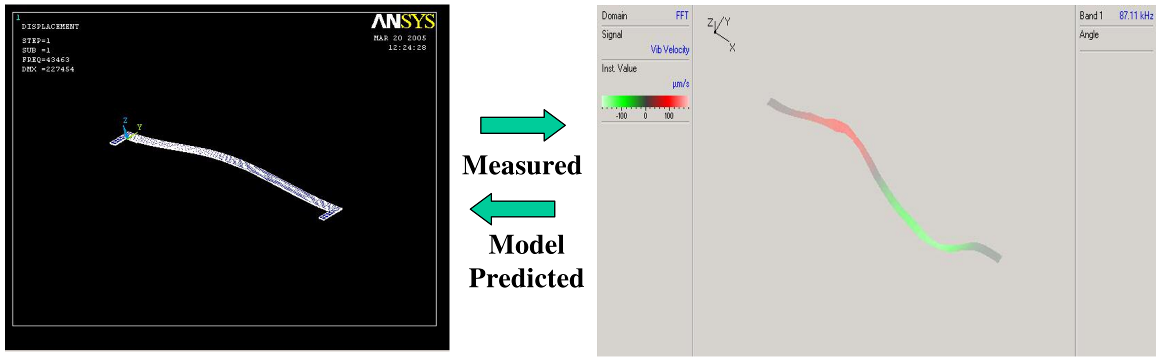

Figure 7.8 Predicted and measured first mode for a generation I resonator.

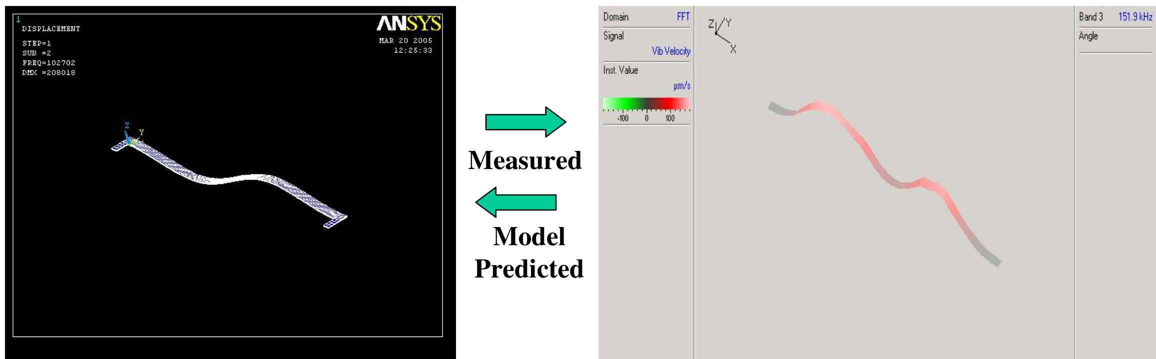

Figure 7.9 Predicted and measured second mode for a generation I resonator.

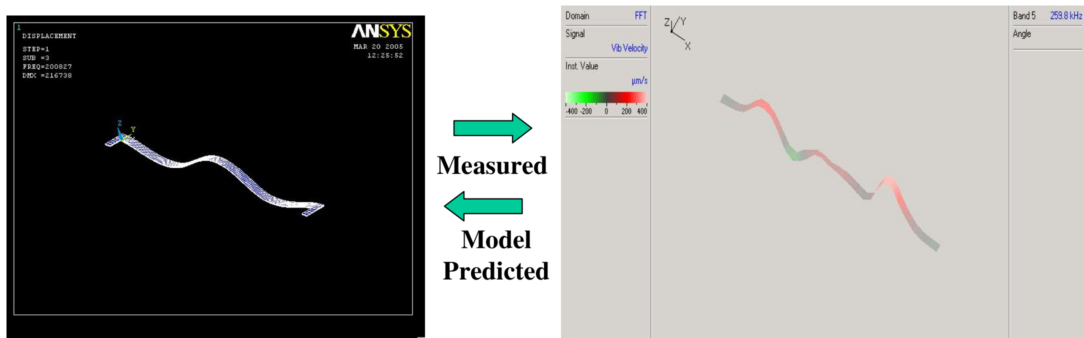

Figure 7.10 Predicted and measured third mode for a generation I resonator.

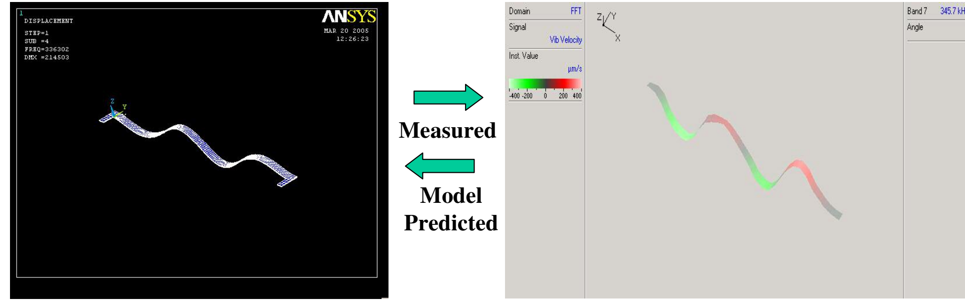

Figure 7.11 Predicted and measured fourth mode for a generation I resonator.

Table 7.2 shows a comparison of these resonant frequencies for each of the modeled and measured modes.

Table 7.2 Comparison of modeled and measured mode frequencies.

Mode	Unstressed Modeled frequency (KHz)	Measured Resonant Frequency (KHz)
Mode 1	43.4	87.11
Mode 2	102.7	151.9
Mode 3	200.9	259.8
Mode 4	336.3	345.7

An overall tensile stress in the resonators can shift the frequencies higher, as seen from equation (6.9) and the data in chapter 6. This was originally thought to be the case for these generation I resonators prior to taking the LDV measurements, which showed that the measured mode shapes did not match the predicted mode shapes. The cause for this discrepancy in frequencies is explained in Figure 7.1, which shows that the beams are severely bowed, and Figures 7.7 through 7.11, which show that the first measured mode shape matches the modeled second mode shape and that the frequencies are also relatively close. In addition, the measured fourth mode shape matches the modeled fourth

mode shape with close to the same frequency and the measured second and third mode shapes appear to be multimode responses that do not match frequencies with any of the modeled modes.

Several groups have shown that beam buckling can shift the first and third mode resonant frequencies higher for a clamped-clamped resonator while the second and fourth modes remain unaffected [69 - 72]. The following analysis follows that published by Nayfeh *et al*. [70]. The equation of motion for an undamped and unforced beam subjected to an axial load can be given by

$$m\frac{\partial^2 \hat{w}}{\partial \hat{w}^2}+EI\frac{\partial^4 \hat{w}}{\partial \hat{w}^4}+\left[P-\frac{EA}{2L}\int_0^L\left(\frac{\partial \hat{w}}{\partial \hat{w}}\right)^2 d\hat{x}\right]\frac{\partial^2 \hat{w}}{\partial \hat{x}^2}=0 \qquad (7.1)$$

where *m* is mass, *E* is Young's modulus, *I* is the moment of inertia, *w* is the transverse displacement, *x* is the distance along the beam, *A* is the cross-sectional area, *L* is the beam length, and *P* is the axial load. The critical Euler buckling loads and modes shapes can be defined as

$$EI\frac{d^4 \hat{w}}{d\hat{x}^4}+P\frac{d^2 \hat{w}}{d\hat{x}^2}=0. \qquad (7.2)$$

If *P* is increased beyond the nth buckling mode and the post buckling displacement is defined as $b\phi_n$ where *b* is a scaling constant and ϕ_n is the buckling mode shape, inserting these back into equation of motion gives

$$\left[P - P^n - \frac{EAb^2}{2L} \int_0^L \left(\frac{d\phi_n}{d\hat{x}} \right)^2 d\hat{x} \right] b \frac{d^2\phi_n}{d\hat{x}^2} = 0 . \quad (7.3)$$

The solution for b can then be derived from (7.3) as

$$b^2 = 2L \frac{\left[P - P^n \right]}{EA} \int_0^L \left(\frac{d\phi_n}{d\hat{x}^2} \right) = 0 . \quad (7.4)$$

To verify the buckling level, the buckled mode shape was measured with a Veeco optical profilometer as shown in Figures 7.12 and 7.13.

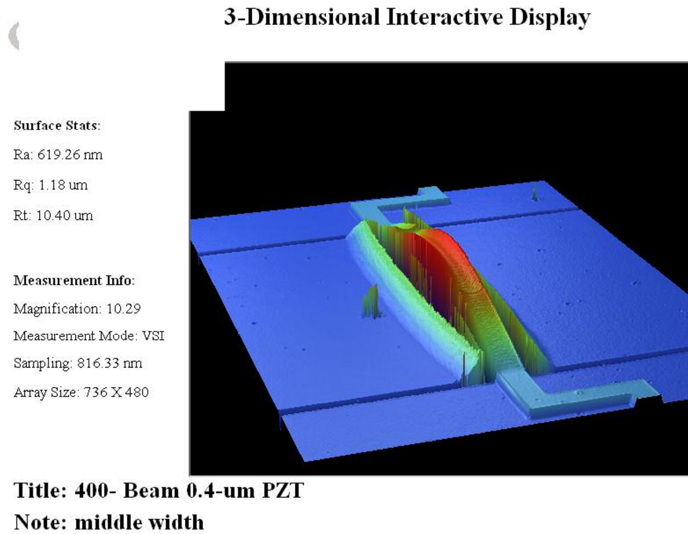

Figure 7.12 3-D view of measured buckled mode shape for 400 μm generation I resonator.

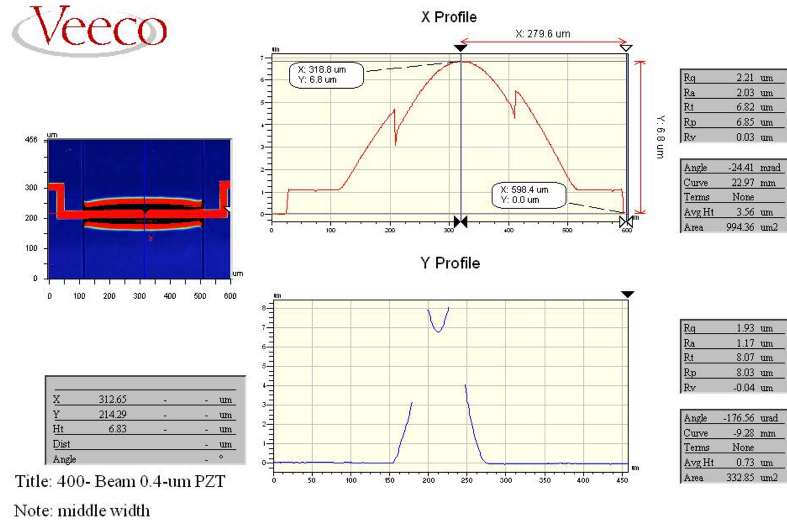

Figure 7.13 Cross section of measured optical profilometer data showing buckled mode shape.

From Figures 7.12 and 7.13, the data from the optical profilometer shows that the beam is exhibiting the first buckled mode shape. This buckled shape matches well with the beam deflections seen in the SEM images in Figure 7.1. With a maximum measured static deflection of 6.8 μm, a simple MATLAB program was written to solve for *b*, given the static midpoint deflection, and to plot the assumed first buckled mode shape given by

$$\phi_1 = 1 - \cos(2\pi x) \tag{7.5}$$

where x is given by $\hat{x}/L$ and the buckling load is given by

$$P^1 = \frac{4\pi EI}{L^2}\,. \tag{7.6}$$

Figure 7.14 shows the output of the MATLAB program, the modeled mode shape is very close to the actual measured mode shape shown in Figure 7.13.

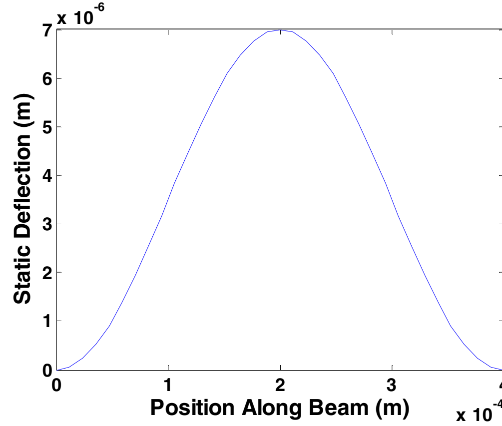

Figure 7.14 MATLAB modeled 1st buckled mode shape.

It is important to note that the displacements measured in the LDV were on the order of nanometers, whereas the static beam displacement was 6.8 μm, so that the resonance was definitely single sided and snap through did not occur. The beam response is then given by a sum of the static displacement and the resonance about that displacement

$$w(\hat{x},\hat{t}) = \hat{u}(\hat{x},\hat{t}) + b\phi_n\left(\hat{x}\right) \tag{7.7}$$

where $\hat{u}\left(\hat{x},\hat{t}\right)$ is the time-dependent displacement about the static position. The parameters in (7.1) can be nondimensionalized by taking $u = \frac{\hat{u}}{L}$ and $t = \sqrt{\frac{E}{m}}\hat{t}$.

If the solution is assumed to be

$$u\left(x,t\right) = \Phi\left(x\right)e^{i\omega t}, \tag{7.8}$$

the equation of motion can be written as

$$\frac{-m\omega^2 L^4}{EI}\Phi + \Phi'''' + \frac{P^n L^2}{EI}\Phi'' = \frac{Ab^2\int_o^1 \phi_n' \Phi' dx}{I}\phi_n'' \tag{7.9}$$

where Φ is the resonant mode shape and ω is the natural frequency. The mode shape is defined by a combination of the homogenius and particular solutions

$$\Phi(x,\omega) = \Phi_h(x,\omega) + \Phi_p(x,\omega) \tag{7.10}$$

where,

$$\Phi_h = C_1 \sin(\lambda_1 \hat{x}) + C_2 \sin(\lambda_1 \hat{x}) + C_3 \sinh(\lambda_2 \hat{x}) + C_4 \cosh(\lambda_2 \hat{x}), \tag{7.11}$$

$$\Phi_p = C_5 \cos(2\pi \hat{x}), \text{ and} \tag{7.12}$$

$$\lambda_1, \lambda_2 = \left\{ \pm \frac{P^n L^2}{2EI} + \frac{1}{2}\sqrt{\left[\frac{P^n L^2}{EI}\right]^2 + \frac{4m\omega^2 L^2}{EI}} \right\}^{\frac{1}{2}}. \tag{7.13}$$

When substituting (7.5), (7.6), and (7.10) through (7.12) into (7.9), the result is the following equation that describes the mode shape for the resonator.

$$\begin{aligned}\left(\frac{8Ab^2\pi^3}{I} - \frac{m\omega^2 L^4}{EI}\right)C_5 = \frac{8Ab^2\pi^3}{I}\left\{\lambda_1\left[\frac{2\pi\left(\cos\lambda_1 - 1\right)}{\lambda_1^2 - 4\pi^2}\right]C_1 - \lambda_1\left[\frac{2\pi\left(\sin\lambda_1 - 1\right)}{\lambda_1^2 - 4\pi^2}\right]C_2\right\} + \\ \frac{8Ab^2\pi^3}{I}\left\{\lambda_2\left[\frac{2\pi\left(1 - \cosh\lambda_1\right)}{\lambda_2^2 - 4\pi^2}\right]C_3 - \lambda_2\left[\frac{2\pi\sin\lambda_2}{\lambda_1^2 - 4\pi^2}\right]C_4\right\}\end{aligned} \tag{7.14}$$

Enforcing the clamped-clamped boundary conditions

$$\Phi = \Phi' = 0 \quad at \quad x = 0 \quad and \quad x = L, \tag{7.15}$$

on (7.11) results in a series of four equations and four unknowns (C_1 through C_4). If C_5=0 these four equations can be used to determine the natural frequencies and mode shape for the resonator. These will not be dependent on the amount of initial buckling in the beam.

If $C5 \neq 0$ then equation (7.14) is used to give five equations and along with (7.13) five unknowns. These five equations can then be used to find the eiganvalues that are dependent on the initial buckled condition. This set of equations can be solved numerically as has been done by others and the solution of the nondimensional frequency versus the nondimensional buckling level for the first four modes is plotted in Figure 7.15 as given by Nayfeh *et al.* [70].

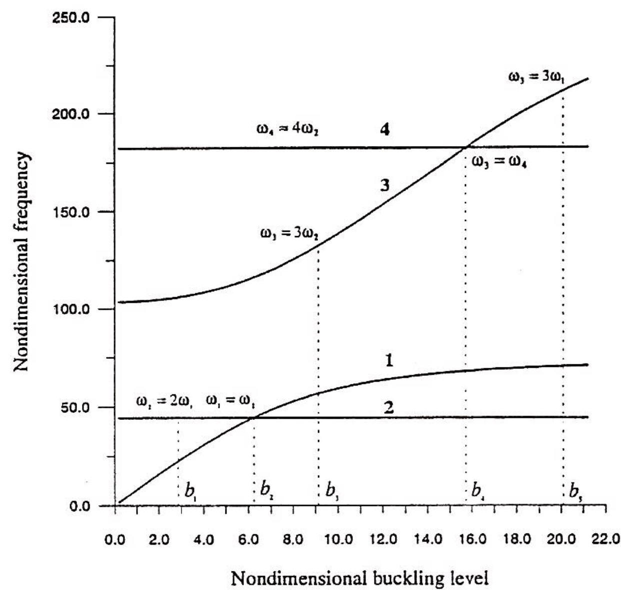

Figure 7.15 Nondimensional solution for resonant frequency versus buckling level for a buckled clamped-clamped beam.

The data from Figures 7.7 through 7.11 definitely falls between the nondimensional buckling level of 6 and 16 from Figure 7.15 since the first peak in Figure 7.7 is the second resonant mode and the fourth peak is the fourth resonant mode, while the second and third peaks are mixed modes. The predicted resonant frequencies from Figure 7.15 for each mode of the 400 μm resonator were calculated by taking a nondimensional buckling level of 7 and using the material properties derived in Chapter 5. Table 7.3 shows a comparison of these predicted values to the actual measured resonant frequencies.

Table 7.3 Measured and predicted resonant frequencies for buckled generation I resonator.

	Measured	Predicted for b=7
Mode 1	87	89
Mode 2	151	97
Mode 3	259	232
Mode 4	345	353

Mode one and four matched reasonably well while modes three and especially mode four varied significantly. One reason for the discrepancy could come from the fact that this was a generation I resonator, which was one of the first resonators fabricated and used the original process flow that did not include all of the current material annealing steps. This more than likely resulted in material properties that are significantly different from those measured in the course of this work. Another source of error could come from the fact that the derivation presented here is based on a uniform beam along the length whereas the PZT resonator is made of three sections as defined by the presence or absence of the top electrode. Derivation of the piecewise problem has been explored by Li *et al*. [73].

As further confirmation that the resonators on this wafer were indeed truly buckled, a few resonators where found that were buckled down on the same wafer as the buckled up ones described above. Figure 7.16 shows the Veeco optical profilometer data from a buckled down beam.

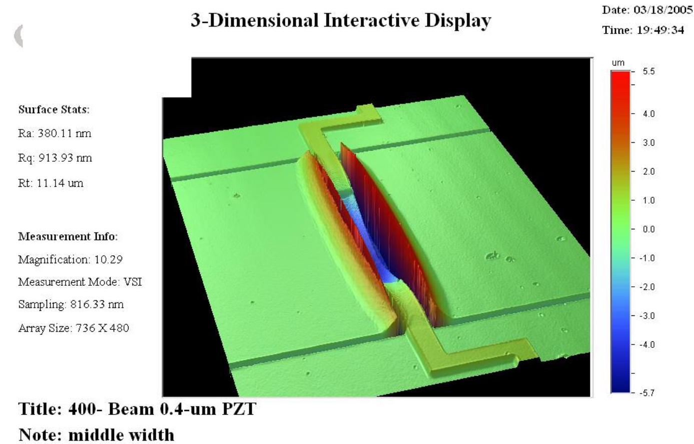

Figure 7.16 Measured buckled-down mode shape for 400 μm generation I resonator from same wafer as device measured and reported in Figures 7.12 and 7.13.

Because the generation I resonators exhibited buckling, the traditional bending mode was not available for direct comparison to the ZnO clamped-clamped beam resonators reported by DeVoe and the generation I resonators were not studied in depth. On the other hand, even with the buckled beam behavior the generation I resonators showed significantly higher resonator admittance than their ZnO counterparts lending support to the predictions from Chapter 2. The motivation for the generation II resonators discussed in Chapter 8 was to eliminate the buckling behavior seen in the generation I devices to enable a better comparison to the ZnO resonators and to increase the resonant frequency beyond the approximately 1MHz frequency demonstrated by the ZnO devices.

Chapter 8. Stress Modified Resonators

8.1 Generation II Resonator Design and Fabrication

A new mask set was made for the generation II resonators and the initial thicknesses of the Ti, Pt and PZT layers were again selected based on the standard process at ARL for PZT thin films as shown in Table 8.1 for generation II wafers W11 and W12.

Table 8.1 Initial film thickness for generation II resonators.

Material	Mat'l Thickness wafer W11 (µm)	Mat'l Thickness wafer W12 (µm)
SiO_2	1.0	2.0
Ti	0.02	0.02
Bottom Pt	0.17	0.17
PZT	0.5	0.5
Top Platinum	0.17	0.17

Control of the residual stresses in the PZT stack is critical for making planar suspended devices for any MEMS application and residual stress in the PZT films have been studied by several researchers at ARL [59, 60, 74]. By using wafer bow measurements, the stress in each material layer of the PZT stack was analyzed, as well as the stress state of the overall stack. From these studies, thin-film RTA anneal processes were added after the SiO_2 and bottom Pt deposition steps to modify the overall resonator stress state. Tables 8.2 and 8.3 show the typical stress state from the modified process that includes anneals of both the bottom SiO_2 and Pt layers [59]. The typical average PZT stack stress is approximately 100 to 200 MPa tensile.

Table 8.2 Typical residual stress in each individual layer.

Layer	Avg. Stress (MPa)	Std. Dev.
SiO_2	-341	7
RTA SiO_2 (700°C/60sec in N_2)	47	7
Ta/Pt	-284	79
RTA Ta/Pt (700°C/60sec)	858	28
0.22 μm PZT	144	22
0.44 μm PZT	148	21
0.66 μm PZT	132	27
0.88 μm PZT	113	32
Pt	-113	26.
RTA Pt (350°C/120sec)	-15	37

Table 8.3 Typical cumulative residual stress in PZT stack.

Layer	**Avg. Stress (MPa)**	**Std. Dev.**
SiO_2	-341	7
RTA SiO_2 (700°C/60sec in N_2)	47	7
Ta/Pt	-23	14
RTA Ta/Pt (700°C/60sec)	219	6
0.22 mm PZT	204	7
0.44 mm PZT	196	9
0.66 mm PZT	181	14
0.88 mm PZT	165	18
Pt	163	4
RTA Pt (350°C/120sec)	175	6

Figure 8.1 shows a SEM micrograph of a 400 μm long resonator from wafer W4 that was fabricated using the updated process. These beams did not exhibit any of the observed buckling seen in the generation I resonators.

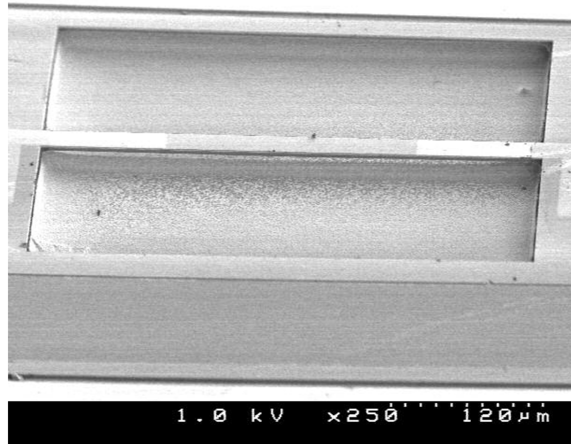

Figure 8.1 400 μm released clamped-clamped resonator from wafer W4.

In addition to the new anneal steps, isolation trenches were added around each structure to minimize feed-through capacitance, several different bond pad sizes were added to study their capacitive effect on electrical testing, beam lengths down to 25 μm were added to increase the resonant frequency, and the release process was changed to use the topside release process described in Chapter 3 and seen in Figure 8.1.

8.2 Generation II Resonator Performance

Figures 8.2 through 8.5 show the electrical response of a 400 μm and 200 μm long resonator from wafer W11 and W12.

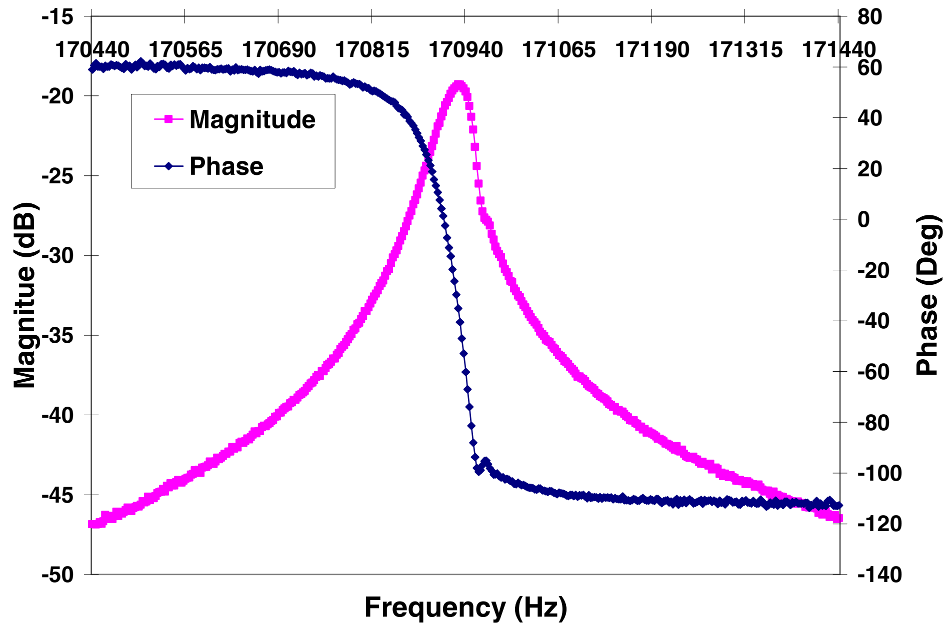

Figure 8.2 Magnitude and phase response for a 400 μm resonator from W11.

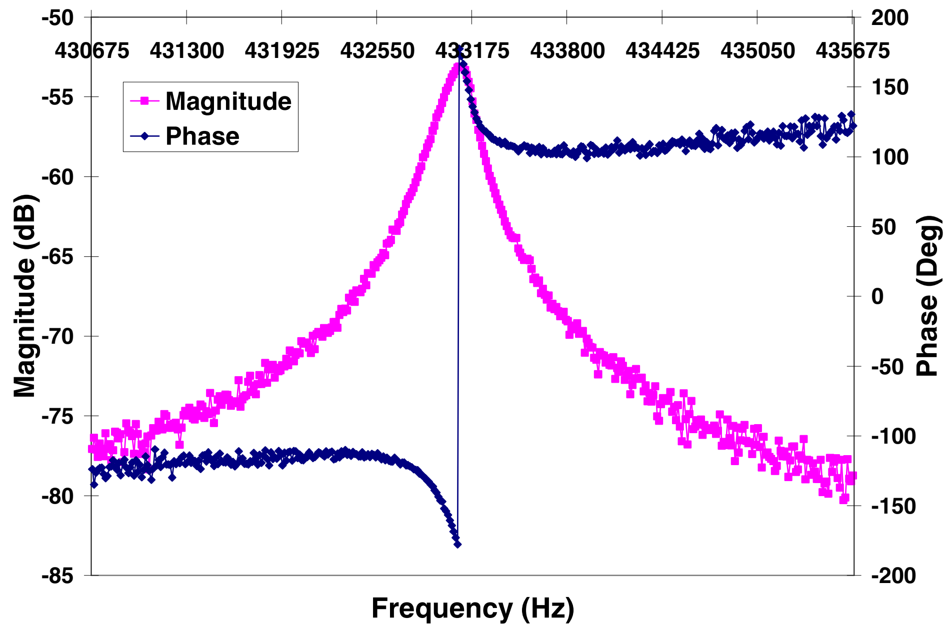

Figure 8.3 Magnitude and phase response for a 200 μm resonator from W11.

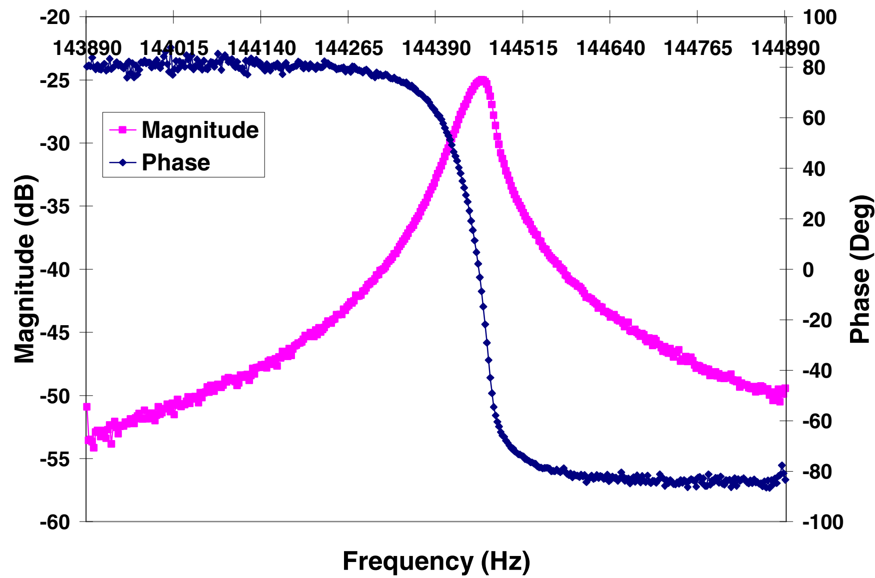

Figure 8.4 Magnitude and phase response for a 400 μm resonator from W12.

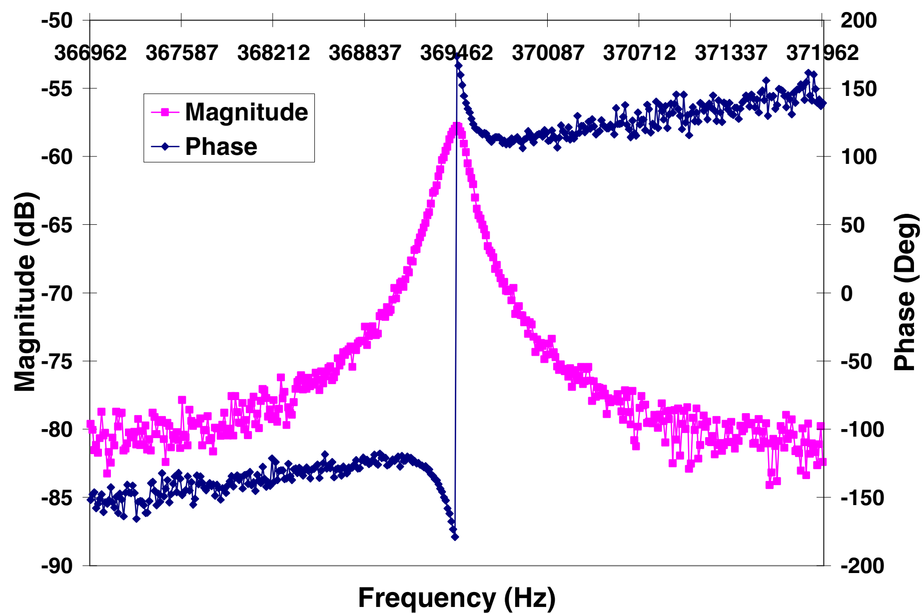

Figure 8.5 Magnitude and phase response for a 200 μm resonator from W12.

Compared to the ZnO resonators discussed in section 7.2, the PZT resonators again displayed more prominent resonant peaks with signal-to-noise levels of greater than 25 dB for 400 μm long resonators compared to the 2 to 4 dB seen in the ZnO resonators. The resonant frequencies where about the same in the 400 μm resonators (142 kHz to 170 kHz compared 158 kHz) but significantly lower for the 200 μm beam resonators (370 kHz to 434 kHz compared to 839 kHz). The PZT resonators exhibited 180 degrees of phase shift at resonance versus the 13 to 58 degrees seen in the ZnO resonators. A unity gain op-amp was used on the 400 μm resonators but not on the 200 μm devices, hence the difference in phase at resonance (see discussion in section 4.2.2). The Qs of the initial resonators from the data in Figures 8.2 through 8.5 were in the range of 2890 to 3418 for the 400 μm resonators and 1770 to 2100 for the 200 μm resonators, much higher than that seen in the generation I PZT resonators and similar to the calculated values of 3700 and 1580 for the ZnO resonators. These values are still lower than those seen with electrostatic clamped-clamped beam devices, up to 8000, over the same frequency range. With the Qs on the same level as the ZnO resonators previously reported, the larger and more distinguished resonant peaks in Figures 8.2 through 8.5 compared to those for ZnO can be related back to the increase in the piezoelectric coefficient of PZT versus ZnO and the increase in resonator admittance as expected from Equation 2.32 in Chapter 2.

Resonators from wafer W11 were also tested at lengths of 100, 80, 50, and 25 μm to examine the resonator performance at higher resonant frequencies. The resulting resonance frequencies were 1.35 MHz, 1.82 MHz, 3.6 MHz, and 9.2 MHz respectively. Figure 8.6 shows data for the 25 μm resonator.

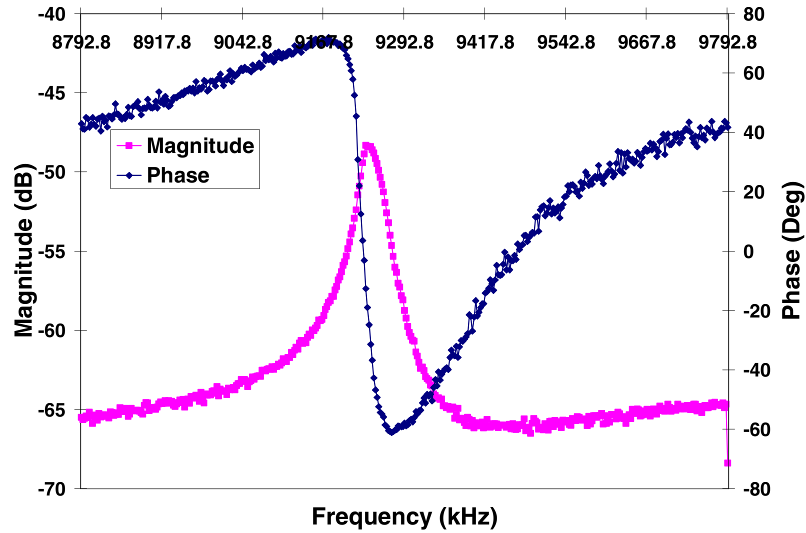

Figure 8.6 Magnitude and phase response for a 25 μm resonator from W11.

A large signal, approximately 17 dB, was still obtained but the Q dropped down to 335. The loaded Qs for wafer W11 are plotted in Figure 8.7. The air loaded Qs for the resonator are not plotted but ranged from 300 to 500 over the frequency range tested.

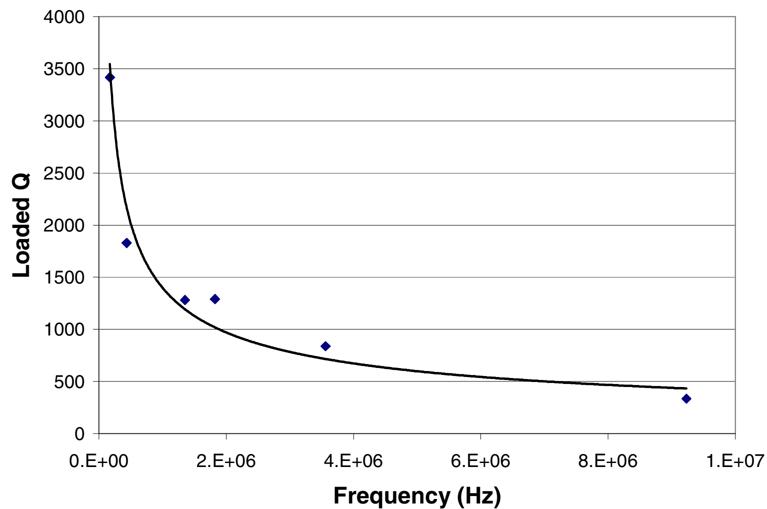

Figure 8.7 Loaded Qs for resonators from wafer W11.

In addition to the basic electrical measurements, the generation II resonators were further examined to look at how they would be affected in real applications by initial poling conditions, operating temperature, operating pressure, and driving voltage.

8.3 Generation II Resonator Poling

As stated in Chapter 2, PZT is a ferroelectric material that requires poling in order to exhibit piezoelectric properties. This poling process changes the lattice constants of the PZT and the overall stress state of the material. As seen in Chapter 6, residual stress can affect the frequency of the resonators. The PZT films in the as-deposited state did not exhibit any piezoelectric properties. Upon processing the resonators, positively biased piezoelectric responses were observed. Figure 8.8 shows the frequency response for a 200 μm resonator from wafer W11 as processed without any poling. Subsequently, the same device was poled for by first applying a positive 3.5 volt bias for 20 minutes followed by a negative 3.5 volt bias for 10 minutes, and then a negative 3.5 volts for another 15 minutes. The frequency response was measured after each poling condition and is plotted along with the unpoled condition in Figure 8.8. The data shows that the as-processed films are positively poled and that an applied negative bias initially decreases the resonance frequency and magnitude of the response. In fact in some cases it was possible to reverse the polarity to a point where no response was seen. With the continued application of a negative bias the magnitude of the response and the frequency are increased back towards that observed via a positively biased film. This is because the film becomes polarized 180º in the opposite direction and for an applied RF electric field the resulting strain and response in the beam structure are the same. Further investigation is required but it is believed that the initially positively poled as-processed PZT film

condition arises from the RF fields generated during plasma etching as reported elsewhere by Brooks *et al*. [21].

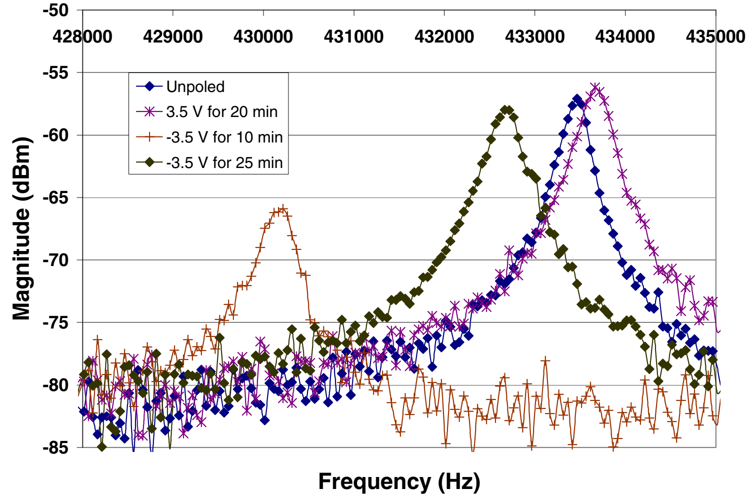

Figure 8.8 Effect of poling condition on resonant frequency for a 200 µm resonator.

The same effect with similar results is shown in Figure 8.9 for an 80 µm resonator from wafer W12.

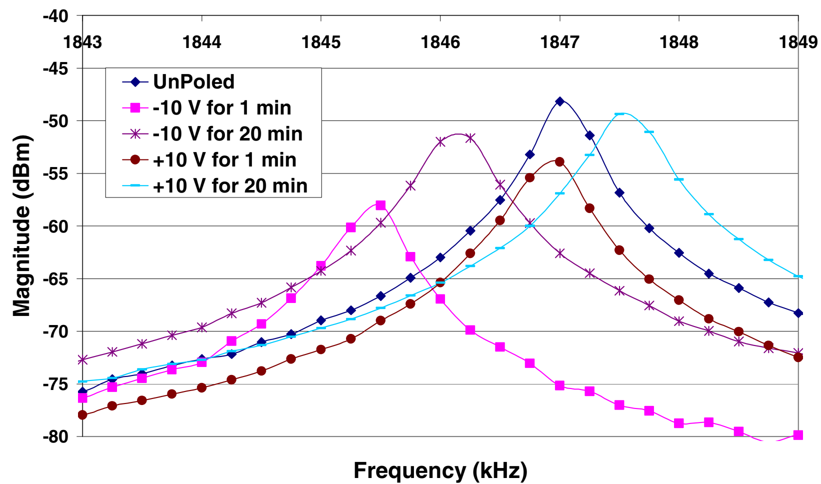

Figure 8.9 Effect of poling condition on the resonant frequency of a 80 µm resonator.

The maximum fractional frequency shift caused by a variation in the poling condition, $\Delta f / f$, for the 200 and 80 μm resonators is 7960 ppm and 1082 ppm, respectively. This means the effect of the poling condition on the resonant frequency is greater than the effect of temperature over a 100º C range as seen in the next section. The larger effect occurs on the longer resonator because, as shown in Chapter 6, lower frequencies and hence longer resonators are more affected on a percentage basis by residual stress. The thermal model developed in Chapter 6 was used on a 200 μm resonator from wafer W11 to determine the effective change in residual stress caused by the changing poling conditions. By varying the false CTE of only the PZT layer in the model to match the frequency shift observed in Figure 8.8 and noting the change in the modeled residual stress, it was determined that poling the film could induce a 13 MPa change in the stress state of the PZT film. Table 8.4 shows the high and low modeled stress range in the PZT film layer at the two frequency extremes for the data in Figure 8.8.

Table 8.4 Modeled PZT stress vs. PZT poling condition.

Poled State	Frequency (Hz)	Modeled PZT Layer Stress (MPa)
Low Poled State	430058	155-236 MPa
High Poled State	433995	169-249 MPa

This ostensibly negative effect can potentially be used to tune the resonator frequency in the lower frequency ranges by varying the stress state in the PZT films. It has been reported that poling at above 150°C or poling while exposed to UV light can fix a given polarization state [75]. The drawback would be larger loss and lower resonator admittance from using a resonator off its optimized polarization state. ZnO is a

pyroelectric film and therefore does not require poling which could be an advantage in stability and repeatability of the frequency response but a disadvantage in the ability to tune the resonant frequency.

8.4 Generation II Resonator Thermal Stability

Thermal stability is a critical parameter if MEMS resonators are to replace more standardized technologies like Quartz and SAW resonators. The temperature dependence of the generation II PZT resonators were measured by varying the operating temperature from 300 K to 400 K under vacuum and testing them electrically on the vacuum probe station hot plate. The variation in resonant frequency over the 100 K temperature span is shown in Figures 8.10 and 8.11 for a 200 μm and a 100 μm long resonator from wafer W11. The fractional frequency change $\Delta f/f$ versus temperature is plotted in Figure 8.12.

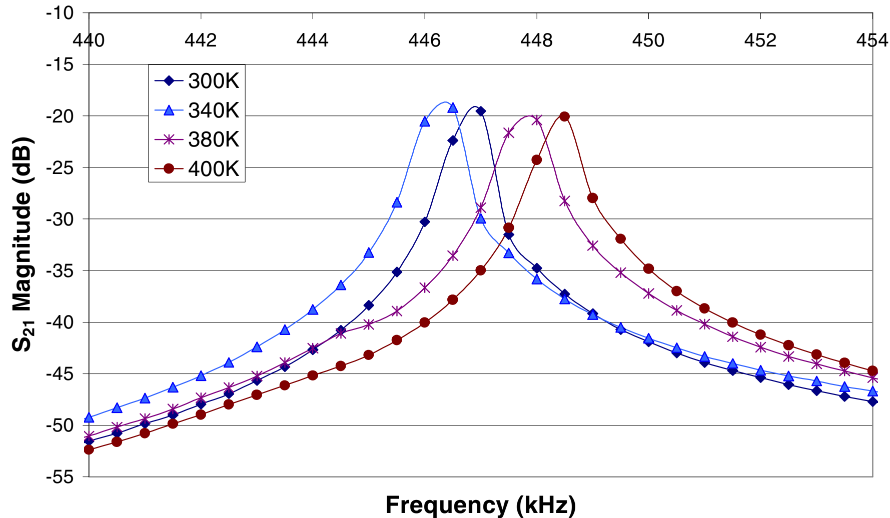

Figure 8.10 Temperature stability of a 200 μm resonator from W11.

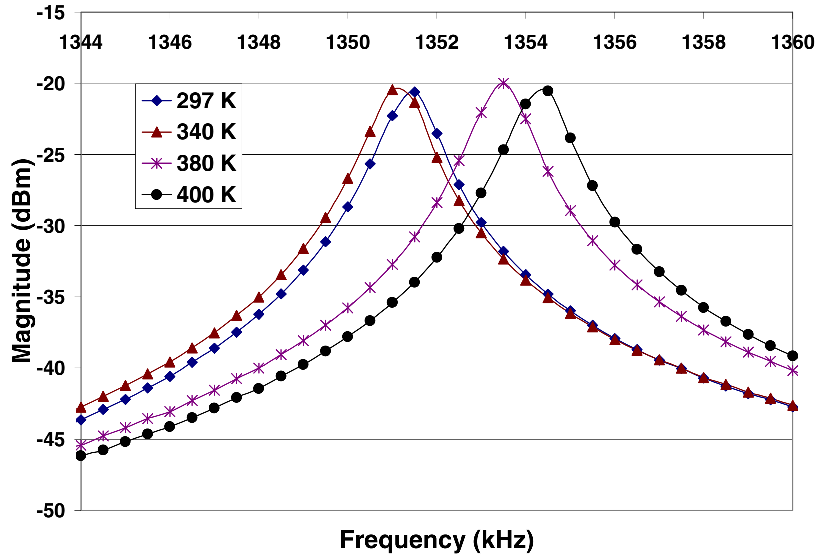

Figure 8.11 Temperature stability of a 100 μm resonator from W11.

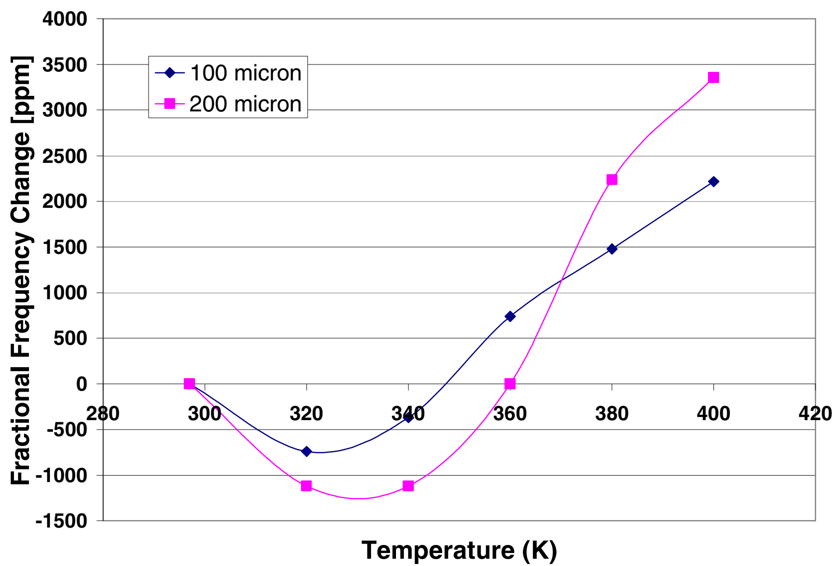

Figure 8.12 Fractional frequency change from Figures 8.10 and 8.11.

For the generation II PZT resonators, the frequency initially decreases until 320 K is reached and then increases until 400 K. The ZnO resonators were not tested thermally so a comparison cannot be made to them but this trend differs from frequency vs. temperature plots reported for non-temperature compensated electrostatic clamped-clamped and comb drive resonators which continually decrease in frequency with

increasing temperature [34,76-78]. For the electrostatic resonators, the substrate and resonator materials generally have very similar CTEs, and the reduction in frequency with temperature is generally attributed to a decrease in the Young's modulus of the resonator material with temperature. The magnitudes of the temperature dependency are also much less for reported electrostatic devices with changes in fractional frequency of around negative 16 ppm. With stress and electrical bias thermal compensation, electrostatic resonators have been demonstrated with near zero changes in fractional frequency over the same temperature range [77].

From Chapters 5 and 6, the PZT stack is made of materials with significantly different Young's modulus, CTE and residual stress values from the silicon substrate. The large variation in the CTE values has a significant effect on the residual stress gradient within the PZT stack as shown in Table 6.6. This modification of the stress gradient drives the large temperature response seen in Figures 8.10 and 8.11. Future designs will need to incorporate stress/temperature compensating materials or stress relief designs in order to reduce the temperature effects to an acceptable level.

8.5 Generation II Resonator Linear Response Analysis

Figure 8.13 shows the effect of vacuum pressure on an 80 μm resonator from wafer W11. As the device is brought under vacuum, the Q and magnitude of the resonant peak increase until about 1 to 10 Torr is reached and then no further increase is observed through 20 mTorr. This data shows that the resonators work well in air but that a vacuum of less than 1 Torr is required to minimize damping and optimize performance.

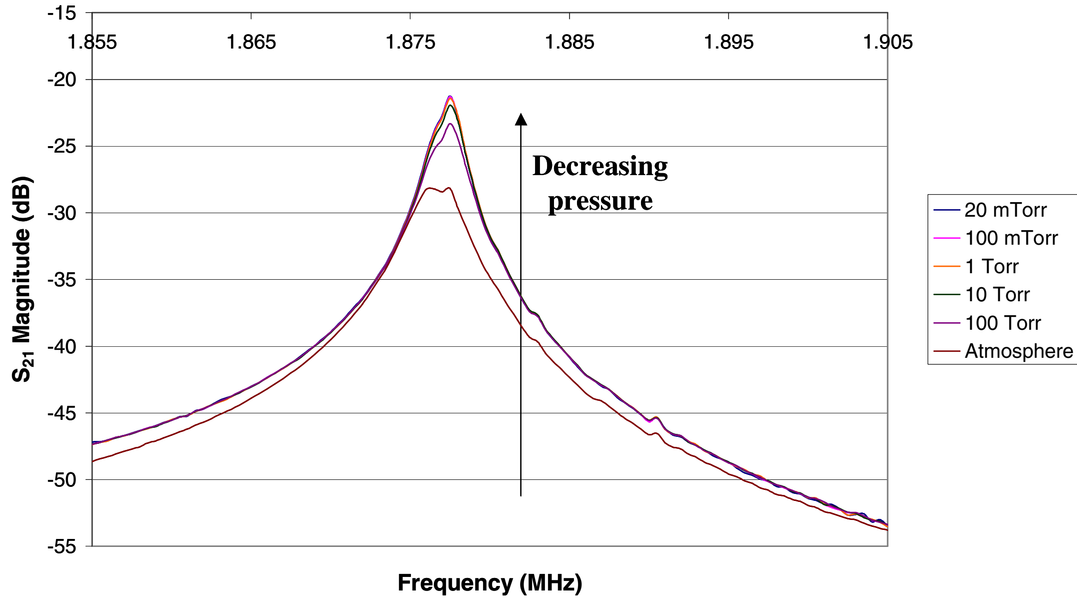

Figure 8.13 Effect of pressure on resonator Q.

From this, it is very clear that squeeze-film damping can play a significant role in the resonator performance. Squeeze-film damping refers to the energy that is dissipated as air is displaced from under the beam as the beam moves vertically and can be given by

$$\lambda_{sf} = \frac{\mu L b^3}{d^3} \tag{8.1}$$

where μ is the air viscosity and d is the beam to substrate gap. For linear vibrations the equation of motion can be given by

$$m\frac{d^2x}{dt^2} + c\frac{dx}{dt} + kx = F\cos(\omega t), \tag{8.2}$$

$$\frac{d^2x}{dt^2} + \frac{c}{m}\frac{dx}{dt} + \frac{k}{m}x = F\cos(\omega t), \text{ or} \tag{8.3}$$

$$\frac{d^2x}{dt^2} + 2\zeta\omega_n \frac{dx}{dt} + \omega_0^2 x = \frac{F}{m}\cos(\omega t) \tag{8.4}$$

where ζ is the viscous damping factor, λ is the linear damping coefficient, and ω_n is the natural frequency of undamped oscillation. The frequency response to the above is given as

$$G(i\omega) = \frac{1}{\left[\left(1-\left(\omega/\omega_n\right)^2\right)^2 + \left(2\zeta\,\omega/\omega_n\right)^2\right]^{1/2}}. \tag{8.5}$$

For small values of ζ the maximum response occurs near $\omega/\omega_n=1$ and the maximum value of $G(i\omega)$ is defined as the quality factor Q and for small values of ζ,

$$Q \approx \frac{1}{2\zeta}. \tag{8.6}$$

The difference in frequency between the half-amplitude points on either side of Q are considered to be the bandwidth of the system and

$$Q \approx \frac{1}{2\zeta} \approx \frac{\omega_n}{\omega_2 - \omega_1}. \tag{8.7}$$

Therefore, the dampening λ coefficient can be given by

$$\lambda = \frac{c}{2m} = \frac{\omega_n}{2Q} = 2\pi\omega_n \frac{(\omega_{3dB+} - \omega_{3dB-})}{2\omega_n} = \pi(\omega_{3dB+} - \omega_{3dB-}). \tag{8.8}$$

A plot of the linear dampening coefficient versus frequency is plotted in Figure 8.14 for a clamped-clamped beam resonator by measuring the 3dB bandwidth at the resonant frequency [79]. The change in the damping coefficient is clear as the pressure is lowered with the elimination of the any air dampening below approximately 10 torr. The damping below 10 torr can be attributed to the intrinsic damping on the PZT resonator structure and that from atmosphere down to 10 torr to the squeeze film damping from air beneath the resonator. The damping coefficient for the same resonator is plotted versus frequency in Figure 8.15.

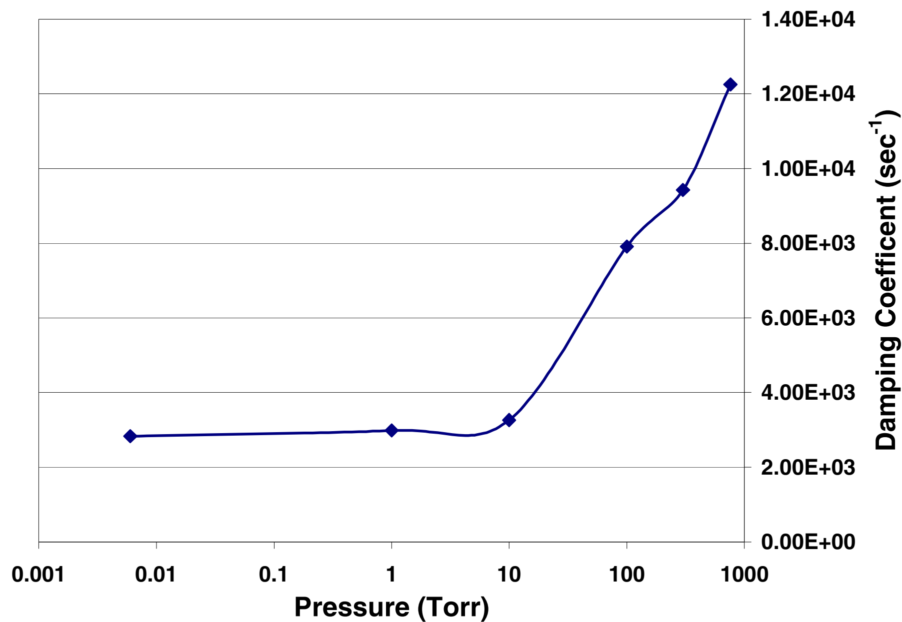

Figure 8.14 Plot of the linear dampening coefficient vs. pressure.

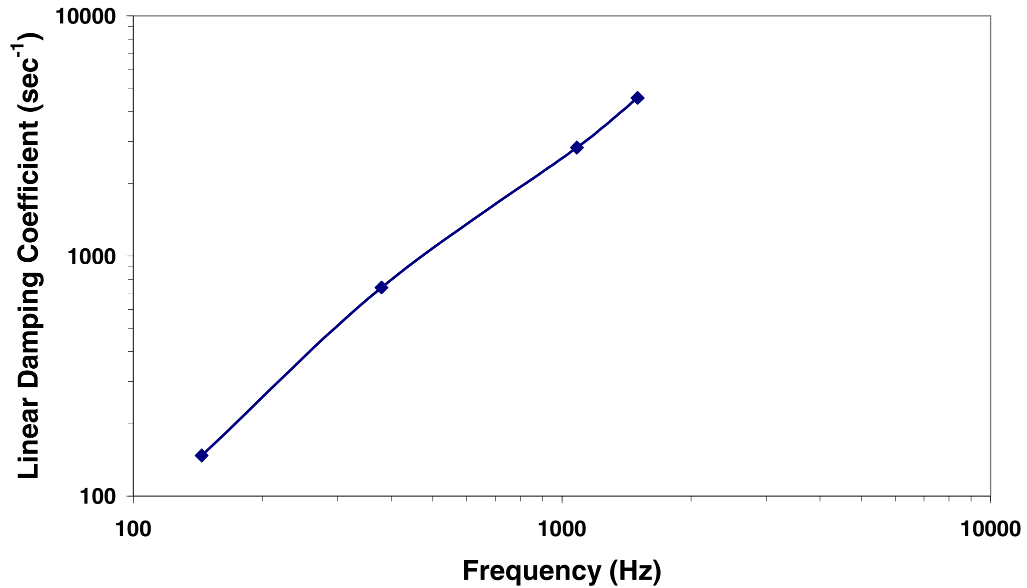

Figure 8.15 Plot of the linear damping coefficient vs. frequency.

Likewise, the linear spring coefficient for the PZT resonators can be determined from

$$\frac{k}{m} = \omega^2 - or - k = m\omega^2 . \tag{8.9}$$

For the 80 μm resonator being used for this development, the linear spring coefficient was 2317 N/m^2. The values for k and ζ can be put back into the equation of motion for the clamped-clamped beam driven by an actuation force F described above. A comparison of the theoretical, as plotted by a MATLAB routine, and measured resonant curves is shown in Figures 8.16 and 8.17 for the 80 μm resonator from wafer W11.

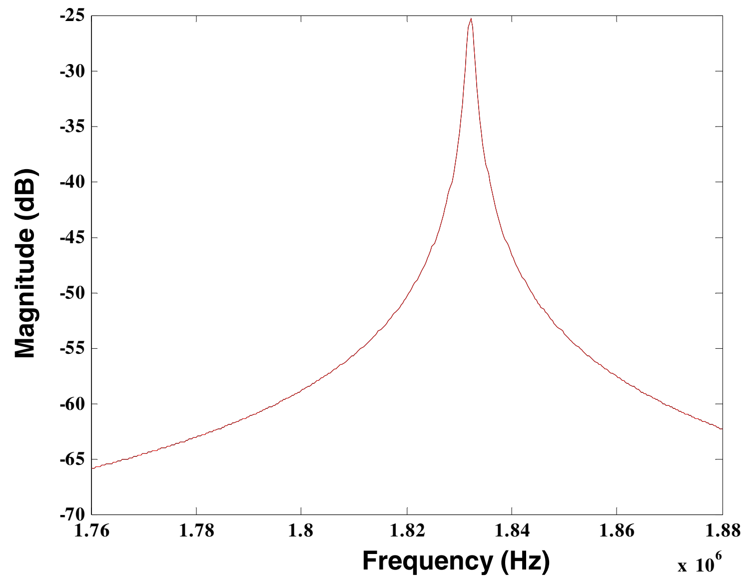

Figure 8.16 Calculated response based on measured values for damping and spring coefficients.

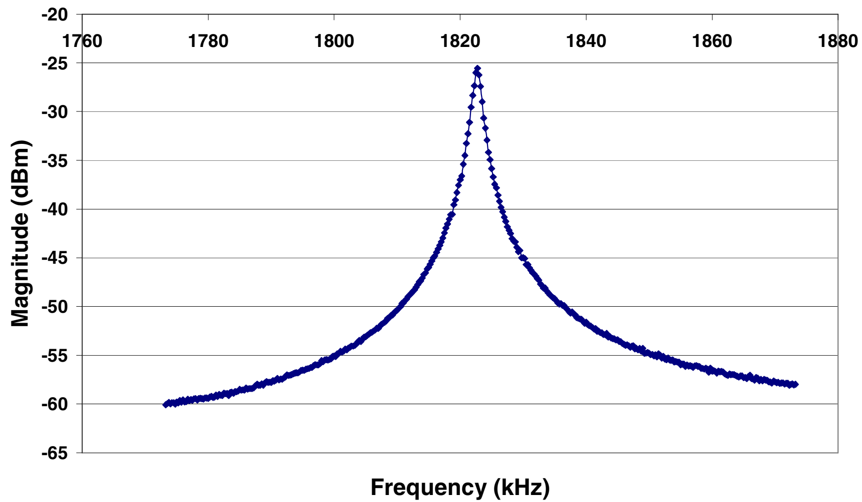

Figure 8.17 Measured response for 80 μm resonator from wafer W11.

The measured data matches well with the theory based prediction based on the calculated damping and spring coefficients and indicates that the resonators are truly operating in a linear regime for the response seen in Figure 8.17.

8.6 Generation II Resonator Nonlinear Response Analysis

In Figures 8.2 and 8.4, a slight asymmetry can be seen in the resonance peak. This is the result of the onset of Duffing behavior caused by an increased input drive voltage. As discussed in Chapter 1, power handling is a current hurdle to the implementation of practical MEMS resonators. This applies to PZT based MEMS resonators as well. Duffing behavior is the result of beam stiffening and can be represented by adding a nonlinear cubic spring constant to the equation of motion given in the last section

$$\frac{d^2x}{dt^2} + 2\lambda \frac{dx}{dt} + \omega_o^2 x + \beta x^3 = \frac{F_{ac}}{m}\cos(\omega t). \tag{8.10}$$

Understanding what effect Duffing behavior in the PZT resonators is critical to maximizing the dynamic range and power handling of the resonators. Dynamic range for the same 80 μm resonator shown in Figure 8.17 for the linear response was measured by varying the drive voltage from 2.5 mV to 0.8 V and sweeping the frequency in both the upward and downward directions. The results are presented in Figure 8.18.

The analysis to follow was performed to study and verify the Duffing behavior response seen in Figure 8.18. The analysis in this section follows that presented by Ayela *et al.* who developed the anharmonic response for a micromachined silicon resonator and by Robert Young who developed the equations within this section that apply the theory discussed by Ayela to the PZT resonators studied for this research. [79, 80].

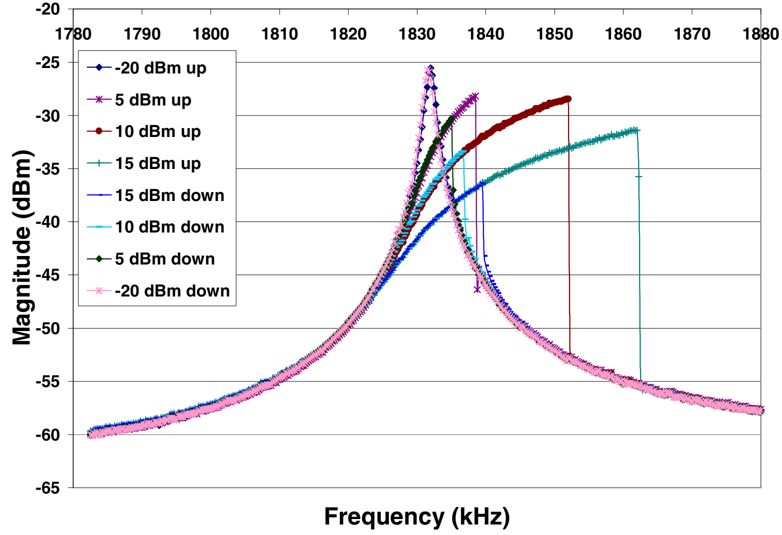

Figure 8.18 Duffing behavior as a function of drive voltage and sweep direction.

If A_{in} is taken as the input drive amplitude the equation of motion can be nondimensionalized by making

$$G = \frac{x}{A_{in}}. \tag{8.11}$$

Therefore,

$$\frac{d^2G}{dt^2} + 2\lambda \frac{dG}{dt} + \omega_o^2 G + \beta A_{in}^2 x^3 = \frac{F_{ac}}{mA_{in}} \cos(\omega t). \tag{8.12}$$

If $\tau = \omega_0 t$ then

$$\frac{d^2G}{d\tau^2} + \frac{2\lambda}{\omega_0^2}\frac{dG}{d\tau} + G + \frac{\beta A_{in}}{\omega_0^2} x^3 = \frac{F_{ac}}{kA_{in}} \cos\left(\frac{\omega}{\omega_0}\tau\right). \tag{8.13}$$

The driving force is assumed to be proportional to the input voltage based on equation (2.11) and therefore, A_{in} is assumed to be proportional to the square root of the average drive input power or

$$A_{in} = C_{NLP}\sqrt{P_{ave}} \tag{8.14}$$

$$\text{and } F_{ac} = C_{FP}\sqrt{P_{ave}}\ . \tag{8.15}$$

Then the equation of motion becomes

$$\frac{d^2G}{d\tau^2} + \frac{2\lambda}{\omega_0}\frac{dG}{d\tau} + G + \frac{\beta C_{NLP}^2 P_{ave}}{\omega_0^2}x^3 = \frac{C_{FP}}{kC_{NLP}}\cos\left(\frac{\omega}{\omega_0}\tau\right). \tag{8.16}$$

Then from Ayela, the frequency shift from spring stiffening during a sweep up or a sweep down in frequency is given by

$$\Delta f = \frac{1}{2\pi}\frac{X\Gamma}{\lambda^2} \text{ for up sweep} \tag{8.17}$$

$$\text{or } \partial f = \left(\frac{27X\Gamma}{4}\right)^{1/3} \text{ for a downward sweep.} \tag{8.18}$$

By eliminating XΓ the damping coefficient λ can be defined as

$$\lambda = \sqrt{\frac{\left(2\pi\partial f_{down}\right)^3}{\frac{27}{4}2\pi\Delta f_{up}}}\ . \tag{8.19}$$

By measuring the shift in frequency for both the upward and downward data from Figure 8.18, the nonlinear damping coefficient as a function of input power can be calculated as shown in Figure 8.19 for the 80 µm resonator from wafer W11.

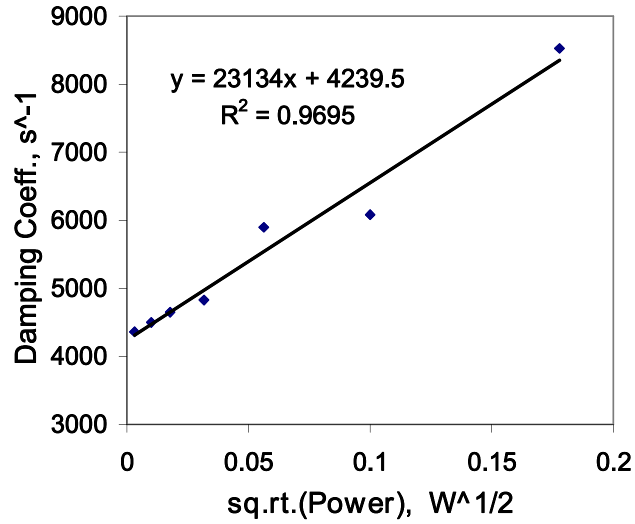

Figure 8.19 Calculated nonlinear damping coefficient.

For the nonlinear spring coefficient, we can again start with terms from Ayela

$$2\pi\Delta f_{up} = \frac{X\Gamma}{\lambda^2} = \frac{3\beta}{8\omega_0}\frac{\Gamma}{\lambda^2} \tag{8.20}$$

and

$$A_{Mup} = \frac{\sqrt{\Gamma}}{\lambda}. \tag{8.21}$$

The S_{21} parameter, or measured resonator electrical response, can be related to A_{Mup} by

$$S_{21Mup} = 20\log\left(\frac{A_{Mup}}{A_{in}}\right), \tag{8.22}$$

then combining to get a function for the nonlinear spring coefficient

$$\beta A_{in}^2 = \frac{8\omega_0}{3} 2\pi\Delta f_{up} 10^{\left(-2S_{21Mup}/20\right)}, \text{ and} \tag{8.23}$$

$$\beta A_{in}^2 = \beta C_{NLP}^2 P_{ave} = \beta' P_{ave} = \frac{8\omega_0}{3} 2\pi\Delta f_{up} 10^{\left(-2S_{21Mup}/20\right)}. \tag{8.24}$$

From (8.24), β', or the nonlinear spring coefficient can be determined by plotting the right hand side of this equation versus the input power as shown in Figure 8.20

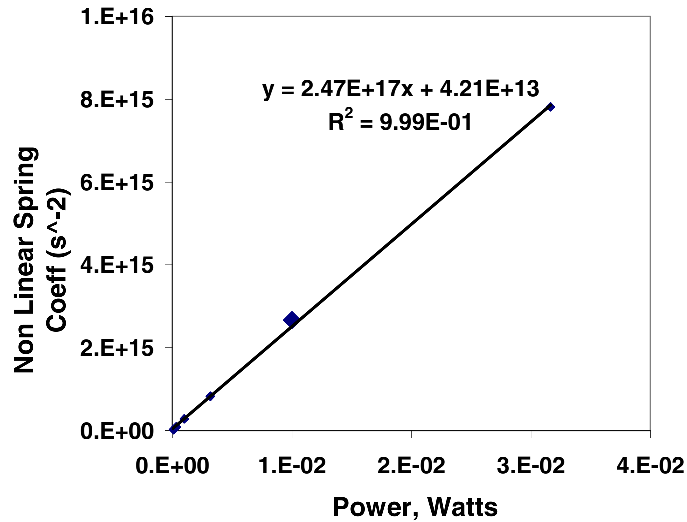

Figure 8.20 Calculated nonlinear spring coefficient versus input power.

The forcing term constant from the equation of motion can be derived again starting with the equations from Ayela

$$A_{mup} = \frac{\sqrt{\Gamma}}{\lambda} = \frac{F_{ac}}{2m\omega_0\lambda} \tag{8.25}$$

combining with relationship for S_{21}

$$\frac{F_{ac}}{A_{in}} = 2m\omega_0\lambda 10^{\left(S_{21Mup}/20\right)} \tag{8.26}$$

then with assumptions for A_{in} and F_{ac}

$$C' = \frac{C_{FP}}{C_{NLP}} = 2m\omega_0\lambda 10^{\left(S_{21Mup}/20\right)}. \tag{8.27}$$

From these values of the damping coefficient, spring constant, and forcing constant a plot of the calculated response can be generated similar to what was done for figure 8.16 in the linear regime. A comparison of the measured response to this calculated response using a MATLAB routine is shown in Figures 8.21 and 8.22 for the same 80 μm resonator from wafer W11. The modeled data matches well with the measured response for the calculated nonlinear damping and spring coefficients. This data indicates that the nonlinear behavior is attributed to Duffing behavior and that the equations in this section can be used to measure the nonlinear damping and spring coefficients for the PZT MEMS resonators.

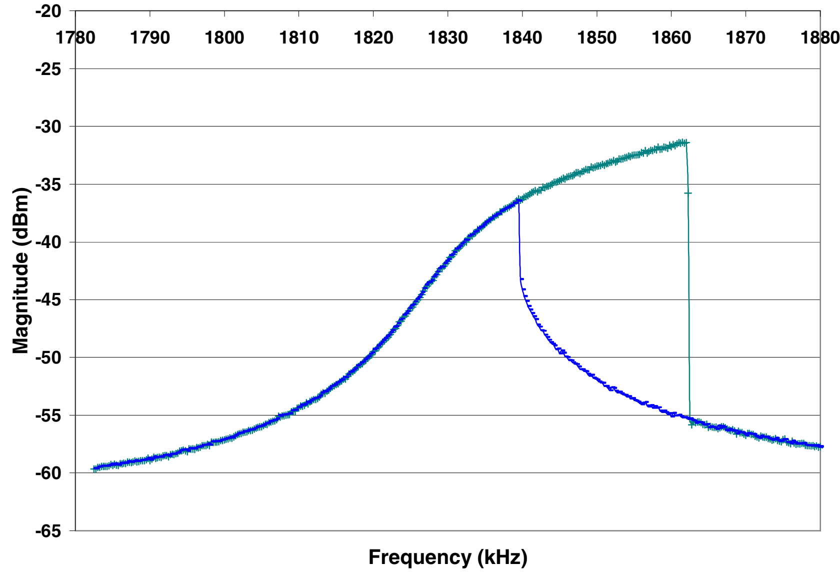

Figure 8.21 Measured nonlinear response of an 80 μm resonator driven at 60 mV.

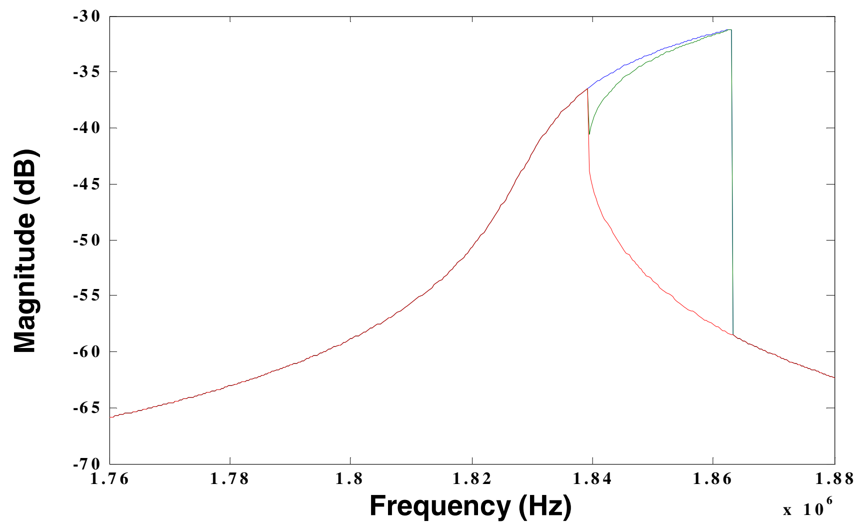

Figure 8.22 Modeled response based on parameters extracted from Figure 8.21.

These techniques were then used to look at the nonlinear spring coefficient as a function of the beam length or resonant frequency. As the beam length is reduced to increase the resonant frequency, the nonlinear spring coefficient is decreased and the linear dynamic range and power handling of the resonators is increased. Figure 8.23 shows the effect of

the decreasing nonlinear spring coefficient with decreasing beam length by overlaying the frequency response of a 400 and a 100 μm resonator both driven at 20 mV. Only the 400 μm resonator exhibits nonlinear behavior.

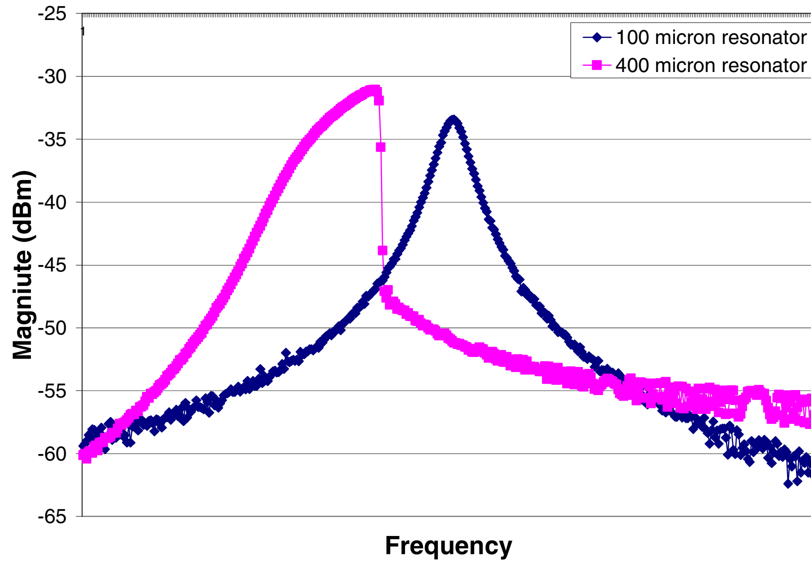

Figure 8.23 Overlaid response of a 100 and 400 μm resonator driven a 20 mV.

From equations (8.17) and (8.18), the frequency sweep up data is affected by damping or the operating pressure whereas the frequency sweep down data should not be affected by pressure. This was validated experimentally and is shown in Figure 8.24 for a 400 μm resonator driven at 223 mV where an observable change is seen for the up sweep data but no difference is seen for the down sweep data. This further confirms the response is following Duffing behavior and that air damping, or lower Q, can offset the Duffing behavior and lead to an increase in dynamic range.

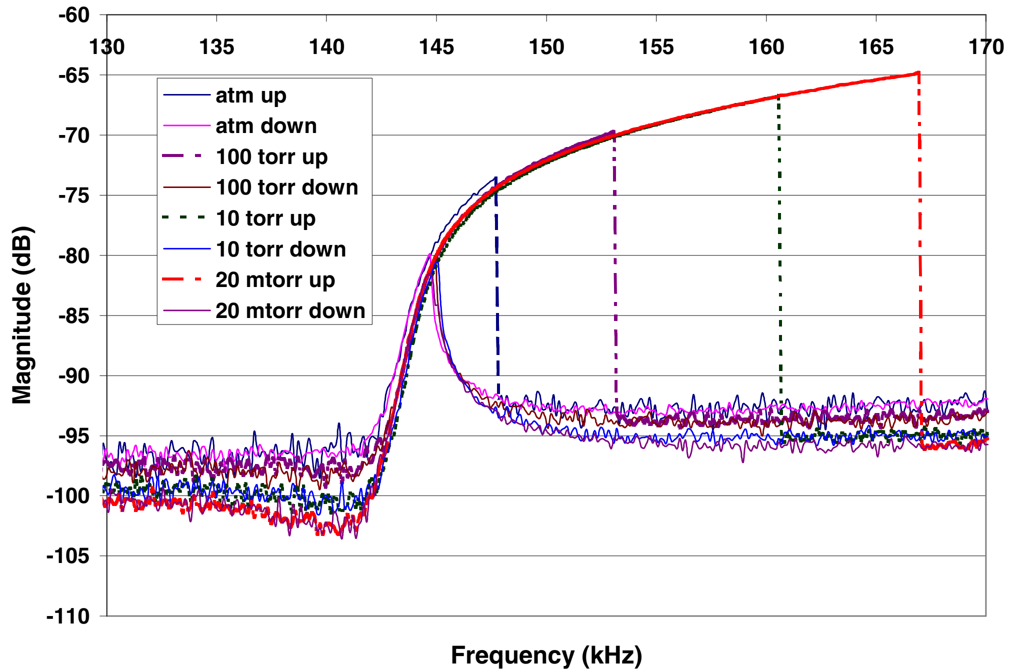

Figure 8.24 Nonlinear Duffing behavior as a function of operating pressure.

From the data in section 8.6, as the beam lengths are shortened to increase the resonant frequency the linear dynamic range will be increased as well. Air damping can further be used to increase the linear dynamic range with the trade off of lower Qs.

8.7 Generation II Resonator Mode Shape Analysis

All of the fabricated devices on wafers W11 and W12 (first generation II fabrication run) where either destroyed or lost prior to the acquisition of the LDV test setup described in Chapter 4 for looking at the mode shapes of the resonators. Subsequently, a second run of generation II resonators that included wafers W9 and W10 listed in Table 8.5 and a third run consisting of the matrix of wafers listed Table 5.3 for the FEM validation where fabricated.

Table 8.5 Film thickness for clamped-clamped beam resonators.

Material Thickness	W9	W10
SiO2 (µm)	2.03	0.72
Ti (µm)	0.02	0.02
Bottom Pt (µm)	0.17	0.17
PZT (µm)	0.44	0.44
Top Platinum (µm)	0.165	0.17

Electrically, the resonators from both the second and third fabrication runs performed in a similar fashion to wafers W11 and W12. Figure 8.25 shows the electrical response from a 200 µm resonator from wafer W10. Resonators from W10 showed some of the highest Qs of any clamped-clamped resonators tested, with a Q of 4700 at 134 kHz and 3840 at 300 kHz respectively.

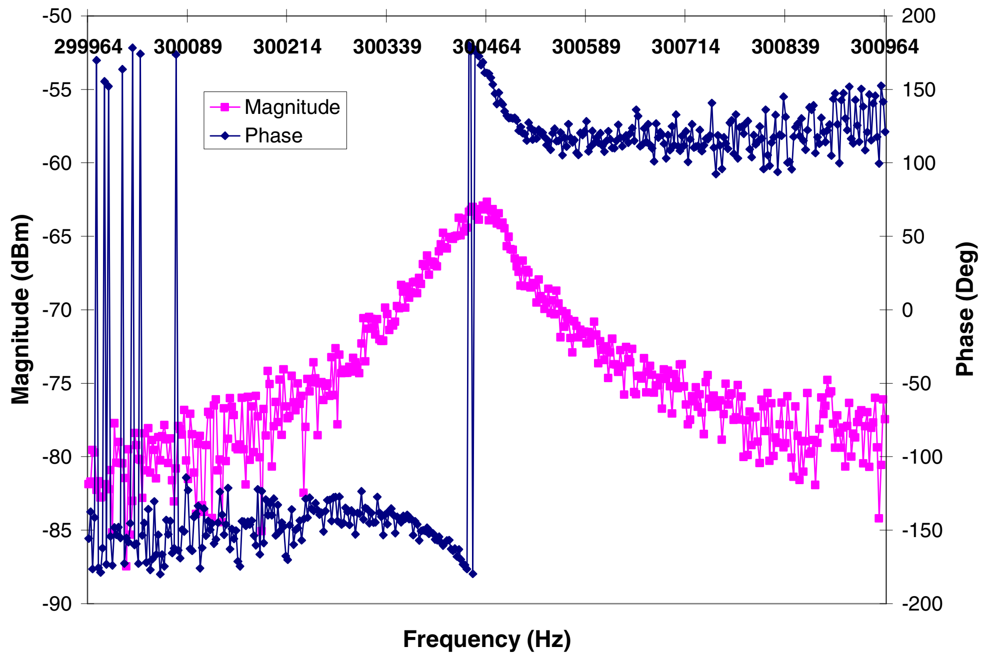

Figure 8.25 200 µm response from wafer W10

An unexpected result in testing these generation II resonators with the LDV test setup described in chapter 4 is that nonlinear modes and secondary peaks appeared within the for devices from wafers W1, W2, W3, W4, and W10 from Table 5.3. This would be expected for an internal resonance of a buckled beam as seen in the generation I resonators discussed in Chapter 7 but not in the apparently planar generation II resonators. The generation II resonators tested for this work were shown to be under a net tensile loading as measured from the wafer bow testing on the blanket films (see Table 5.7), from the observed increase in resonance frequency and modeling work in Chapter 6, and by the visually planar devices seen by SEM inspection as shown in Figure 8.1. Figure 8.26 shows a close up image of the anchor and transition areas at the end of the electrode for the same resonator shown in Figure 8.1 with no observed bowing in either image.

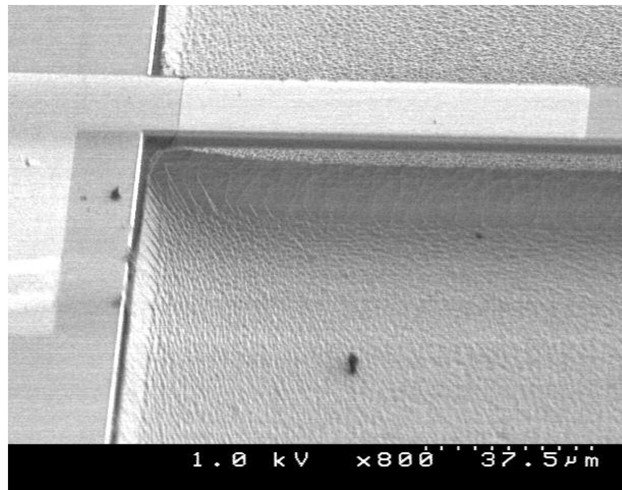

Figure 8.26 SEM of electrode area on 400 μm resonator shown in Figure 8.1.

In the LDV velocity spectrum data, this mode coupling shows up as a shoulder or secondary peak superimposed with the main fundamental mode resonant peak as seen in Figure 8.27 for a 400 μm long beam from W3. Figures 8.29 and 8.30 give snap shots of the resonant mode shape at points 1-4 shown in the frequency spectrum of Figure 8.28.

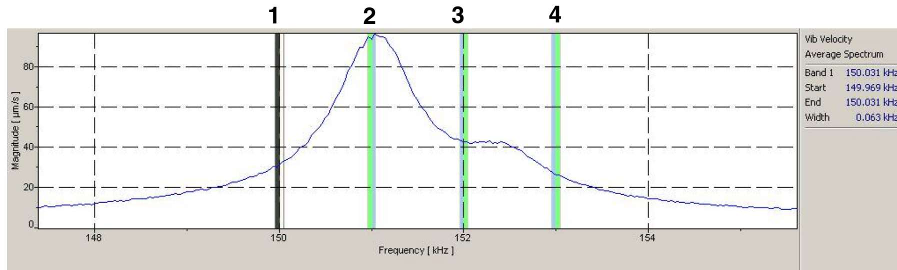

Figure 8.27 LDV velocity spectrum for 400 μm resonator from wafer W3.

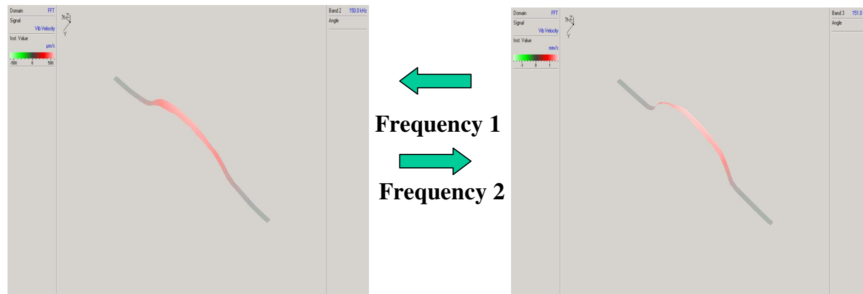

Figure 8.28 Measured mode shapes at frequencies 1 and 2 from Figure 8.27.

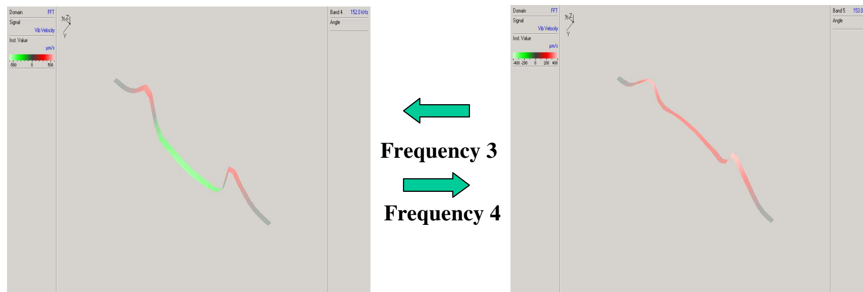

Figure 8.29 Measured mode shapes at frequencies 3 and 4 from Figure 8.29.

Qualitatively, for the non-fundamental modes, the center of the beam exhibits phase lag compared to the electrode areas. Eventually the fundamental mode returns as the frequency is increased.

The distinct secondary shoulder in the LDV data was not apparent in the electrical testing as seen in Figure 8.30 for the same 400 μm resonator for which LDV data is shown in Figure 8.27. Although, at the 10 mV drive voltage used in the LDV, the onset of the Duffing behavior is apparent in the electrical response, little or no change could be seen in the LDV data and resulting mode shape response for drive voltages as high as 120 mV. Figure 8.30 was taken in vacuum and the LDV data was taken in air, which at the 10 mV voltage level dampens the response and eliminates any Duffing behavior. This effect of pressure is shown in Figure 8.24 for the case of a resonator driven at 20x larger drive voltage than typically used in the LDV measurements and for the data in figure 8.30.

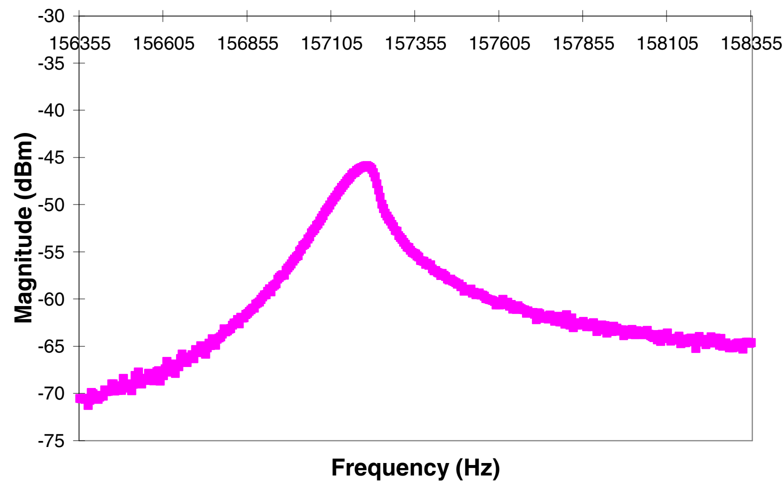

Figure 8.30 Electrical response of 400 μm resonator from W3 driven at the 10 mV drive voltage used for LDV testing.

An initial theory was that the reactant force to the piezoelectric actuation was large enough to create buckling in the beam during operation resulting in mode coupling similar to what was seen for the generation I resonators discussed in Chapter 7 and shown in Figures 7.9 and 7.10. Table 8.6 shows a comparison of the critical Euler buckling force for a 400 micron beam from each wafer to the block force generated in the beams using equation (2.13) with an applied voltage equal to that used for the LDV testing of 10mV.

Table 8.6 Critical euler buckling force and stress.

Wafer #	Resultant Applied Force (N x 10^{-8} @ 10 mV)	Euler Critical Buckling Force (N x 10^{-8})	Euler Critical Buckling Stress (N/m^2 x 10^5)
W1	5.32	994	2.58
W2	10.0	1,750	3.67
W3	1.61	7,060	11.7
W4	5.17	7,550	11.2
W5	6.75	1,160	3.87
W6	5.32	891	2.57
W7	1.43	4,710	10.4
W8	5.42	6,430	10.1
W9	1.16	6,070	10.8

From Table 8.6, the resultant forces generated within the beam are a couple orders of magnitude lower than the required force necessary to buckle the beams. Based on this analysis, piezoelectrically-induced beam buckling was ruled out as a source for the observed multi-mode interactions.

These secondary modes were not initially seen on wafers W5, W6, W7, and W8. On closer examination with a fine frequency step, the same nonlinear response was found near the resonant peak even though a distinct secondary peak or shoulder was still not

apparent. Figures 8.31 through 8.33 show the LDV velocity spectrum and relevant mode shapes for a 400 μm resonator from wafer W9 that shows a mixed mode shape near the resonant peak.

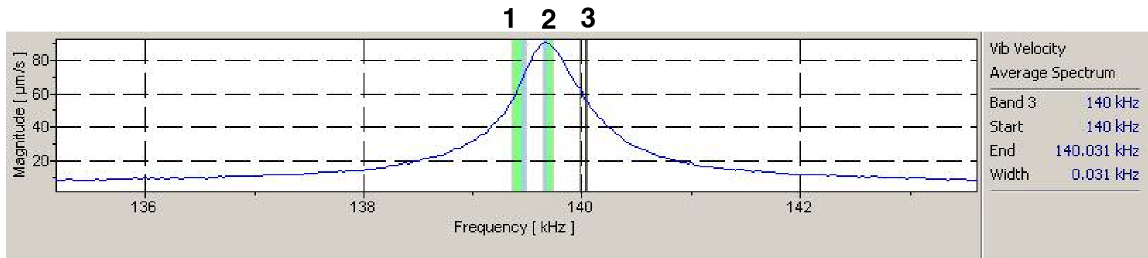

Figure 8.31 LDV velocity spectrum for 400 μm resonator from wafer W9.

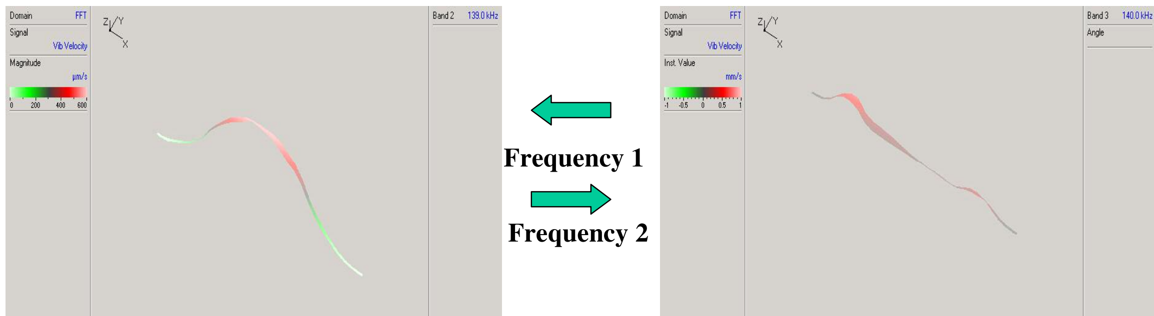

Figure 8.32 Measured mode shapes at frequencies 1 and 2 from Figure 8.31.

Figure 8.33 Measured mode shape at frequency 3 from Figure 8.31.

This nonlinear effect as seen in Figures 8.31 through 8.33, can be found in all of the generation II devices with varying degrees of separation from the fundamental resonant peak. The one obvious difference between these wafers and wafers W1, W2, W3, and W4 is that wafers W1, W2, W3, and W4 all had thick top and bottom electrodes (~200nm) whereas the rest of the wafers with the exception of W9 and W10 have thin (~100 nm) top and bottom electrodes. Discontinuities in the beam (like the termination of the top electrode) can simulate an increase in the static deflection and can lead to a nonlinear response. For all of the wafers, the nonlinear response occurred as a phase lag between the quarter electrodes. To test whether this was a superposition of a higher mode as in the buckled beam response or the effect of discontinuities within the beam, two additional electrode configurations were tested. The first one still used a quarter-length drive electrode but incorporated a sense electrode that covered half of the resonator instead of the normal quarter length as shown in Figure 8.34.

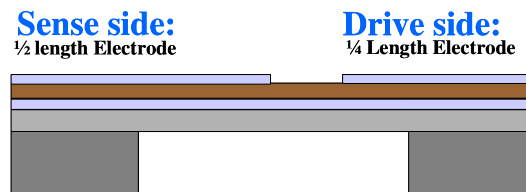

Figure 8.34 Alternative resonator design with a ½ length sense electrode.

Figures 8.35 and 8.36 show the response of one of these resonators from wafer W3 whose normal configuration response is shown in Figure 8.27 through 8.29.

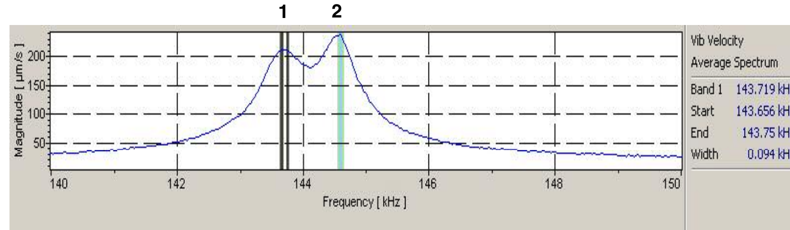

Figure 8.35 LDV velocity spectrum response with ½ length sense electrode.

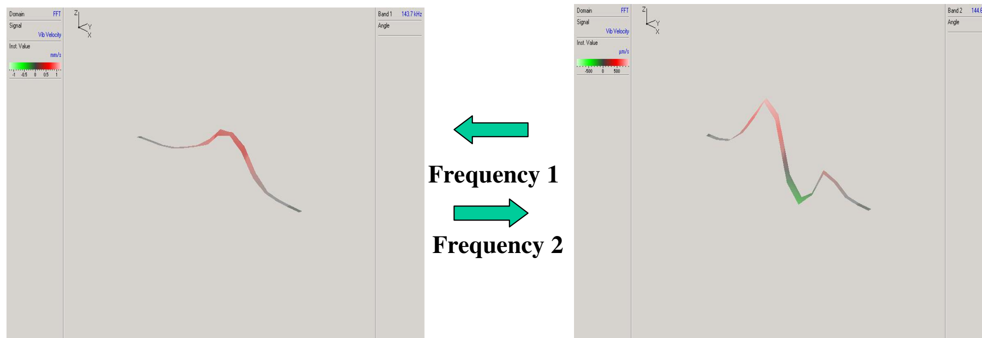

Figure 8.36 Measured mode shapes at frequencies 1 and 2 from Figure 8.35.

From Figure 8.35, the secondary peak is still present and even more prominent than in Figure 8.27 for the normal configuration. From Figure 8.36, the phase lag is still present but has shifted and again only occurs between the electrode areas between ½ to ¾ of the resonator length. This suggests that the phase lag is directly related to the discontinuity in the beam and not coupling to an overall higher resonant mode as shown in the buckled generation I resonators.

The second new configuration tested used quarter-length electrodes but removed the PZT layer between the electrodes as shown in Figure 8.37 to create a larger discontinuity along the beam length.

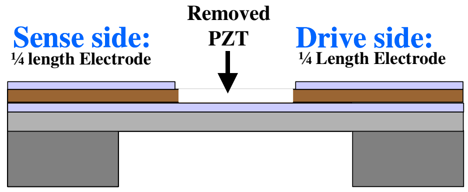

Figure 8.37 Second alternative design with PZT removed from center section.

Figures 8.38 through 8.40 show the response for a 400 μm resonator with this configuration from wafer W3.

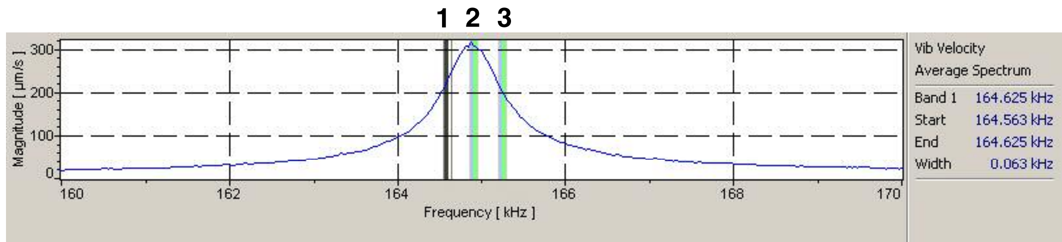

Figure 8.38 LDV velocity spectrum of a 400 μm resonator with the PZT removed from between the electrodes.

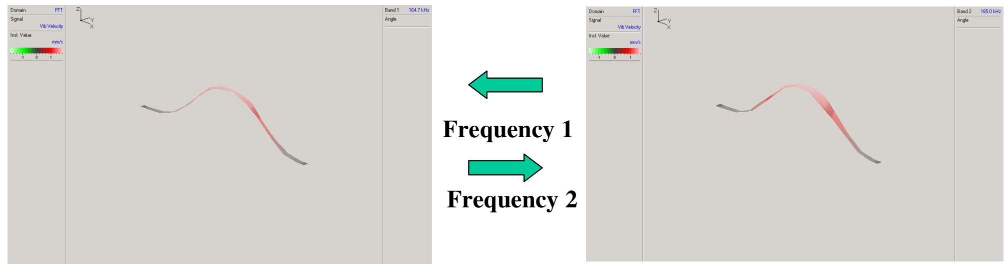

Figure 8.39 Measured mode shapes at frequencies 1 and 2 from Figure 8.38.

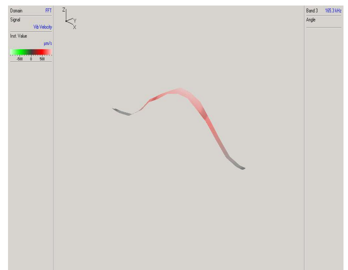

Figure 8.40 Measured mode shapes at frequency 3 from Figure 8.38.

These devices did not show any signs of phase lag along the entire length of the resonator. Conversely, a resonator of similar design from wafer W9, which only showed a small amount of lag in the normal configuration, had an increase in the amount of phase lag at resonance with the middle PZT removed although no secondary peak was observable as shown in Figures 8.41 and 8.42.

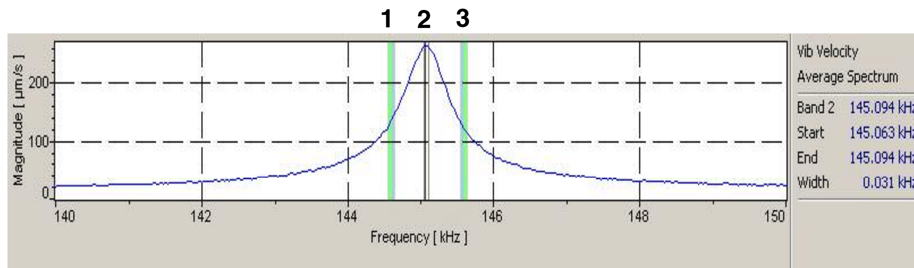

Figure 8.41 LDV velocity spectrum of a 400 µm resonator from wafer W9 with the PZT remove from between the electrodes.

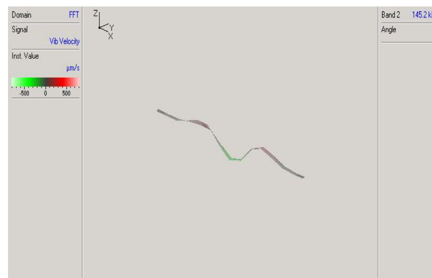

Figure 8.42 Measured mode shape at frequency 2 from Figure 8.41.

This further confirmed that the electrode/beam discontinuity configuration contributes to the nonlinear mode shapes and but that removing the PZT from the beam center to create a large discontinuity does not shift the secondary peak further right but moves the secondary peak lower in frequency relative to the main peak and in the case of wafer W3, eliminates the phase lag effect.

Figure 8.43 plots the ratio of the neutral axis in the electrode section of the beam to that of the nonelectroded section in the middle of the beam for wafers W1 through W9 and includes the resonators from W3 and W9 that had the middle PZT removed.

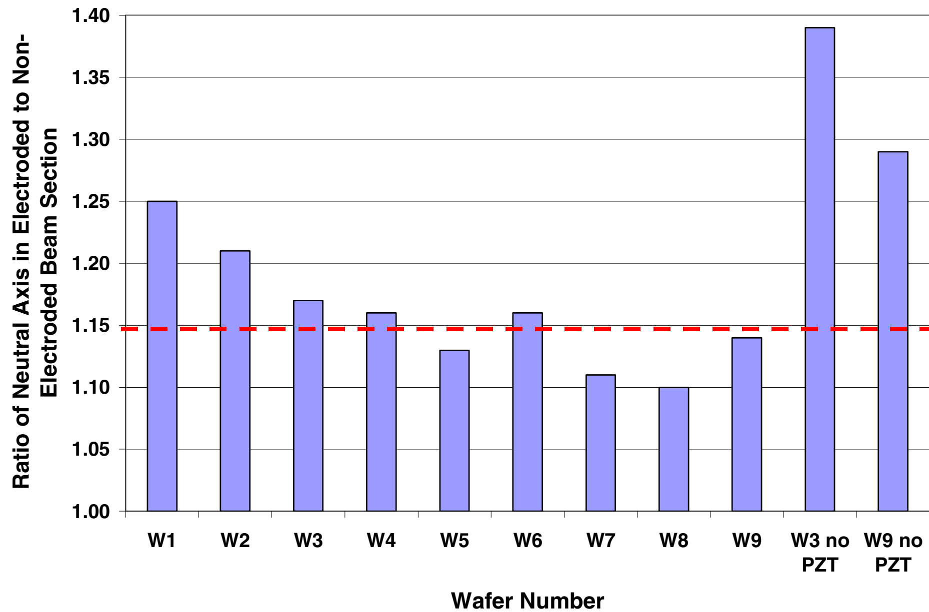

Figure 8.43 Plot of ratio of neutral axis in the electrode section of the beam to the nonelectroded section of the beam.

From Figure 8.43, wafers W5 through W9 that showed the least amount of nonlinear behavior on average had a lower change in neutral axis ratio than wafers W1 through W4. Wafer W6 had the thinner top electrode but a larger ratio than the other wafers in that same group and it did exhibit a small secondary peak similar to that seen in wafers W1 through W4. Typical LDV velocity spectrums for resonators from wafers W1 through W9 are shown in figure 8.44. Therefore, for future designs this ratio needs to be minimized in order to prevent the creation of nonlinear mode shapes.

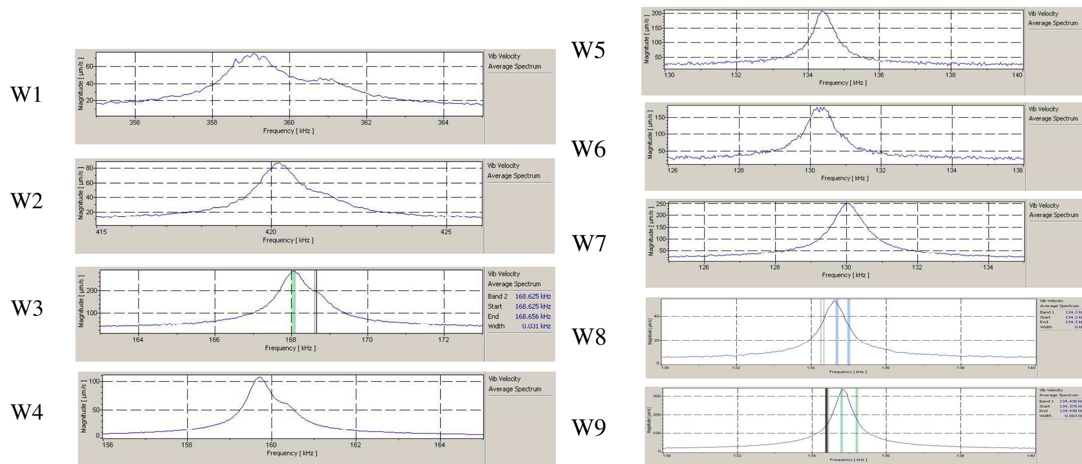

Figure 8.44 Measured LDV velocity spectrum for resonators from wafers W1 - W9.

This cannot be the whole story, however, because removing the PZT from the middle of the resonators from wafer W3 and W9 significantly increased the ratio for both devices over their quarter-length electrode counterparts as shown in Figure 8.43. Removal of the middle PZT layer leads to a significant change in the stress gradient that can cause a change in the static deflection. The static deflection for all wafers were measured by the optical profilometer described in Chapter 4 and are reported in table 8.7.

Table 8.7 Measured static deflection at center of resonator.

Wafer	Measured Initial Displacements (nm)
W1	522
W3	680
W3 – No Middle PZT	1037
W3 – Half Length Sense Electrode	592
W4	567
W5	670
W6	236
W7	510
W8	600
W9	660
W9 – No Middle PZT	1702
W9 – Half Length Sense Electrode	413

Overall, data from the Veeco revealed center deflections between 236 to 680 nm for the normal quarter length electrode designs with not much difference between wafer groups W1-W4 and W5-W9. Also, not much change was seen for the half-length electrode design but there was a significant increase for the no-middle PZT resonator design of approximately 2x for resonators from W13 and approximately 3x for resonators from wafer W14. From this data, the generation II resonators are slightly bowed in their static state and based on the LDV data that shows the displacement of the resonators is in the pico-meter range, the beams are resonating about their initial deflection point (one-sided resonance). Also, from section 6.5, the clamped-clamped beam should deflect downward given the CTE gradient based on the PZT stack materials. During temperature testing of the resonators, it was also noticed that the spread between the two peaks within the frequency spectrum shifted. Figures 8.45 and 8.46 show a resonator from wafer W1 at room temperature and at 250 ºC respectively.

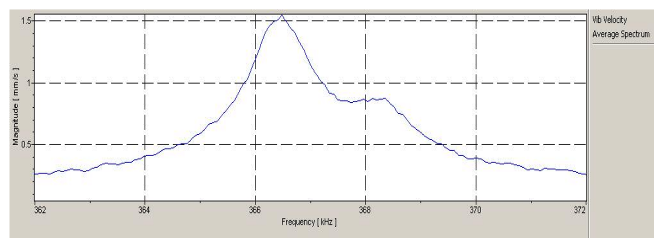

Figure 8.45 LDV velocity spectrum for a 200 μm resonator from W1 at RT.

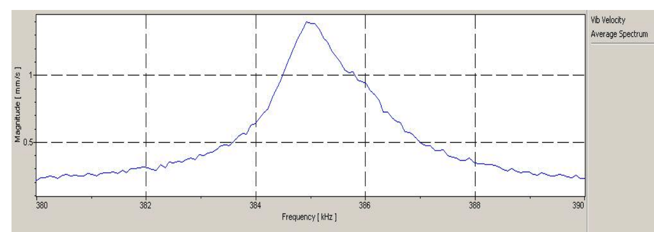

Figure 8.46 LDV velocity spectrum for same 200 μm resonator from W1 at 250 °C.

Besides the overall frequency shift observed by the device, as expected from the model verification in Chapter 6, the distance between the superimposed peaks is also reduced. To test if reducing the static deflection through heating had an effect on the mode coupling at the primary resonant peak, a device from wafer W8, that only showed a small amount of coupling an little to no secondary LDV peaks, was tested at 24 ºC and 100 ºC. Figure 8.47 shows the effect on the center frequency response of the 400 µm clamped-clamped resonator at 24 ºC and 250 ºC respectively.

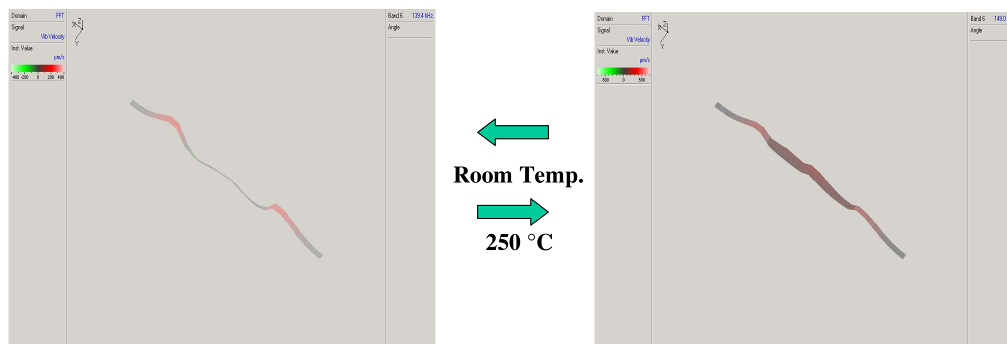

Figure 8.47 Measured mode shape at room temperature and 250ºC for a 400 µm resonator from wafer W8.

Little change was noticed in the LDV velocity spectrum and although the mode coupling could not be eliminated, the amount of phase lag in Figure 8.46 appears to be reduced.

The motivation for the generation III resonators discussed in Chapter 9 was to try and eliminate any nonlinear phase lag behavior by fabricating a resonator with a small variation in the neutral axis and to also incorporate new materials within the dielectric stack in order to modify the stress gradient to achieve highly planar structures.

8.8 Additional Analysis of Generation II Clamped-Clamped Resonator Nonlinear Response

Typically the resonators are driven from one side and sensed on the other side. In order to see if the asymmetrical actuation mechanism had an effect on some of the additional modes, all of the resonators were tested again but this time they were tested by symmetrically driving both the drive and sense electrodes (ports 1 and 2) instead of the normal asymmetric drive (driven at port 1). Figures 8.48 and 8.49 show the LDV velocity spectrum data for a resonator from wafer W6 (did not show a distinct secondary peak in LDV data). The first three modes were excited via single drive excitation but only the first and third modes were excited via dual drive excitation.

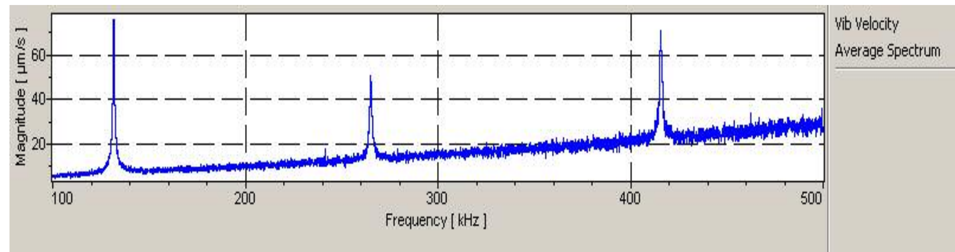

Figure 8.48 LDV velocity spectrum for single-drive excitation on W6.

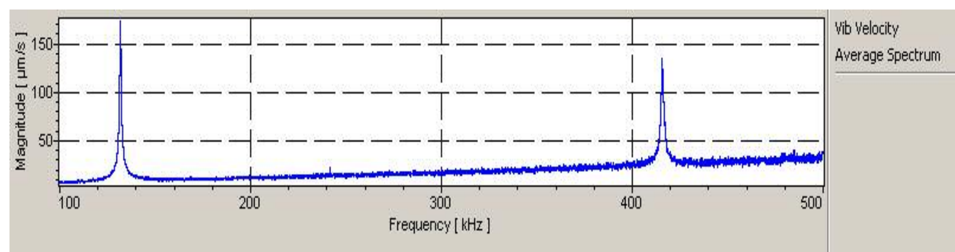

Figure 8.49 LDV velocity spectrum for dual-drive excitation on W6.

It is interesting to note that none of the peaks in the LDV velocity spectrum for either method show a secondary peak, but a small amount of the nonlinear phase lag near the resonant peak can still be seen.

Figures 8.50 and 8.51 show the results from a similar test for a resonator from wafer W3 (did show the distinct secondary peak in the LDV data). The first two modes were excited by both single and dual drive excitation. The third mode is above the measure capability of the scanning LDV system. Distinct secondary peaks are seen for both modes.

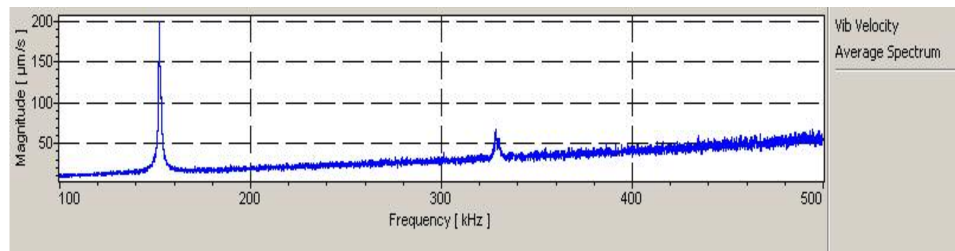

Figure 8.50 LDV response for single-drive excitation of a 400 µm from W3.

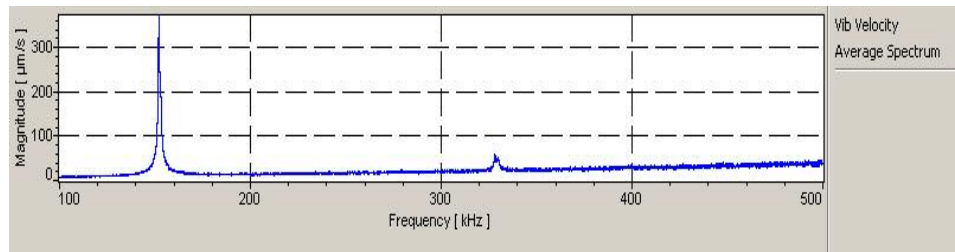

Figure 8.51 LDV response for dual-drive excitation for a 400 µm resonator from W3.

For dual drive actuation on this same resonator, both the first and second modes can still be seen and secondary peaks are still visible within the two main resonant peaks. This mode coupling can be seen across the rest of the matrix of wafers as listed in Table 8.8

Table 8.8 Comparison of measured dual drive actuation to modeled modal analysis for a 400 μm resonator.

Wafer	Measured mode 1 (Hz)	Stress Modeled Mode 1 (Hz)	No Stress Modeled Mode 1 (Hz)	Measured mode 2 (Hz)	Stress Modeled Mode 2 (Hz)	No Stress Modeled Mode 2 (Hz)	Measured mode 3 (Hz)	Stress Modeled Mode 3 (Hz)	No Stress Modeled Mode 3 (Hz)
W1	136,797	151,312	48,404	273,000	295,653	119,122	429,000	459,802	233,316
W3	152,031	111,130	85,695	328,203	254,750	218,650	N/A	465,470	425,963
W4	158,949	163,936	87,114	346,563	346,543	225,586	N/A	588,693	442,341
W5	136,016	139,310	54,389	N/A	285,340	142,903	450,938	458,420	281,088
W6	131,797	151,123	43,773	N/A	298,340	112,709	415,547	462,380	220,947
W7	133,203	141,107	76,955	N/A	298,867	203,000	N/A	509,223	396,574
W8	136,541	141,114	81,350	N/A	305,881	215,990	N/A	527,917	423,307
W9	140,000	142,404	77,123	N/A	299,150	199,787	N/A	505,660	389,443

This data indicates that the stepwise construction and variation in the neutral axis of the resonator can contribute to the overall nonlinear response of the resonator in the form of mode coupling but that the drive method has little effect on creating or reducing the phase lag seen within a resonant peak.

In another test of this concept, the devices from wafers W3 and W6 were tested again but this time with a single sine wave at the principal resonant frequency instead of the frequency sweep used in Figures 8.48 thorough 8.51. Figure 8.52 shows the LDV velocity spectrum for the resonator from wafer W3. In addition to the primary resonant peak at the drive frequency, small peaks can be seen in Figure 8.52 at two times and three times the drive frequency indicating nonlinear behavior and mode coupling within the device.

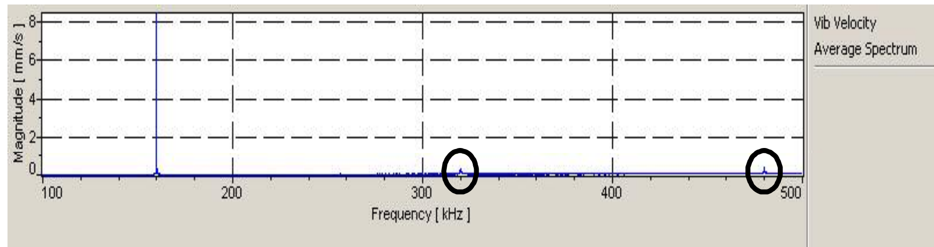

Figure 8.52 LDV spectrum for a 400 µm resonator driven at a fundamental frequency.

Figure 8.53 shows a similar LDV velocity spectrum for the resonator from wafer W6. No additional resonant peaks were seen within the data indicating no measurable nonlinear behavior or mode coupling.

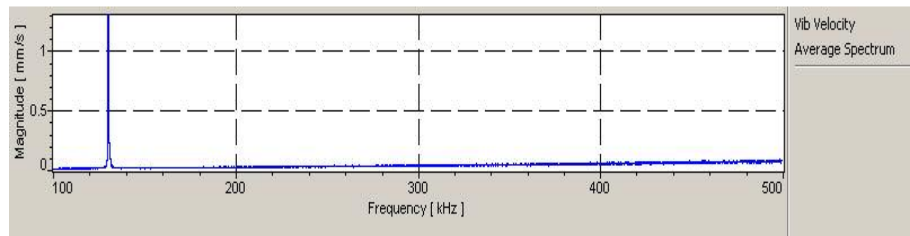

Figure 8.53 LDV spectrum for a 400 µm resonator driven at the fundamental frequency.

From the data in Figures 8.50 through 8.53, resonators that exhibit side peaks within the LDV velocity spectrum have inherently larger nonlinear response in that harmonics can be excited at resonance.

Chapter 9. Stress Compensated Resonators

9.1 Generation III Resonator Design and Fabrication

The goal of the generation III resonator designs was to try and eliminate any nonlinear phase lag behavior by fabricating a resonator with a small variation in the neutral axis and to also incorporate new materials within the dielectric stack in order to modify the stress gradient to achieve highly planar structures.

Researchers at ARL have investigated several techniques to further modify the stress gradient to produce planar structures. PZT cantilever beams have been fabricated with upward, zero, and downward curvatures by modifying the PECVD SiO_2 process or the top Pt anneal [81]. Another technique being explored, and the one used for this research, is to incorporate a Si_3N_4 thin film layer into the oxide dielectric stack structure to modify the stress gradient.

The addition of the Si_3N_4 layer and its material properties has three effects on the clamped-clamped resonator design. From Chapter 5, the Young's Modulus Si_3N_4 was found to be 293 GPa which is much larger than the normally used SiO_2. The increase in Young's modulus leads to an increase in the resonant frequency for a given beam geometry. Secondly, the CTE for Si_3N_4 was also measured and is approximately 4x larger than that for SiO_2 and close to that of the silicon substrate so the overall temperature coefficient of the resonator should be modified slightly. Finally, the addition of the Si_3N_4 layer modifies the stress gradient and offsets the high tensile stress seen in the Pt layer and can result in very planar devices.

Two different generation III resonator configurations were fabricated with variation in the PZT thickness while maintaining the same electrode thickness. The same mask set and process as the one used for the generation II resonators was used with the following exceptions:

- An oxide-nitride-oxide dielectric layer was substituted for the oxide only dielectric layer in the generation II resonators

- The bottom metal was deposited in ARL's new Unaxis CLC sputtering system with a Ti\TiO_2\Pt\Ti structure that is 180 nm thick instead of the normal Ti\Pt structure since the system used for the normal Ti\Pt deposition was down at the time of fabrication.

A comparison of the two resonator geometries is given in Table 9.1.

Table 9.1 Material thickness for generation III resonators.

Wafer	W13	W14
First Oxide Layer Thickness (nm)	100.0	100.0
Nitride Thickness (nm)	50.0	50.0
Second Oxide Layer Thickness (nm)	85.0	85.0
PZT Thickness (nm)	500.0	1000.0
Ratio of Neutral Axis (Electrode to No electrode)	1.13	1.11

The ratio of neutral axis ratio puts the resonators from both W13 and W14 in the region for minimal phase lag from Figure 8.43 with resonators from W13 more likely to see a secondary peak and nonlinear behavior because of the higher neutral axis ratio.

During the fabrication, wafer bow measurements were taken to measure the residual stress in each layer. The PECVD oxide-nitride-oxide film is deposited in one single step so the stress data is for the composite film and not for any one single layer of oxide or nitride. The measured values for stress are given in Table 9.2. The addition of the nitride layer increases the overall stress in the dielectric layer leading to a smaller stress gradient than that seen in the data from Table 5.8 for the generation II resonators.

Table 9.2 Measured stress in generation III resonators.

Wafer	W13	W14
Stress in Dielectric (MPa) (post anneal)	95	167
Stress in Bottom Metal (MPa) (post anneal)	584	609
Stress in PZT (MPa)	53	101

Using the material properties from Chapter 5 for Si_3N_4 and the stress values from Table 9.2, the ANSYS FEM model used in Chapter 6 was modified to add the additional Si_3N_4 layer for investigating its effect on the beam curvature. The final stress gradient was generated using similar techniques to those used in Chapter 5 by modeling the static stress-induced cantilever deflection of cantilevers from both wafers. Figure 9.1 shows the Veeco optical profilometer data for 100, 200, 300, and 400 μm cantilever deflections for

cantilevers from wafer W13. Figure 9.2 shows the ANSYS modeled deflection of a 300 µm cantilever. Figures 9.3 and 9.4 show the same data for cantilevers from wafer W14.

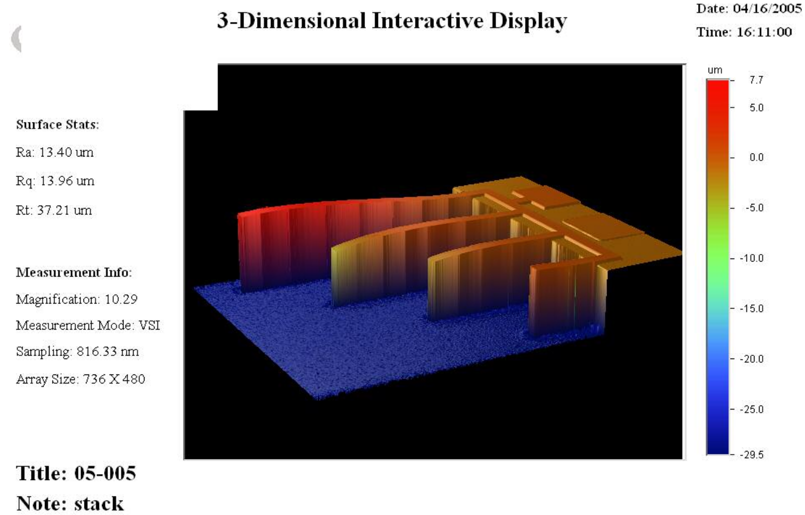

Figure 9.1 Measured cantilever stress-induced tip deflections from wafer W13.

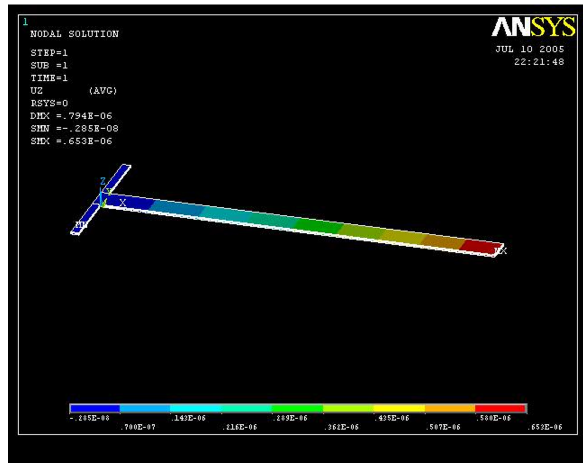

Figure 9.2 Modeled cantilever stress-induced deflection for a 300 µm resonator from wafer W13.

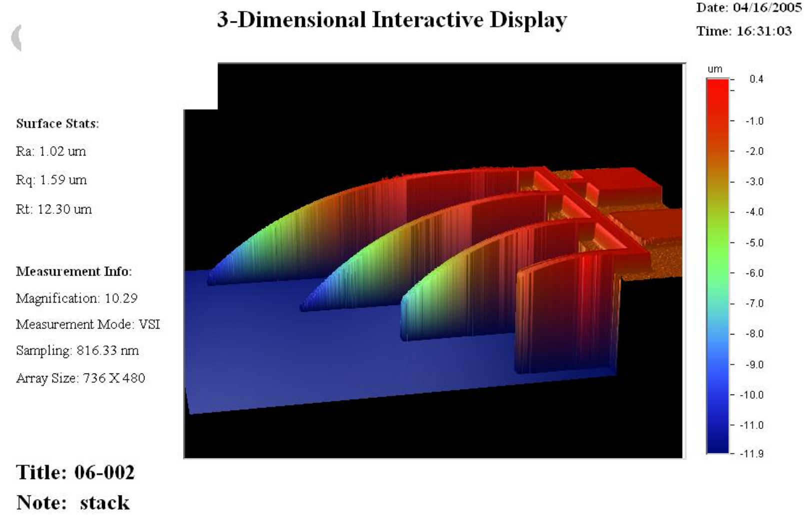

Figure 9.3 Measured cantilever stress-induced deflections from wafer W14.

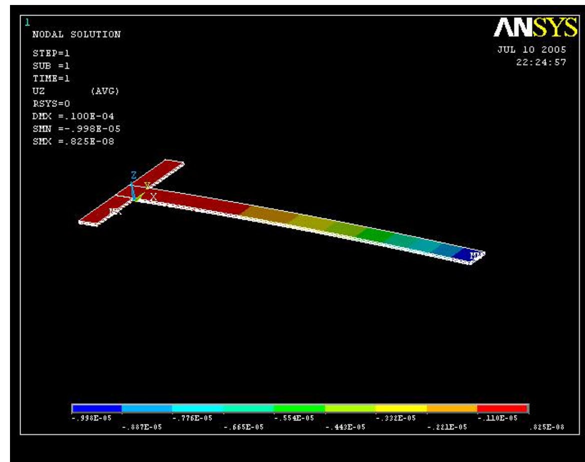

Figure 9.4 Modeled cantilever stress-induced deflections for a 300 µm resonator from wafer W14.

Whereas cantilevers on wafer W13 were almost planar and actually had some devices bowed up or bowed down, cantilevers from wafer W14 were all slightly bowed down with a deflection of approximately -11 µm for a 300 µm cantilever. All previous cantilevers from generation I and II wafers, exhibited severe upward bows. The ANSYS modeled results closely approximated the measured results with the model predicting a deflection of 0.65 µm for a 300 µm cantilever from wafer W13 and –9.98 µm for a 300

μm cantilever from wafer W14. Figure 9.5 is an SEM image of a 400 μm resonator from wafer W14 showing a very planar structure.

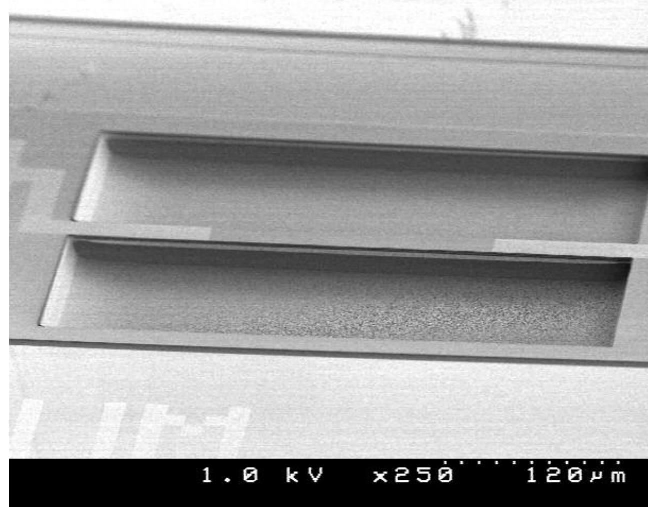

Figure 9.5 SEM image of a fabricated generation III resonator from wafer W14.

Resonators from both wafer W13 and W14 were measure on the optical profilometer and both devices had much smaller center deflections than the previous generation II resonators. 400 μm resonators from wafer W14 had between 6 to 60 nm of center deflections while those from wafer W13 had center deflections ranging from 60 nm up to 120 nm. These results compare favorably to the generation II resonators that exhibited typical center deflections ranging from 200 to 500 nm.

The FEM model was then used to see the effect of the placement of the Si_3N_4 layer within the stack on the clamped-clamped beam center deflection. Table 9.3 shows the modeled center deflections for a 400 μm resonator from wafer W14 for four different locations for the Si_3N_4 layer within the dielectric stack.

Table 9.3 Effect of nitride layer position on beam deflection and resonant frequency.

Stack thickness (nm)	Modeled clamped-clamped beam center deflection (nm)	Modeled Frequency (kHz)
Bottom oxide = 100 Nitride = 50 Top Oxide = 850	77	187.1
Bottom oxide = 300 Nitride = 50 Top Oxide = 650	78	186.6
Bottom oxide = 500 Nitride = 50 Top Oxide = 650	79	186.1
Bottom oxide = 700 Nitride = 50 Top Oxide = 250	81	185.7

From the data in table 9.3, the lower the Si_3N_4 layer was within the stack resulted in less initial static deflection but there is not much difference. Therefore, the addition of the Si_3N_4 layer is significant in modifying the overall stress gradient and beam deflections but the location of the layer within the stack should only make minor additional changes.

9.2 Generation III Resonator Performance

Figures 9.6 and 9.7 show representative electrical response for a 400 µm resonator from each wafer. As predicted by the FEM, the resonant frequencies were increased over generation I and II resonators with the same beam geometries. The resultant frequencies were approximately 201 kHz and 191 kHz for a 400 µm resonator from wafer W13 and W14 respectively. The Qs for these devices are 2500 for wafer W13 and 2440 for W14. These values are within the same range of the generation II resonators that were tested so no significant increase or loss in Q was observed by going to the multilayer stack

configuration. The resonator admittance or peak size was also similar to the results seen from the generation II resonators.

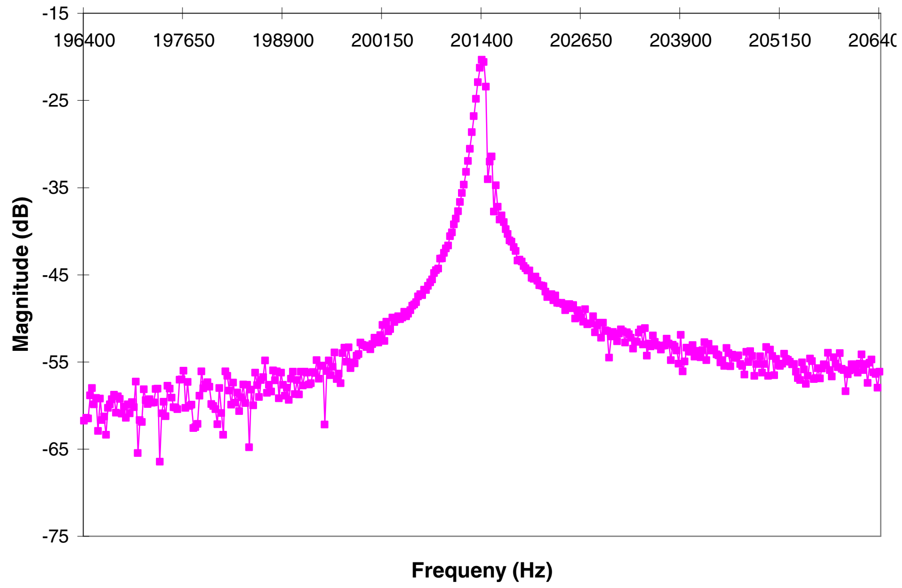

Figure 9.6 Magnitude response for a 400 μm resonator from wafer W13.

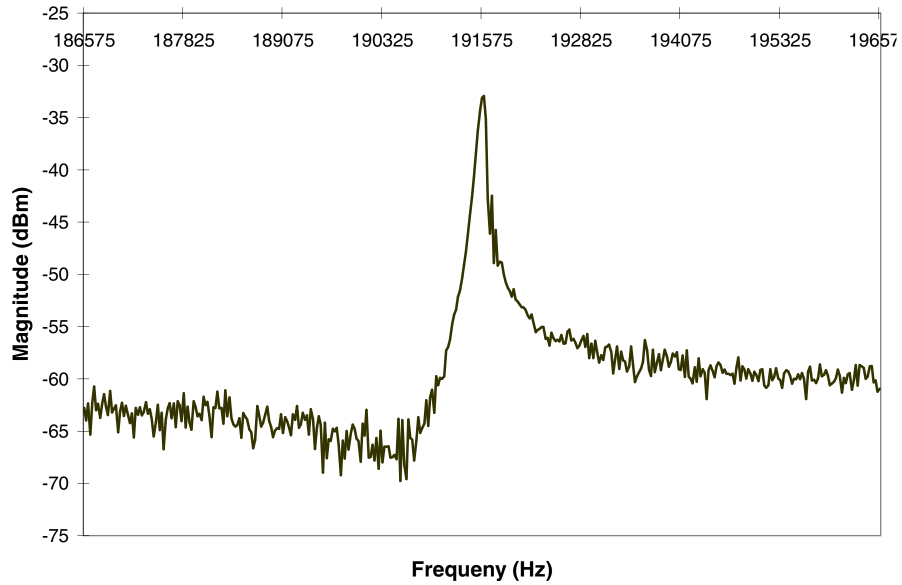

Figure 9.7 Magnitude response for a 400 μm resonator from wafer W14.

9.3 Generation III Resonator Mode Shape Analysis

Devices from wafer W14, which exhibited the lowest center deflections (as small as 6 nm) do not reveal any secondary peak within the LDV data and no higher modes or phase lag can be found within the resonance peaks. Figure 9.8 shows the LDV velocity spectrum for a 400-µm resonator from wafer W14. Figures 9.9 and 9.10 show the mode shapes found at frequencies within the peak from Figure 9.8.

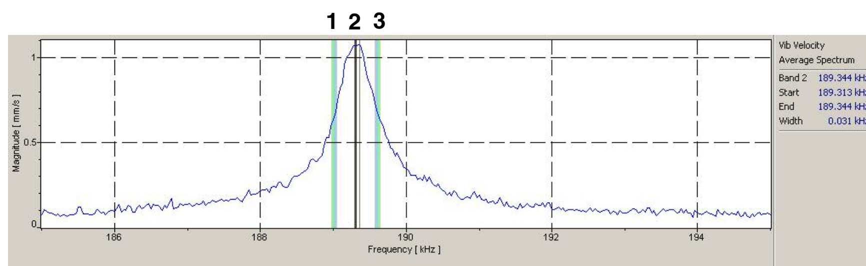

Figure 9.8 LDV velocity spectrum response for 400 µm resonator from W14.

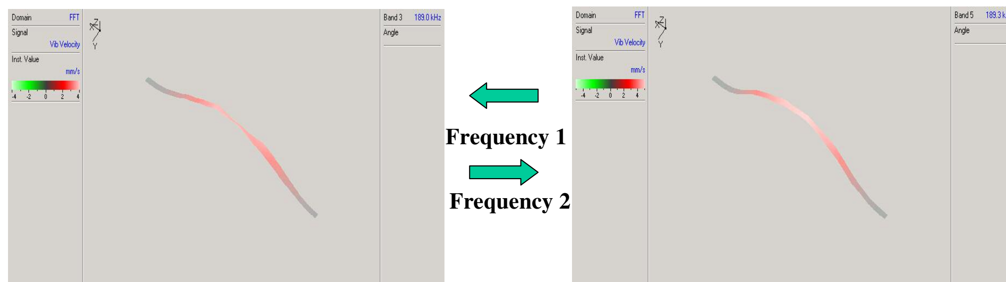

Figure 9.9 Measured mode shapes at frequencies 1 and 2 from Figure 9.9.

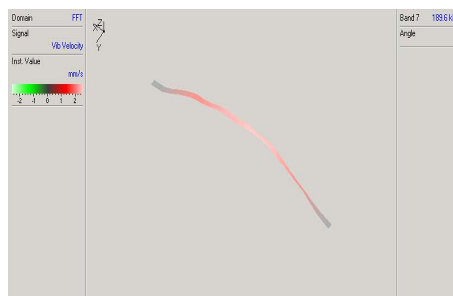

Figure 9.10 Measured mode shape at frequency 3 from Figure 9.9.

Conversely, Figure 9.11 shows the velocity spectrum for a 400-µm resonator from wafer W13. Resonators from this wafer show the same characteristic secondary peak in the LDV velocity spectrum as the generation II resonators tested previously. Figures 9.12 and 9.13 show the mode shapes found at frequencies within the two peaks from Figure 9.11.

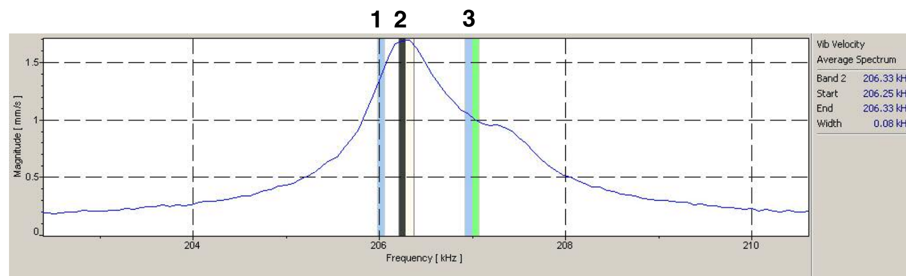

Figure 9.11 LDV velocity spectrum for a 400 µm resonator from wafer W13.

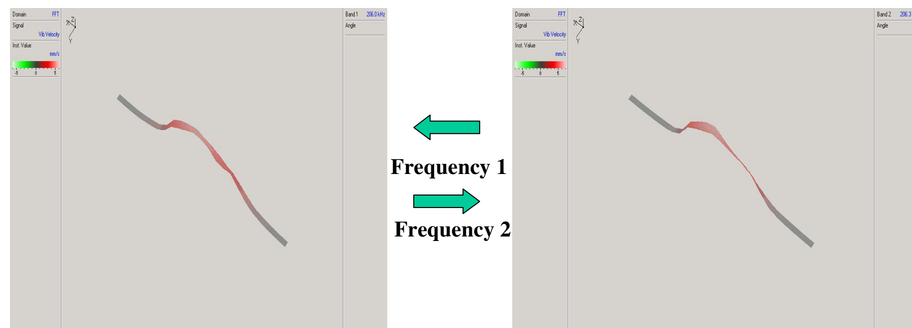

Figure 9.12 Measured mode shapes at frequencies 1 and 2 in Figure 9.11.

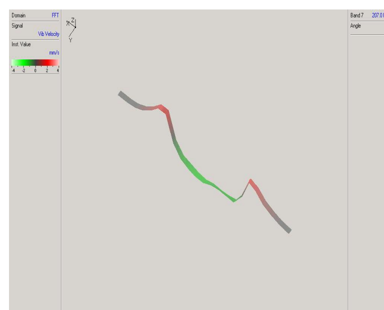

Figure 9.13 Measured mode shape at frequency 3 from Figure 9.11.

This data shows that modification of the stress gradient can be performed to successfully fabricate extremely planar devices, and that the nonlinear phase lag seen in the generation II resonators can be eliminated by minimizing the change in the neutral axis along the beam length.

9.4 Generation III Resonator Thermal Stability

The resonators were also tested thermally to see if the added nitride layer would affect the temperature coefficient of the resonators. Figure 9.14 shows the measured fractional frequency change in the response of 200-μm resonator from wafer W14 compared to 200-μm generation II resonator from wafer W1 when subjected to temperatures from room temperature up to 100 ºC.

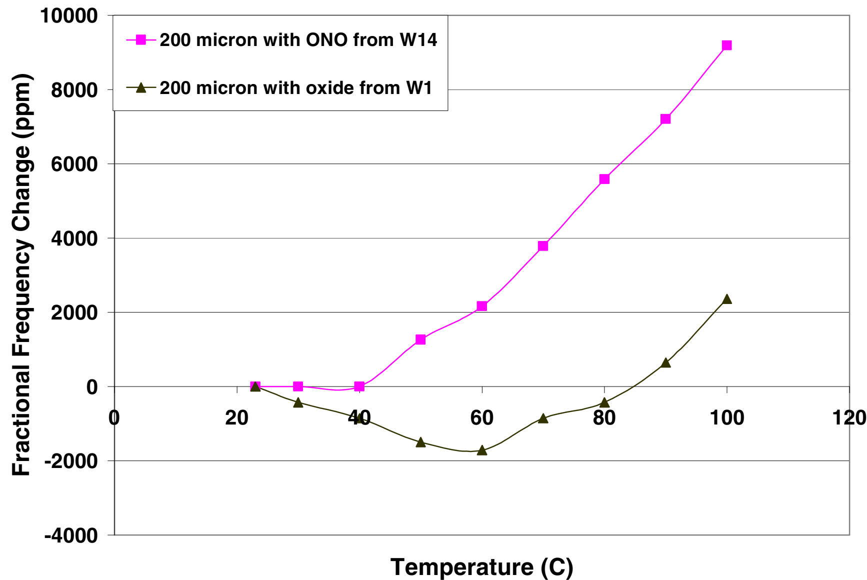

Figure 9.14 Comparison of measured frequency temperature response for oxide versus oxide-nitride-oxide beam structure.

From Figure 9.14, the addition of the nitride layer did have a significant effect on the thermal stability of the resonator. The generation III resonators did not experience the initial drop in frequency experienced by the generation II resonators. This is the result of the modified composite Young's modulus of the stack structure and the overall CTE gradient and composite CTE response for the beam structure obtained by incorporating the higher Young's modulus and higher CTE Si_3N_4 layer within the SiO_2 structure. This means that the new designs are better for providing planar structures with no nonlinear behavior, but they have a trade-off in that they have lower temperature stability.

Chapter 10. Conclusions and Future Work

10.1 Conclusions

The goal of this research was to examine the potential of sol-gel PZT thin films for application to piezoelectric MEMS resonators in the LF to VHF frequency range. In particular, the goal was to compare their performance to previously demonstrated ZnO resonators. Several processing techniques were developed over the course of this research for fabricating suspended PZT MEMS resonator structures. These included processes for ion milling the total PZT stack structure without shorting and for releasing the PZT MEMS structures through both backside and topside release techniques. The PZT resonators fabricated under this effort were the first functioning MEMS devices made from the sol-gel PZT thin film process that was developed jointly by ARL and Penn State under DARPA contract DABT63-95-C-005.

The initial resonators had severe stress gradient issues leading to buckled devices with center deflections of seven microns or more for a clamped-clamped beam. Resonance about these buckled mode shapes was demonstrated and measured mode shapes and frequencies were compared to theoretical predictions demonstrating that the beams where in fact buckled and were performing as such. These initial resonator structures were a major driver in the efforts by several researchers within ARL, including the author, to study the residual stresses within the PZT stack as a function of process conditions and anneal steps. Material annealing steps added as a result of these efforts significantly improve the planarity of the PZT MEMS resonators to around 600 nm center deflections.

These second generation resonators were extensively tested. They showed significantly improved resonator admittance over the previously demonstrated ZnO devices. The PZT resonators exhibited resonant peaks of over 25 dB versus the 2 to 4 dB seen in the ZnO resonators made from the same mask set. The PZT resonators also demonstrated Qs on the same order as those extracted for the ZnO devices. Qs typically ranged from 2500 to 4000 with one device reaching over 8000. Although on par with the ZnO devices these values are still low compared to equivalent electrostatic devices and work needs to be done on material selection and anchor design if PZT based devices are to compete with electrostatic based resonators. The resonant frequencies of the PZT devices were also extended from the approximately 1 MHz frequency demonstrated by the ZnO resonators up to 10 MHz for the fundamental bending mode resonance of a clamped-clamped resonator.

In addition, the PZT resonators were studied for thermal stability, effect of poling condition, and linear dynamic range. Mainly because of the incorporation of the Pt thin films within the stack, the PZT MEMS devices performed poorly in thermal stability testing and devices tested were several orders of magnitude worse than their electrostatic counterparts. ZnO devices were not thermally tested so direct comparisons could not be made. It was shown that the poling process used for the PZT devices can alter the residual stress within the PZT stack which has a direct impact on the resonant frequency of the device. Techniques were also demonstrated to measure the linear and nonlinear spring and damping coefficients. It was shown that the linear dynamic range increases with reduced beam length and that it can also be increased at the trade off of reduced Q through the use of air damping.

A significant outcome of this research was the use of wafer bow and a combination of cantilever resonance testing, clamped-clamped resonator testing, and FEM to determine the Young's modulus, CTE and residual stresses for the SiO_2, Pt and PZT thin film materials that make up the resonator material stack. This data will be critical in the future not only for resonator design, but also for all PZT device design that use the sol-gel PZT films supplied by ARL. A summary of the data collected is reported in Table 10.1.

Table 10.1 Summary of measured and modeled material properties.

Material Property	SiO_2	Si_3N_4	Pt	PZT
Young's Modulus (MPa)	68	293	250	75
CTE (/ºC)	0.7	2.81	7.1	3.5
Residual Stress (MPa)	-40 to -94	640-670 (modeled)	134 to 733	91 to 284

Finally, studies were done into nonlinear mode shapes that appeared within the LDV velocity spectrum and mode shape data. These nonlinear modes were linked to the piecewise discontinuities and variations in the neutral axis along the traditional PZT MEMS resonator quarter length electrode design. These studies led to a modification of the PZT material stack to include a thin nitride layer to further modify the stress gradient and reduce the clamped-clamped beam initial static deflections. These generation III resonators were extremely planar (less than 60 nm center deflections for a 400 µm beam) and by minimizing variations in the neutral axis across the length of the resonator, devices without any nonlinear mode shapes were produced. The one performance trade-off for these devices was poor thermal stability.

10.2 Future Work

As with any research, there is always a desire to do more. From this initial research there are several promising and interesting topics for future research that are required if PZT-based MEMS resonators are to become viable for considered in RF applications including:

- Studies into anchor and material loss and ways to improve Qs.
- Development of better electrical equivalent models and impedance matched resonator designs.
- Studies into alternative beam and electrode materials to improve the stress gradients, thermal stability, and resonator Qs.
- Studies into alternative resonator configurations for higher frequency and improved Qs.
- Continued studies into the nonlinear behavior of stepwise discontinuous beams and the development of design rules to ensure linear performance of PZT based MEMS devices.
- Incorporation of arrays of devices to increase power handling.
- Incorporation of MEMS switches for variable band pass filter demonstrations.
- Integration with PZT based FBAR devices to cover the frequency range from a few Hz to GHz on a single chip.

Bibliography.

[1] H.J. Santos "RF MEMS Circuit Design for Wireless Communications," *Microelectromechanical Systems* pp. 167-201 2002.

[2] C.T. Nguyen "Vibrating RF MEMS for Next Generation Wireless Applications," *IEEE Custom Integrated Circuits Conference* vol. 1, pp. 257-264, 2004.

[3] "United States Frequency Allocations - The Radio Spectrum," U.S. Department of Commerce Office of Spectrum Management, October 2003.

[4] Q.-X. Su, P. Kirby, H. Komuro, M. Imura, Q. Zhang and R. Whatmore "Thin-Film Bulk Acoustic Resonators and Filters Using ZnO and Lead-Zirconium-Titanate Thin films," *IEEE Transaction on Microwave Theory and Techniques* vol. 49, no. 4, pp. 769-778, 2001.

[5] R. Aigner "RF-MEMS Filters Manufactured on Silicon: Key Facts About Bulk-Acoustic-Wave Technology," *Topical Meeting on Silicon Monolithic Integrated Circuits in RF Systems* pp. 157-167, 2003.

[6] H. Nathanson "The Resonant Gate Transistor," *IEEE Transaction on electron Devices* vol. 14, pp. 117-133, 1967.

[7] L. Lin, C.T. Nguyen, R.T. Howe and A.P. Pisano "Micro Electromechanical Filters for Signal Processing," *International IEEE Micro Electro Mechanical Systems Conference* pp. 226-231, 1992.

[8] C.T. Nguyen "Micromechanical Filters for Minaturized Low-Power Communications," *SPIE* vol. 3673, pp. 55-67, 1999.

[9] L. Lin, R.T. Howe and A.P. Pisano "Microelectromechanical Filters for Signal Processing," *IEEE/ASME J. Microelectromechanical Syst.* vol. 7, no. 3, pp. 286-294, 1998.

[10] E. Quévy, D. Galayko, B. Legrand, C. Renaux, C. Combi, D. Flandre, L. Buchaillot, D. Collard, B. Vigna and A. Kaiser "IF MEMS Filters for Mobile Communications," *8th IEEE International Conference on Emerging Techologies and Factory Automation* vol. 2, pp. 733-736, 2001.

[11] C.T. Nguyen "Frequency-Selective MEMS for Miniaturized Communication Devices," *IEEE Aerospace Conference* vol. 1, pp. 445-460, 1998.

[12] F. Ayazi and K. Najafi "High Aspect-Ratio Combined Poly and Single-Crystal Silicon (HARPSS) MEMS Technology," *Journal of Microelectromechanical Systems* vol. 9, no. 3, pp. 288-294, 2000.

[13] Y.-W. Lin, S. Lee, S.-S. Li, Y. Xie, Z. Ren and C.T. Nguyen "Series-Resonant VHF Micromechanical Resonator Reference Oscillators," *IEEE Journal of Solid-State Circuits* vol. 39, no. 12, pp. 2477-2490, 2004.

[14] M.W. Judy and R.T. Howe "Polysilicon Hollow Beam Lateral Resonators," *6th International IEEE Micro Electro Mechanical Workshop (MEMS 93)* pp. 265-271, 1993.

[15] W.-T. Hsu, J.R. Clark and C.T. Nguyen "A Sub-Micron Capacitive Gap Process for Multiple-Metal-Electrode Lateral Micromechanical Resonators," *The 14th IEEE International Conference on Micro Electro Mechancial Systems 2001* pp. 349-352, 2001.

[16] J.R.C. Reza Navid, Mustafa Demirci, and Clark T.-C. Nguye "Third-Order Intermodulation Distortion in Capacitively Driven CC-Beam Micromechanical Resonators," *14th International IEEE Micro Electro Mechanical systems Conference* pp. 228-231, 2001.

[17] F. Xu, R. Wolf, T. Yoshimura and S. Trolier-McKinstry "Piezoelectric Films for MEMS Applications," *11th International Symposium on Electrets* pp. 386-396, 2002.

[18] P. Muralt "PZT Thin Films for Microsensors and Actuators: Where Do We Stand?," *IEEE Transactions on Ultrasonics, Ferroelectrics and Frequency Control* vol. 47, pp. 903-915, 2000.

[19] B. Piekarski, M. Dubey, E. Zakara, R. Polcawich, D.L. DeVoe and D. Wickenden "Sol-gel PZT for MEMS Applications," *Integrated Ferroelectrics* vol. 42, pp. 25-37, 2002.

[20] D.L. DeVoe "Piezoelectric Thin Film Micromechanical Beam Resonators," *Sensors and Actuators A* vol. 88, pp. 263-272, 2001.

[21] K. Brooks, D. Damjanovic, N. Setter, P. Luginbuhl, G. Racine and N. Derooij "Piezoelectric Response of PZT Thin Film Actuated Micromachined Silicon Cantilever Beams," *IEEE* 1995.

[22] K.-I. Hong, S.-B. Kim, S.-J. Kim and D.-K. Choi "Cantilever Type PZT Microsensor Using Resonance Frequency for BioMEMS Application," *SPIE BioMEMS and Smart Nanostructures* vol. 4590, pp. 337-344, 2001.

[23] Ming Zang, Shayne M. Zurn, Dennis L. Polla, Bradley J. Nelson, and William P. Robbins "Design, Simulation and Fabrication of a Bridge Structure Microstransducer," *Modeling and Simulation of Microsystems, 3rd International Conference*, San Diego, CA, March 27-29, 2000

[24] B. Piekarski, M. Dubey, D.L. DeVoe, E. Zakar, R. Zeto, J. Conrad, R. Piekarz and M. Ervin "Fabrication of Suspended Piezoelectric Microresonators," *Integrated Ferroelectrics* vol. 24, no. 2, pp. 147-154, 1999.

[25] B. Piekarski, D.L. DeVoe, R. Kaul and M. dubey "Design, Modeling, and Testing of Micromachined Piezoelectric Clamped-Clamped beam resonators," *ASME 2000* vol. MEMS-Vol.2, 2000.

[26] B. Piekarski, D.L. DeVoe, M. Dubey, R. Kaul and J. Conrad "Surface Micromachined Piezoelectric Resonant Beam Filters," *Sensors and Actuators A* vol. 91, pp. 313-320, 2001.

[27] L.L. A.T. Fergson, V.T. Nagaraj, B. Balachandran, B. Piekarski and D. DeVoe "Modeling and Design of Composite Free-Free Beam Piezoelectric Resonators," *Sensors and Actuators A* vol. 118, pp. 63-69, 2005.

[28] L. Currano, B. Piekarski and D.L. DeVoe "FEA Modeling of Piezoelectric Clamped-Clamped Beam Microresonators," *ASME International Mechanical Engineering Congress & Exposition* 2002.

[29] B.A. Lynch "Electromechanical Modeling of Piezoelectric Resonators," Masters' Thesis, University of Maryland, 2002.

[30] W.G. Cady "Piezoelectricity; An Introducton to the Theory and Applications of Electromechanical Phenomena in Crystals," 1964.

[31] B. Jaffe, W.R. Cook and H. Jaffe "Piezoelectric Ceramics," 1971.

[32] D. Damjanovic, P. Muralt and N. Setter "Ferroelectric Sensors," *IEEE Sensors Journal* vol. 1, no. 3, pp. 191-206, 2001.

[33] S. Trolier-McKinstry and R. Zeto "Final Report Contract DABT63-95-C-0053: Manufacturable Sol-Gel PZT Films for Microsensors and Microactuators," ARL, 1999.

[34] W.-T. Hsu, J.R. Clark and C.T. Nguyen "Mechanically Temperature-Compenstated Flexural-Mode Micromechanical Resonators," *International Electron Devices Meeting* pp. 399-402, 2000.

[35] P. Aungkavattana and S. Trolier-McKinstry "Microstructure Development in Lead Zirconate Titanate Ferroelectric Thin Films During Annealing," *IEEE International Symposium on Applications of Ferroelectrics* vol. 2, pp. 801-804, 1996.

[36] F. Xu and S. Trolier-Mckinstry "Properties of Sol-Gel-Derived Lead Zirconate Titanate (PZT) Thin Films on Platinum-Coated Silicon Substrates," *IEEE International Symposium on Applications of Ferroelectrics* vol. 1, pp. 511-514, 1996.

[37] R.C. Piekarz "Lead Zirconate Titanate (PZT) Sol-Gel thin Film Preparation, Deposition and Testing," *ARL-TR-2895* pp. 1-15, 2002.

[38] I. Chopra "ENAE 651 Course Notes: Smart Structure Theory," University of Maryland, 1999.

[39] A.M. Baz "Course Notes: Introduction to Active Vibration Control," University of Maryland, 1999.

[40] D.L. DeVoe "Thin Film Zinc Oxide Microsensors and Microactuators," Ph.D. thesis, University of California, Berkeley, 1997.

[41] A. Ballato and J. Ballato "Electrical Measurements of Ferroelectric Ceramic Resonators," *ARL-TR-436* 1996.

[42] A. Ballato "Modeling Piezoelectric and Piezomagnetic Devices and Structures via Equivalent Networks," *IEEE Transactions on Ultrasonics, Ferroelectrics and Frequency Control* vol. 48, no. 5, pp. 1189-1240, 2001.

[43] J. Söderkvist "Electric Equivalent Circuit for Flexural Vibrations in Piezoelectric Materials," *IEEE Transactions on Ultrasonics, Ferroelectrics and Frequency Control* vol. 37, no. 6, pp. 577-586, 1990.

[44] J. Zelenka "Piezoelectric Resonators and Their Applications," *Studies in Electrical and Electronic Engineering* vol. 24, 1986.

[45] R. Zeto, B. Rod, M. Ervin, R. Piekarz, S. Trolier-McKinstry, T. Su and J. Shepard "High-Resolution Dry Etch Patterning of PZT for Piezoelectric MEMS Devices," *IEEE International Symposium on Applications of Ferroelectrics* pp. 89-92, 1998.

[46] Veeco Instruments, "WYKO Surface Profilers Technical Reference Manual," 2005.

[47] J. T.F. Retajczk and A. Sinha "Elastic Stiffness and Thermal Expansion Coefficient of BN Films," *Applied Physics Letters* vol. 36, no. 2, pp. 161-163, 1980.

[48] J.-H. Zhao, Y. Du, M. Morgen and P.S. Ho "Simultaneous Measurement of Young's Modulus, Poisson Ratio, and Coefficient fo Thermal Expansion of Thin Films on Substrates," *Journal of Applied Physics* vol. 87, no. 3, pp. 1575-1577, 2000.

[49] J.-H. Zhao, T. Ryan and P. Ho "Measurement of Elastic Modulus, Poisson ratio, and Coefficient of Thermal Expansion on On -Wafer Submicron Films," *Journal of Applied Physics* vol. 85, no. 9, pp. 6421-6424, 1999.

[50] M. Janda "Elasticity Modulus E and Temperature Expansion Coefficient of Alumiium thin films measured by a New Method," *Thin Solid Films* vol. 112, pp. 219-225, 1984.

[51] N. Maluf "An Introduction to Microelectromechanical Systems Engineering," *Microelectromechanical Systems* vol. 1, -265, 2000.

[52] J.M. Palmer "Handbook of Optics," vol. II, pp. 35 1995.

[53] MatWeb "Platinum, Pt, CP Grade, Annealed Online Material Data Sheet," 2005.

[54] D. Herman, M. Gaitan and D. DeVoe "MEMS Test Structures for Mechanical Characterization of VLSI thin Films," *SEM Conference* 2001.

[55] W.-H. Chuang, T. Luger, R.K. Fettig and R. Ghossi "Mechanical Property Characterization of LPCVD Silicon nitride Thin films at Cryogenic Temperatures," *Journal of Microelectromechanical Systems* vol. 13, no. 5, pp. 870-879, 2004.

[56] K.E. Petersen and C.R. Guarnieri "Young's Modulus Measurements of Thin films Using Micromechanics," *Journal of Applied Physics* vol. 50, no. 11, pp. 6761-6766, 1979.

[57] L. Kiesewetter, J.-M. Zhang, D. Houdeau and A. Steckenborn "Determination of Young's Moduli of Micrmechanical Thin Films Using the Resonance Method," *Sensors and Actuators A* vol. 35, pp. 153-159, 1992.

[58] Piezo Kinetics "PZT Product Literature - Mechanical Properties @ 25°C," Product Literature, 2005.

[59] E. Zakar, R. Polcawich, M. Dubey, J. Pulskamp, B. Piekarski, J. Conrad and R. Piekarz "Stress Analysis of SiO2/Ta/Pt/PZT/Pt Stack for MEMS Appication," *IEEE International Symposium on Applications of Ferroelectrics* vol. 2, pp. 757-759, 2000.

[60] E. Zakar, M. Dubey, R. Polcawich, B. Piekarski, R. Piekarz, J. Conrad and R. Widuta "Study of PZT Film Stress in Multilayer Structures for MEMS Devices," *International Symposium of Applied Ferroelectrics* 2000.

[61] V.K. Pamula, A. Jog and R.B. Fair "Mechanical Property Measurement of Thin-Film Gold Using Thermally Actuated Bimetallic Cantilever Beams," *Modeling and Simulation of Microsystems* pp. 410-413, 2001.

[62] PI Ceramics Gmbh. "Typical Parameters of Piezoelectric Ceramics," Product Literature, 2005.

[63] Piezomechanik GbmH "Piezo-Mechanics: An Introduction," Product Literature, 2005.

[64] D.G. Fertis "Mechanical and Structural Vibrations," 1995.

[65] S. Timoshenko, D.H. Young and J. W. Weaver "Vibration Problems in Engineering," 1974.

[66] H.A. Tilmans, M. Elwenspoek and J.H. Fluitman "Micro Resonant Force Guages," *Sensors and Actuators A* vol. 30, pp. 35-53, 1992.

[67] M.U. Demirci and C.T. Nguyen "Higher-Mode Free-Free Beam Micromechanical Resonators," *IEEE International Frequency Control Symposium and PDA Exhibition* pp. 810-818, 2003.

[68] K. Wang, Y. Yu, A.-C. Wong and C.T. Nguyen "VHF Free-Free Beam High-Q Micromechanical Resonators," *IEEE/ASME J. Microelectromechanical Syst.* vol. 9, no. 3, pp. 347-360, 2000.

[69] A.A. Afaneh and R.A. Ibrahim "Nonlinear Response of an Initially Buckled Beam with 1:1 Internal Resonance to Sinusoidal Excitation," *Nonlinear Dynamics* vol. 4, pp. 547-571, 1992.

[70] A. Nayfeh, W. Kreider and T.J. Anderson "Investigation of Natural Frequencies and Mode Shapes of Buckled Beams," *AIAA* vol. 33, no. 6, pp. 1121-1126, 1995.

[71] W. Kreider and A.H. Nayfeh "Experimental Investigation of Single-Mode Responses in a Fixed-Fixed Buckled Beam," *Nonlinear Dynamics* vol. 15, pp. 155-177, 1998.

[72] W.-Y. Tseng and J. Dugundji "Nonlinear Vibrations of a Buckled Beam Under Harmonic Excitation," *Journal of Applied Mechanics* vol. 38, no. 2, pp. 467-476, 1971.

[73] H. Li and B. Balachandran "Buckling and Free Oscillations of Composite Microsresonators," *submitted for publication , J. Microelectromechanial Systems* 2004.

[74] E. Zakar, M. Dubey, R. Polcawich, B. Piekarski, R. Piekarz, J. Conrad and R. Widuta "Study of Stress in PZT Films for MEMS Devices," *MRS Fall Meeting* 1999.

[75] R.G. Polcawich and S. Trolier-Mckinstry "Piezoelectric and Dielectric Reliability of Lead Zirconate Titanate Thin Films," *Journal of Material Research* vol. 15, no. 11, pp. 2505-2513, 2000.

[76] W.-T. Hsu and C.T. Nguyen "Geometric Stress Compenstion for Enhanced Thermal Stability in Micromechanical Resonators," *IEEE Ultrasonics Symposium* vol. 1, pp. 945-948, 1998.

[77] W.-T. Hsu and C.T. Nguyen "Stiffness-Compensated Temperature-Insensitive Micromechanical Resonators," *IEEE International Conference on Micro Electro Mechanical Systems* pp. 731-734, 2002.

[78] W.-T. Hsu, J.R. Clark and C.T. Nguyen "A Resonant Temperature Sensor Based on Electrical Spring Softening," *IEEE 11th International Conference on Solid State Sensors and Actuators* pp. 1484-1487, 2001.

[79] Robert Young, Personal Communincations on "Nonlinear Vibrations of Clamped-Clamped Beams," 2001.

[80] F. Ayela and T. Fournier "An Experimental Study of Anharmonic Micromachined Silicon Resonators," *Meas. Sci. Technology* vol. 9, pp. 1821-1830, 1998.

[81] B.P. J. Pulskamp, R.G. Polcawich, A. Wickenden, M. Dubey "Mitigation of Residual Film Stress Deformation in Multi-Layer MEMS Devices," *J. Vac. Sci. Technol. B* vol. 21, no. 6, 2003.